博士論文

Application of porous metals in sound absorption technology

（多孔質金属の吸音技術への応用）

テゥアシカル　ジャンナティ　アデニン

Application of porous metals in sound absorption technology

（多孔質金属の吸音技術への応用）

Approved, Thesis committee:

_____

Daiguji, Hirofumi
Professor, Department of Mechanical Engineer
The University of Tokyo, Japan

_____

Kato, Chisachi
Professor, Department Of Mechanical Engineer
The University of Tokyo, Japan

_____

Maruyama, Shigeo
Professor, Department Of Mechanical Engineer
The University of Tokyo, Japan

_____

Okamoto, Koji
Associate Professor, Department of Advanced Energy
The University of Tokyo, Japan

_____

Ishii, Tatsuya
Senior Researcher, Propulsion Research Unit
Japan Aerospace Exploration Agency, Japan

Abstract

Porous metal is a suitable candidate for acoustic liner in the jet engine as it can attenuate sound in wide frequency band and endure high pressure and high temperature environment. Many researches have been conducted various to study the sound attenuation by porous material under normal incident sound wave in the absence of flow. However, air flow and oblique incident sound wave exist in inside the nacelle of jet engine. Therefore, the sound attenuation by porous with the presence of air flow and under oblique incident sound wave that is similar to the condition inside the jet engine should be investigated.

The first step of this study was the characterization of the microstructure of two types of porous metal, sintered fiber and foam. The microstructure characterization is essential because the microstructure of the porous material affects the acoustic phenomena. In the second step, the flow resistivity of the porous sample was investigated. Flow resistivity, that represents the resistance on the fluid to flow through a porous material, could be related to viscous loss mechanism the sound attenuation inside the porous material. Furthermore, acoustic models also usually require the flow resistivity as one of the input parameters. In the next step, the sound attenuation of the porous metal under normal incident sound waves in the absence of flow was investigated. This step helps to understand the mechanism of sound attenuation inside porous metals as many acoustic models are available for this condition. Finally, the sound attenuation of porous material was investigated inside a flow duct under two conditions, in the absence of air flow and in the presence of air flow. The impedance under normal incident sound wave inside the impedance tube and under oblique incident sound wave inside the flow duct in the absence of flow was compared. If the impedance obtained from the impedance tube and the flow duct is similar, the porous material might acted as locally reactive. The impedance in the flow duct then can be predicted from relatively simple impedance tube setup and the acoustic model for porous material under normal incident sound wave. Then, the effect of the air flow on the sound attenuation of the porous metal was observed.

The microstructure affects the sound attenuation inside the porous metal. Two mechanisms of sound attenuation inside the porous metal were observed: viscous loss and resonance. Viscous loss is the sound attenuation mechanism inside the sintered fiber samples whereas the resonance is the dominant mechanism of sound attenuation inside the foam samples with low reticulation rate. The foam material with high reticulation rate has an acoustic characteristic similar to the sintered fiber material, i.e. viscous loss is dominant while the resonance is insignificant. Furthermore, it was observed that there is an optimum range of flow resistivity to obtain the best sound attenuation in the impedance tube. Furthermore, when there is no air flow in the flow duct, the impedance of the sintered fiber samples and the foam samples with porosity = 81% is similar to that in the impedance tube. Thus these samples acted in similar way with the locally reactive acoustic liner such as resonators. Conversely, the impedance of the foam samples with porosity = 85% was different from

that in the impedance tube. This sample has a low flow resistivity so that the attenuation so that the attenuation inside the sample occurred in both normal and parallel direction such as in non-locally reactive material. Furthermore, the interaction between the air flow and sound wave was shown to affect the sound attenuation inside the flow duct. It was also observed that the velocity profile only significantly affect the impedance of some porous samples.

TABLE OF CONTENT

CHAPTER 1

Introduction to the Use of Porous Metal for Jet Engine Noise Attenuation

In this chapter preface of the thesis and the background of this research are provided. Furthermore, the flow of the discussion in this study is briefly explained.

1.1 Airplane Noise

Noise emitted from airplanes might disturb the surrounding environment, especially in the airport area. Therefore, regulation was made to limit aircraft noise in the airport area [1]. Regulation required that the noise emitted from the aircraft to be measured at three locations as illustrated in Fig. 1.1. The accumulative of the noise measured at the three locations should be below the limit value. The noise limits are varied depend on the size of the aircraft as shown in Fig. 1.2. Figure 1.2 also shows the progression of the noise limit over time. The noise limit itself was first adopted in 1972 indicated as the Chapter 2 in Fig. 1.2. The increase of bypass ratio of the engine improved the fuel efficiency and lowered the emitted noise of the jet engine. Thus, the noise limit was lower in 1977 indicated as Chapter 3. As the noise reduction technology developed, the noise limit was reduced by 10 dB, in 2001 i.e. indicated as chapter 4 in Fig. 1.2. The latest regulation enacted in 2013 labeled as chapter 14 required further reduction of aircraft noise, 7 EPN dB from chapter 4 limit in total of 3 measuring points. Furthermore, the latest regulation also requires that noise reduction not less than 1 EPN dB must be conducted at each measuring points. The latest regulation should be applied in 2017 for large size aircraft and in 2020 for medium size aircraft. This noise limit became

more stringent over time in order to keep the noise in the airport area in a safe noise level due to the increase of the number of aircraft operating worldwide. Thus, further reduction attempts of airplane noise are essential to comply with the regulation.

Jet engine is one of the main sources of airplane noise. Jet engine noise can be originated from fan, combustor, compressor, and jet. Honeycomb liner is widely used for the nacelle mainly to reduce fan noise. Because honeycomb liner is one type of resonator, it has a peak noise absorption in a narrow range of frequency [2], [3]. Furthermore, honeycomb liner is not suitable for use in high temperature and high pressure environment. In addition, as the size of the nacelles is getting shorter, the location for acoustic liner might shift to the higher temperature and pressure sections [4], [5]. Therefore, a new acoustic liner that resists high temperature and high pressure might be required. One potential candidate for the future acoustic liner is porous material. Metal or ceramic based porous material might operate in high temperature and high pressure environment. Thus, porous material based acoustic liner can be used even in a harsher environment such as inside the combustion chambers or the exhaust of low-pressure turbines. Furthermore, unlike honeycomb liner, porous material can also reduce noise in wide frequency range.

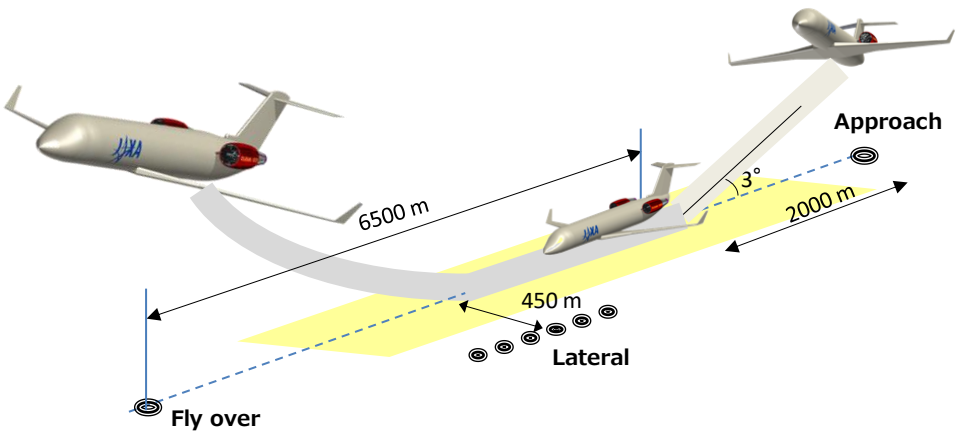

Figure 1.1 The Noise Measurement Location in the Airport Area Required by Regulation

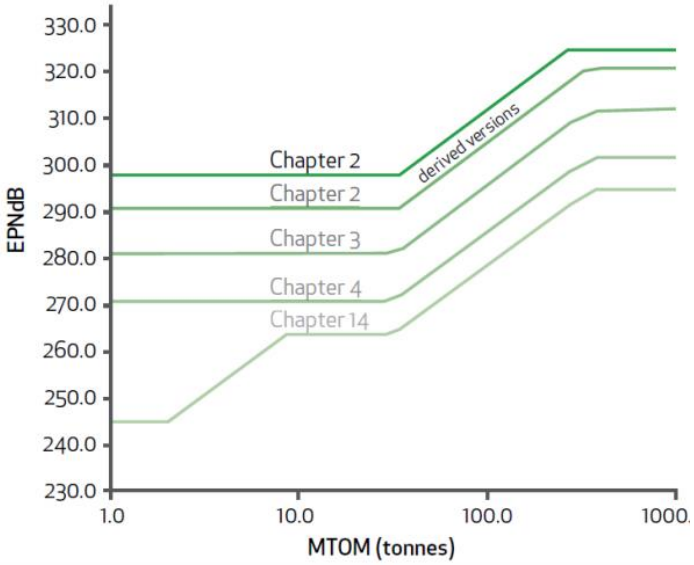

Figure 1.2 The Progression of the International Civil Aviation Organization (ICAO) Noise Standard

1.2 Porous Material for Sound Attenuation

When sound wave propagated through porous material, some mechanism might occur that will cause the attenuation of the sound wave [6], [7]. Therefore, porous material is commonly used as sound absorber in room and buildings for decades. Porous material for buildings application usually made of materials that cannot stand harsh environment e.g. fiber glass, foams, and wools. However, currently, porous material can be made from metals and ceramics that can resist harsh environment. Thus, the application of porous material as noise absorber can expand to a harsher working environment such a in the gas turbine of jet engine or a power plant [8]–[12].

The porous material made of ceramic and metal is potential for the future acoustic liner inside jet engines, especially in high temperature and high pressure sections. However, in order to use porous material based acoustic liner in the jet engine, several steps should be conducted as illustrated in Fig. 1.3. Starting from the device idea, basic research should be conducted to understand the sound attenuation mechanism by porous material. Furthermore, unlike the room and building application, there is air flow inside the jet engine. Therefore, the effect of this air flow to the sound attenuation of porous material should be identified. Then

the sound attenuation by porous material under high temperature and high pressure should be investigated. The understanding of the sound attenuation mechanism obtained from the basic research can be used as a basis to design the acoustic liner. A small scale prototype then will be manufactured and tested using small jet engine. If the performance is satisfying, the real scale model should be manufactured and tested inside a real jet engine. If the acoustic liner passes the real-scale test, finally the device can be applied to operating airplanes. This research covers the basic research of the design process.

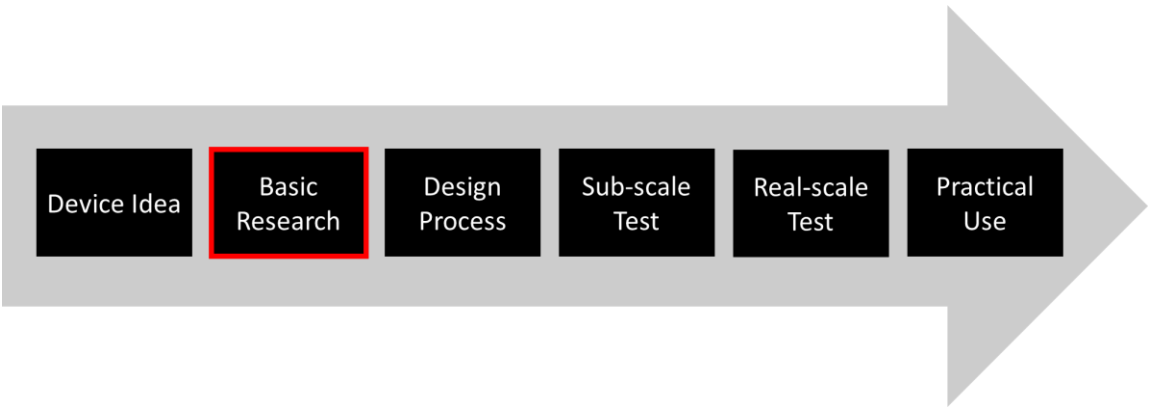

Figure 1.3 The steps to design porous material based acoustic liner for jet engines

1.3 Problem formulation and aim of research

Even though porous material is well-known as a good sound absorber, the mechanism of sound attenuation by porous material is still not well understood yet. Porous material may have various microstructure e.g. fibrous, foam, and granular. Each structure of porous material might cause a different sound attenuation mechanism. In the real application, the porous liner will be attached on the surface of the jet engine duct. Furthermore, the air flow existed inside the jet engine. This air flow might affect the sound attenuation mechanism.

One important parameter represents the acoustic characteristic of material is acoustic impedance. Impedance indicates the ratio between pressure and velocity at a point or a surface. The knowledge on impedance of the porous material can help to better

understand and predict the mechanism of sound attenuation of the porous material. Thus, the impedance value is essential in order to effectively design acoustic liner for the jet engine. The improvement of impedance eduction process of a liner inside a duct is still on going to obtain the accurate impedance of acoustic liner, even for the resonator type. Thus accurate impedance eduction of porous material is even more important. However, the air flow was shown to affect the impedance of the liner. Thus, the understanding of the effect of the air speed on the impedance of the porous material is important to design an effective liner to perform the best at the condition specific for the jet engine.

The acoustic properties of porous material under normal incident sound wave can be obtained relatively easily using an impedance tube. By using this method, the attenuation mechanism inside the porous structure can also be understood and predicted using available acoustic models for porous material. The condition inside a duct, however, is more complicated. Instead of normal incident sound wave, the sound wave propagated in parallel direction with the surface of the porous material. Furthermore, if there is air flow inside the duct, the attenuation mechanism inside the duct will be more complicated. The attenuation mechanism inside the flow duct might be affected by interaction between the air flow, sound wave, and porous structure. The interaction between the porous structure and the sound wave might be cause similar mechanism to the impedance tube condition whereas the other two factors would cause some differences between the acoustic properties inside the impedance tube and the duct. However, if direct relation between the acoustic properties inside the impedance tube and the flow duct can be identified, the mechanism of sound attenuation in the flow duct can be understood based on the impedance tube results.

Some problems could be identified related to the investigation of the sound attenuation by porous material for jet engine acoustic liner:

1. How is the sound attenuation mechanism inside the porous sample?
2. What is the effect of structure and other parameter on the sound attenuation mechanism inside the porous sample?
3. How is the sound attenuation mechanism in the flow duct?
4. Does the sound attenuation in the FD related to IT?
5. What is the effect of air flow on the sound attenuation by porous material?

This report is aimed to answer the above questions.

1.4 Content of this thesis

In this study, we are investigating the sound attenuation mechanism of the porous metal. We expect that this research can provide a basis to design an acoustic liner of jet engines. The step of the investigation is provided as follows.

1) Microstructure Characterization of Porous Metal

   As the first step, we characterize the microstructure of the porous sample. Microstructure related parameters, i.e. pore size and pore throat size, were measured. These parameters are important for further analysis of the porous metal in the next steps. The actual porosity of the sample was measured by using volume based method obtained from the mass of the samples. The observation of the samples surface was conducted to measure the pore size and pore opening size of the foam samples. As observation of the samples surface of the sintered fiber sample was failed to enable the measurement of the fiber diameter, X-Ray Computerized Tomography (CT) Scanning was conducted. The X-Ray CT Scan could provide an insight to the microstructure of the sintered fiber samples.

2) Flow through Porous Metal

The parameter characterizing the resistance encountered by fluid flow through a porous material is usually referred as flow resistivity. This parameter is widely considered to relate with the acoustic energy loss, when sound wave propagated through the porous material. Furthermore, the derivation of acoustic models for porous material usually includes flow resistivity as the input parameter. Therefore, in this step, we measured the flow resistivity of the porous samples and analyze the flow resistivity relation with the structure of the porous samples.

3) Sound Attenuation under Normal Incident Soundwaves on Porous Metal

We then investigated the acoustic properties of the porous material under normal incident sound waves. The normal incident sound waves assumption is simple so that there are many acoustic models available for this condition. The acoustic properties obtained from the measurements and the acoustic model might indicate the sound attenuation mechanism inside the porous material. Furthermore, the effect of the structure on the sound attenuation mechanism could be understood.

4) Sound Attenuation by Porous Material under Grazing Flow

For the acoustic liner application, the porous material will be attached in the wall inside the nacelles. Thus, the acoustic properties of acoustic liner are usually measured inside a flow duct setup. In this research, the sound attenuation by porous samples was also investigated inside a flow duct. The porous sample was attached in the wall of the flow duct in which air flow was generated. The acoustic properties of the samples under this condition were then compared to that of the samples under normal incident sound wave. The effect of the air flow on the sound attenuation by porous material in the flow duct was then analyzed.

1.5 References

[1] *2013 ICAO Environmental Report*. International Civil Aviation Organization, 2013.

[2] T. Harada, K. Nagai, H. Oinuma, H. Daiguji, and T. Ishii, "Validation of Impedance Eduction Method for Acoustic Liner Panel in Grazing Flow," *Asian Jt. Conf. Propuls. Power*, 2018.

[3] S. Busse-Gerstengarbe, F. Bake, L. Enghardt, and M. G. Jones, "Comparative Study of Impedance Eduction Methods, Part 1: DLR Tests and Methodology," in *19th AIAA/CEAS Aeroacoust. Conf*, 2013, pp. 1–11.

[4] D. L. Sutliff and M. G. Jones, "Low-Speed Fan Noise Attenuation from a Foam-Metal Liner," *J. Aircr.*, vol. 46, no. 4, pp. 1381–1394, 2009.

[5] D. L. Sutliff, M. G. Jones, and T. C. Hartley, "High-Speed Turbofan Noise Reduction Using Foam-Metal Liner Over-the-Rotor," *J. Aircr.*, vol. 50, no. 5, pp. 1491–1503, 2013.

[6] M. A. Kuczmarski and J. C. Johnston, "Acoustic Absorption in Porous Materials," *NASA/TM—2011-216995*.

[7] J. P. Arenas and M. J. Crocker, "Recent Trends in Porous Sound-Absorbing Materials," *J. Sound Vib.*, vol. 44, pp. 12–18, 2010.

[8] D. R. A. Christie, "Measurement of the Acoustic Properties of a Sound Absorbing Material at High Temperatures," *J. Sound Vib.*, vol. 46, no. 3, pp. 347–355, 1976.

[9] P. Nordin, S. L. Sarin, E. R. Rademaker, and S. Aerosystems, "Development of New Liner Technology for Application in Hot Stream Areas of Aero-Engines," pp. 1–13, 2004.

[10] P. S. Liu, H. B. Qing, and H. L. Hou, "Primary investigation on sound absorption performance of highly porous titanium foams," *Mater. Des.*, vol. 85, pp. 275–281, 2015.

[11] J. Pi, B. Zhang, J. Li, and Y. Chen, "Numerical Analysis of Sound Propagation Properties of Porous Metal At High Temperatures Based on Comsol Multiphysics," *21st Int. Confress Sound Vib.*, 2014.

[12] F. Sun, H. Chen, J. Wu, and K. Feng, "Sound absorbing characteristics of fibrous metal materials at high temperatures," *Appl. Acoust.*, vol. 71, no. 3, pp. 221–235, 2010.

CHAPTER 2

Microstructure Characterization of Porous Metal

In this chapter, the microstructure of the porous metal samples used in this study was characterized. The characterization methods include the volume based porosity measurements, photograph analysis, and X-Ray Computerized Tomography (CT) Scanning. This step is important to obtain essential parameters and basic information for further analysis in next chapters.

2.1 Introduction

Porous materials have been used by human for a long time. The natural porous materials were initially used by human such as for thermal insulation, acoustic insulation, and filtration. Furthermore, early investigation on the structure of the porous material might have started from analysis of rocks or sands in geology. The application of the geological study on porous materials was varied from the oil extraction to the ground water flow. However, currently, the advances of technology have enabled the production of synthetic porous material from various base materials, ranging from plastics, metals, to ceramics. The application of porous material has also expanded to a broader scope, such as the geothermal energy harvesting, packed bed reactor, and fuel cell. The type of the base material and its structure might affect the phenomena occur inside the porous material. Therefore, the investigation on the porous structure is essential for the prediction of the performance of the material.

The structure of porous material can be categorized as foam, fibrous, packed sphere. Each category might have further variation on the details of the microstructure. As an example, the foam material might consist of interconnected pore or closed pore[1], [2]. Furthermore, the

foam material with interconnected pore might have a different degree of interconnectivity, represented by the number of pore throat inside one pore, the size of the pore throat, and the number of neighboring pores[3]. This variation of microstructure of foam material might affect its performance in the application [2]–[4]. Therefore, the microstructure of the porous material have to characterized before further analysis.

One widely used parameter to characterize the microstructure of porous material is the porosity. Porosity is the ratio of the void volume to the void-solid volume. The porosity measurement can be conducted using various methods [1]. However, porosity cannot clearly indicate which structure the porous material has. Even for the case of foam material, porosity cannot determine the interconnectivity of the pores. Therefore, the visual analysis of the porous material should be conducted so that the structure can be identified. Furthermore, the dimension of the microstructure should be measured, e.g. the fiber diameter in the case of fibrous material or sphere diameter in the case of packed sphere. This microstructure dimension might affect the performance of the porous material.

Even though the structure observation is essential in the study related to porous material, the procedure is not easy. Direct visual observation might be conducted of the surface of porous material. However, observation on the surface of the samples might not be able to represent accurately the structure inside the samples. Therefore, in the past, a method was developed to analyzed sequences of thin sections of porous material [5], [6]. The image of the surface of a rock was first taken using Scanning Electron Microscope (SEM). Then the surface was polished to reduce 1 μm of thickness. After polishing, the SEM images of the surface was taken again. The polishing and SEM examination were conducted repeatedly to obtained sequential images of the porous material. However, this method is time consuming and destructive to the samples. Currently, the availability of computerized tomography (CT) scanning enables non-destructive observation of the inside of porous material [7]. The CT

scan can provide sequential images of the porous material. Thus, the local characteristic and inhomogeneity inside the porous material can be observed. Furthermore, the sequential images can be combined and then used for analyzing the 3D structure of the material.

A major difficulty in the porous material structure analysis is that a porous material might have inhomogeneous microstructure. The pores inside of block of foam material might vary in diameter and a block of fibrous material might have an area where the fibers are denser. The easiest analysis method is to use the averaged of the measured dimension and to assume the material is homogenous. If those assumptions failed to provide a correct analysis, the dimension might be considered as a distribution function.

In this chapter, the characterization of porous samples is reported. We first measured the actual porosity of the porous samples. Then visual observation of the surface of the porous samples was conducted to measure the dimension of the structure of the samples. Furthermore, X-Ray CT scan was also used for investigating the microstructure of the sample.

2.2 Porous Metal Sample

In this project, we used two types of porous metal: sintered fiber and foam. Both materials were made of stainless steel, SUS316L. The sintered fiber and foam samples were purchased from Nikko Techno, Ltd. and Nagamine Co., Ltd., respectively. Table 2.1 list the samples used in this project. The cross-section of the fibers is rectangular, area of which is equal to the area of a circle with a diameter of 0.03 mm as stated by the manufacturer. The porosity of sintered fiber samples was varied between 65%~80%. Meanwhile, the stated porosity of foam samples was 84%~94% and the pore size varied with the porosity.

The samples were prepared in two forms: cylinder and slab. The cylindrical samples were about 25 mm in diameter and 30 mm in thickness whereas the slab samples were 280 mm in length, 60 mm in width, and 30 mm in thickness as illustrated in Fig. 2.1. The actual

dimension of each sample might differ by ± 1 mm. The cylindrical samples were used for the microstructure characterization (Chapter 2) , the flow resistivity test (Chapter 3), and the impedance tube test (Chapter 4), whereas the slab samples were used specifically for the flow duct test (Chapter 5). Every sample was inserted in a casing liner to fit the sample slot in the impedance tube and flow duct setup. The foam samples have a stainless steel casing provided by the manufacturer. On the contrary, the casing for the sintered fiber samples was made of polymer using 3D printer. The casings for the foam samples are fixed whereas the casings for the sintered fiber samples are detachable.

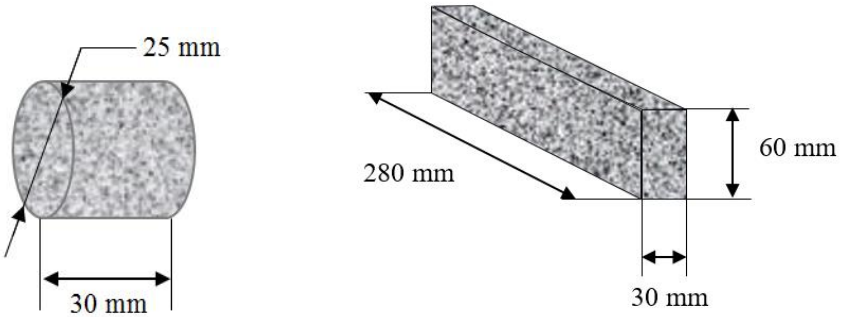

Figure 2.1. Dimension of the cylindrical and slab samples.

Table 2.1 Available porous metal samples.

	Sample	Cylindrical sample	Slab sample
Sintered Fiber			
1st batch	1	O	O
	2	O	X
	3	O	O
2nd Batch	1	O	X
	2	O	X
	3	O	X
	4	O	X
	5	O	X
	6	O	X
	7 – normal fiber	O	X
Foam			
	MF-80A	O	O
	MF-40	O	X
	MF-20	O	O

ϕ = 65% ϕ = 78% ϕ = 80%

(a)

ϕ = 82%

Normal

(b)

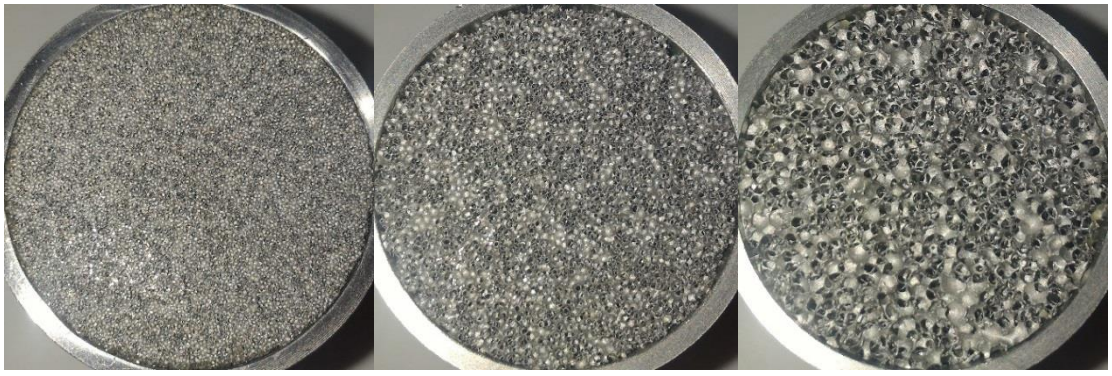

ϕ = 81% ϕ = 85% ϕ = 96%

(c)

Figure 2.2. The photographs of the surface of the (a) sintered fiber with planar fiber, (b) sintered fiber with normal fiber and (c) foam samples with varied porosity.

2.3 Characterization Method and Results

2.3.1 Volume based Porosity Measurement

The porosity measurement was conducted on all of the cylindrical samples. The measurement was based on void to total volume ratio. First, the total volume, V, was assumed

as the volume of the cylinder consists of the void and solid parts, $V = V_{Void} + V_{Solid}$. The actual thickness and diameter of the cylindrical samples are measured using a caliper and listed in Table 2.2. The actual total volume of the samples was calculated from these measured values. Second, the actual mass of the samples, M, was measured and listed in Table 2.2. Third, the solid volume, V_S, can be obtained using equation $V_S = M/\rho_{SUS}$, where ρ_{SUS} is the density of the SUS316L. Finally, the porosity of the samples was calculated by using eq. (2.1)

$$\phi = \frac{V - M/\rho_{SUS}}{V} \tag{2.1}$$

The measured porosity of the samples was also provided in Table 2.2. The porosity range of the fiber samples was from 65% to about 84% whereas the range of the cellular foam was from 81% to 96%.

Table 2.2 Actual dimension and porosity of the samples.

	Sample	t (mm)	D_{IT} (mm)	V (mm^3)	M (g)	V_s (mm^3)	Stated Porosity	Measured Porosity
Sintered Fiber								
1st batch	1	30.25	24.80	14612.30	40.97	5121.30	~65%	64.95%
	2	29.15	24.75	14024.22	24.81	3101.36	~80%	77.88%
	3	29.7	24.8	14346.62	23.02	2877.99	~80%	79.94%
2nd Batch	1	30.27	25.02	14882.54	20.02	2503.12	~80%	83.18%
	2	30.21	25.01	14841.16	19.62	2452.30	~80%	83.48%
	3	30.22	25.01	14846.08	19.53	2441.63	~80%	83.55%
	4	30.23	25.01	14850.99	19.19	2399.39	~80%	83.84%
	5	30.24	25.02	14867.79	20.54	2567.18	~80%	82.73%
	6	30.14	25.01	14806.78	18.67	2333.20	~80%	84.24%
	7 – normal	30.16	25.00	14804.76	20.90	2612.24	~80%	82.35%
Foam								
	MF-80A	30.80	25.00	15118.91	22.56	2820.15	84%	81.34%
	MF-40	30.25	25.00	14848.93	18.04	2255.22	90%	84.81%
	MF-20	29.23	25.00	14348.24	4.61	575.71	94%	95.99%

2.3.2 Geometric Dimension Analysis

The photographs of the surface of the samples were taken and shown in Fig 2.2. From visual observation, the structure of the surface of the sintered fiber samples was similar, except for the sample with normal fiber orientation. Furthermore, the diameter of the fiber cannot be measured from the figure as the resolution of the photos is low. On the contrary, the variation of the structure of the foam samples could be seen from visual observation of the photos as the pore size and the pore throat size varied. The pore size and the pore throat size were large enough for measurement using the photographed images. The method to estimate the pore size and pore throat size of the foam sample with ϕ = 96% is explained below.

In Fig. 2.3 (a), blue squares were drawn to identify one pore. The pore size was then obtained as the average of the height and width of this square. The size of the squares can be estimated by comparing it to the known diameter of the sample, D_{IT}. Meanwhile, in Fig. 2.3 (b), red squares were drawn to identify one pore opening, i.e. the hole connecting the pore to a neighboring pore. Similarly, the pore throat size was obtained as the average of the height and width of the red square. For every sample, 10 pores and pore throats were measured. Finally, the pore size and pore throat size of each sample was the average of 10 measured values. The pore size and the pore throat size are listed in table 2.3

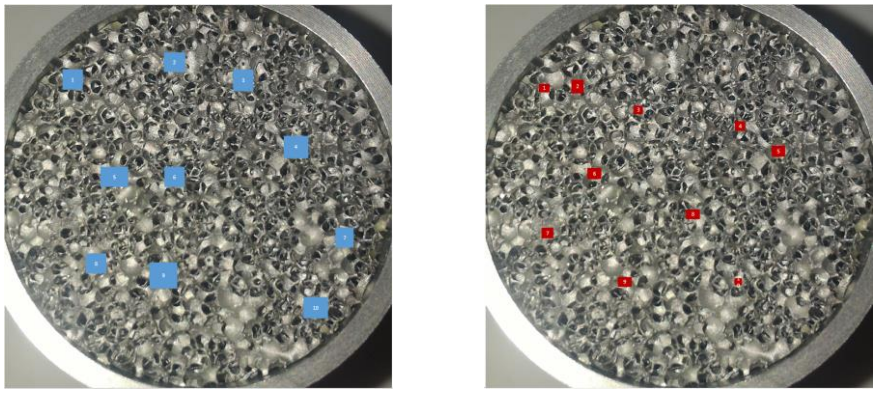

(a) (b)

Figure 2.3. Example of (a) pore size and (b) pore throat measurement of foam sample with ϕ = 96%.

Table 2.3 Pore size and pore throat size of the foam samples.

Sample Code	ϕ	Pore size	Pore throat size	Pore throat - Pore size ratio
MF-80A	81%	0.40±0.04	0.15±0.01	0.39
MF-40	85%	0.60±0.06	0.27±0.02	0.45
MF-20	96%	1.35±0.20	0.74±0.11	0.55

Table 2.4 The samples for CT Scan.

Sample	Batch	ϕ	Sample Length (mm)	Number of Images	Distance between images (mm)
Sample A	First	79.94%	29.7	1476	0.02
Sample B	Second	83.18%	30.27	1502	0.02

2.3.3 X-Ray Computerized Tomography (CT) Scanning

X-Ray CT Scanning was conducted to obtain information on the microstructure inside the samples because observation from photographed images of the surface sample could not provide many information on the structure. The scanning was conducted on the cylindrical samples. The CT scan could be performed on the sintered fiber samples as the casing is made of polymer. In contrast, the CT scan cannot be done on the foam sample because the X-Ray cannot pass through the stainless steel casing.

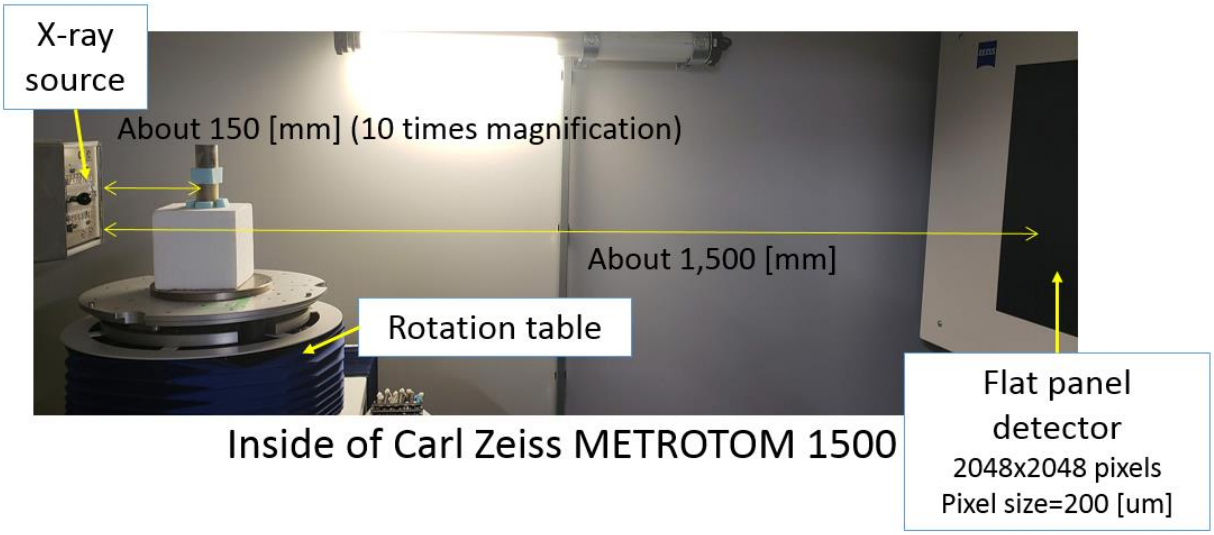

Figure 2.4. The setting inside of the CT Scan device.

The X-Ray CT Scanning was conducted on two of the sintered fiber samples, the sample with ϕ = 80% from the first batch referred as A and sample no. 1 with ϕ = 83% from the second batch referred as B as stated in Table 2.4. The scanning process used Carl Zeiss METROTOM 1500 device. The scanning time was 5 hours for each sample under condition 200kV and no pre-filter. The voxel size was 20.53 μm. The setting of the sample inside the scanning device is shown in Fig. 2.4.

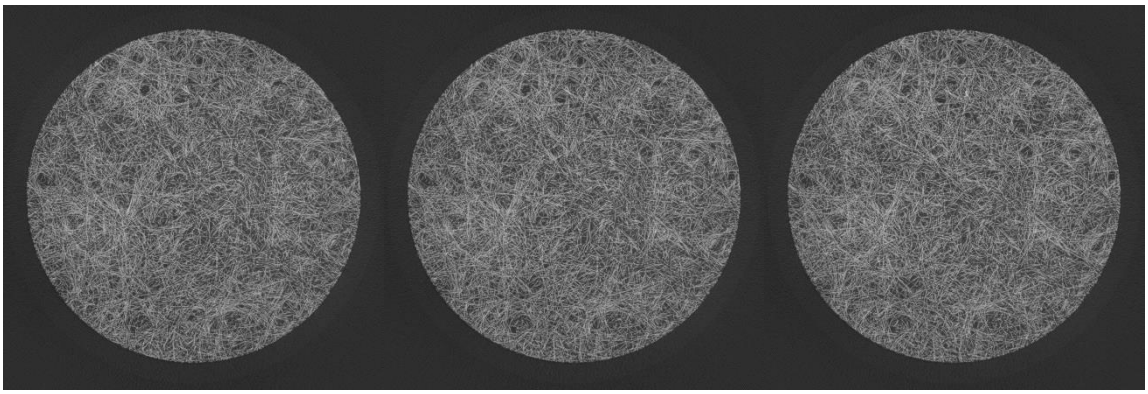

Images A-0565 to A-0567

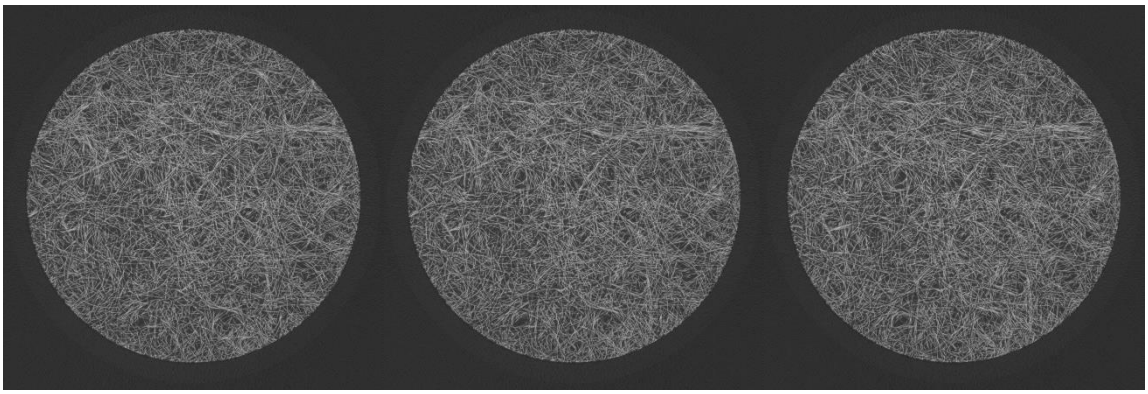

Images A-0663 to A-0665

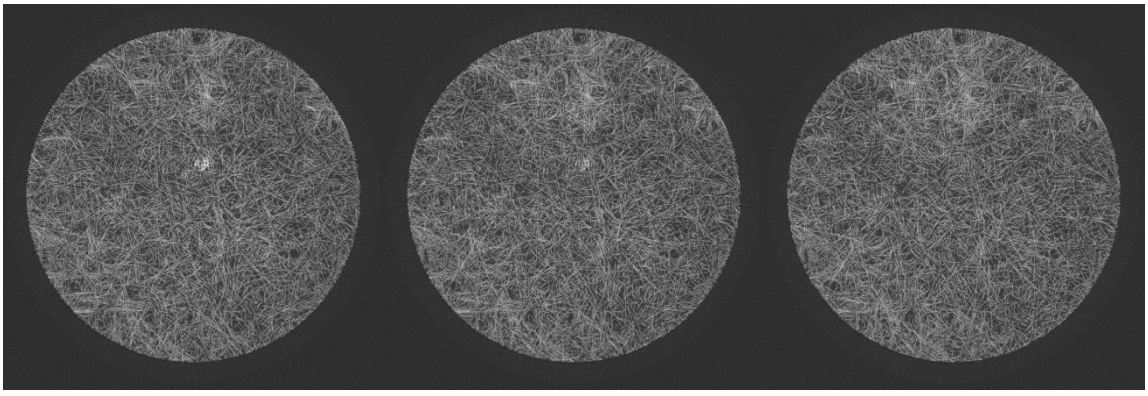

Images A-0798 to A-0800

Figure 2.5 Sequential images from CT Scanning of sintered fiber of samples A, ϕ = 80%.

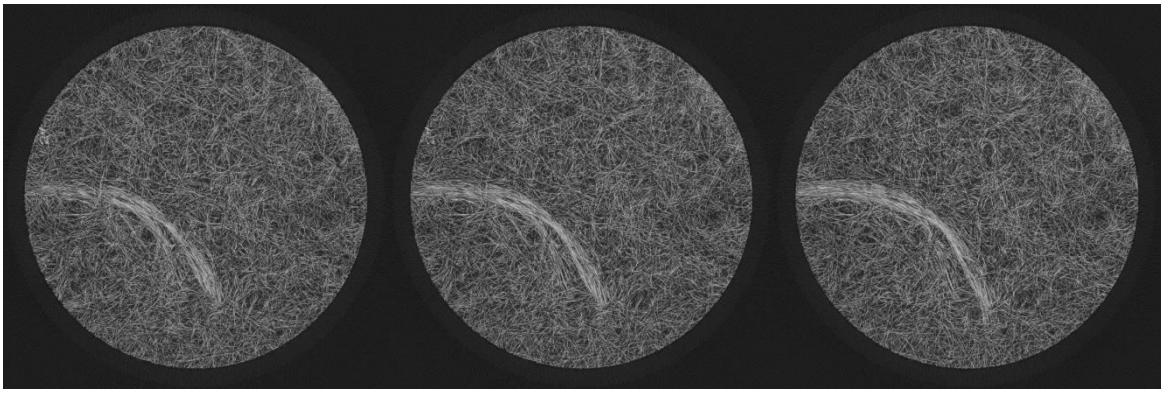

Images B-0539 to B-0541

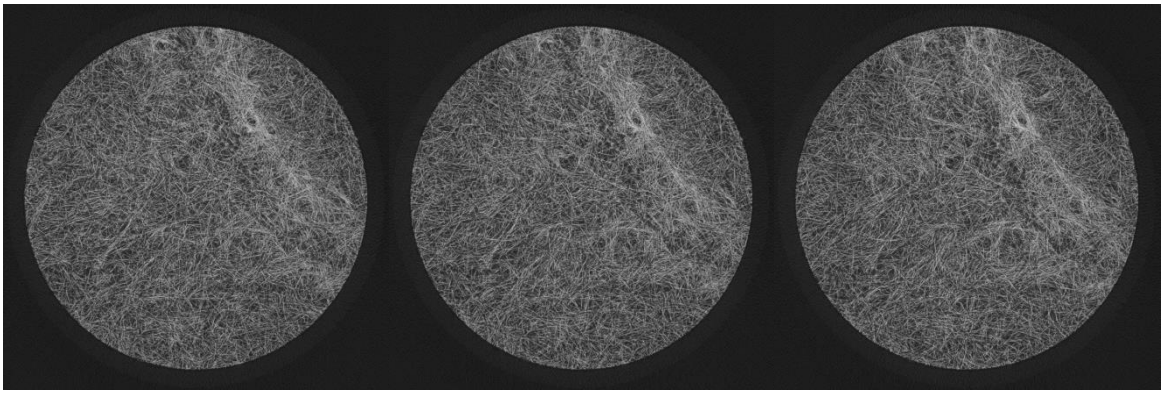

Images B-0568 to B-0570

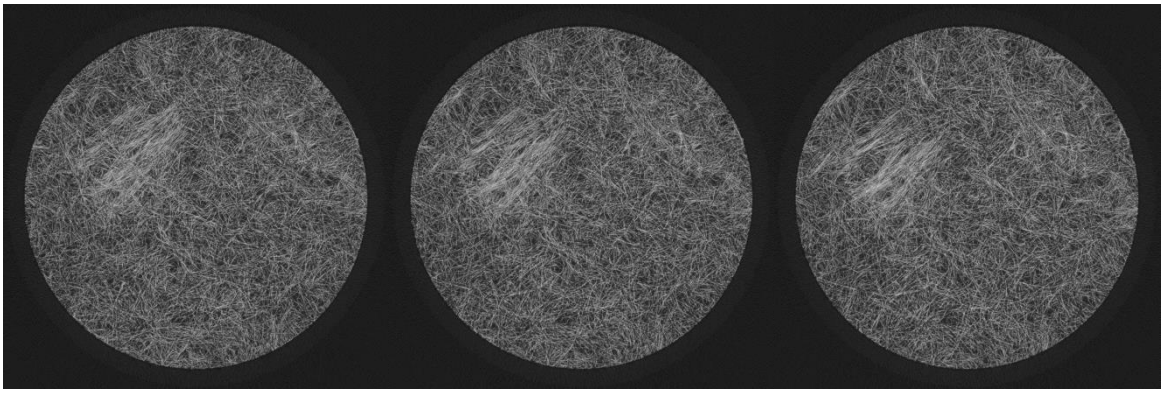

Images B-0664 to B-0666

Figure 2.6 Sequential images from CT Scanning of sintered fiber of sample B, ϕ = 83%.

Some of the sequential images from the CT scan of the sample A and B are shown in Fig. 2.5 and Fig. 2.6, respectively. Fig. 2.5 shows that the microstructure of the sample A is nearly isotropic in 2D and relatively homogenous. In the other hand, Fig. 2.6 shows that the sample B has clusters of gathered fibers indicating that the microstructure is inhomogeneous.

2.4 Discussion

The actual porosity of the foam samples is different from the stated porosity provided by the manufacturer. The stated porosity might represent the porosity of larger size of the bulk material. As our sample is quite small, the porosity might be different from the bulk porosity. The actual porosity would be used for the analysis in the next chapters.

The raw images from CT Scanning of the sintered fiber samples indicated that the homogeneity of the material might differs from one production batch to another. The material from the old batch was relatively homogenous and 2D isotropic while the new batch has some clustered fiber indicating inhomogeneity. This difference cannot be identified easily using direct visual observation. Furthermore, the raw images from the CT- Scanning could be processed into binary, black and white images, as explained in the appendix 2A.

The fiber diameter stated by the manufacturer would be used in further analysis whereas the measured pore size and pore throat size would be used for analysis in next chapters. The actual size of the fiber forming the sintered fibers samples could not be measured. The resolution of the photographs is not high enough to accommodate the measurement of the diameter of the fiber. Meanwhile, the pore size and pore throat size of the foam material was measured from the photographed images. The pore size and pore throat size varied as the porosity varied. Furthermore, the ratio of the pore and pore throat size also varied. Thus, parametric analysis using the samples was not possible as there is no fixed parameter. Furthermore, the value of the pore size and pore throat size of the foam samples might be not accurate as the measurement only used 2D image of the surface of the samples. Thus, the pore size and pore throat size measured here was only an estimation value for further analysis in next chapters. A more accurate measurement of the microstructure of both sintered fiber and foam material can be done by analysis of the 3D body processed from CT Scanning. Furthermore, higher resolution CT-Scan image can be obtain by using smaller specimens,

$V_s < 1\ cm^3$. However, care should be taken as the specimen become smaller; it might cause larger deviation from the bulk properties.

From the visual observation, foam samples used in this project has highly interconnected cells. However, the structure of each sample might have a different degree of interconnectivity. One parameter to represent the degree of interconnectivity of a porous material is the reticulation rate. A foam material with a high-reticulation rate has a high opening ratio and consists of reticulated solid frame. Thus, there are hardly any solid walls to separate the pores. In contrast, in foam material with low reticulation rate, each pore was surrounded by solid wall separating it to the neighboring pores. The separating walls might have opening to interconnect each pore, but the opening ratio is less that of the sample with high reticulation rate. From the characterization methods conducted in this chapter, the reticulation rate of the foam samples cannot be determined. Unlike the foam material, the void channel inside the sintered fiber material was formed by the gap between the fibers. Thus, the air channel might not be in the form of cells but more like interconnected ducts.

2.5 Conclusion

The actual porosity of the samples has been measured and this value will be used for analysis in the next chapters. The pore size and pore throat size of the foam samples was also estimated and they would be used for model analysis in the next chapters. The characterization process indicated that the homogeneity of the microstructure of porous material might varied between one batches of production to another. This difference of microstructure inside the material cannot be detected under direct visual observation. Moreover, the shape of the void inside the sintered fiber sample was different from the foam material. The void inside fiber samples resembles interconnected channel whereas the void inside the foam sample resembles interconnected cell.

2.6 References

[1] M. Kaviany, *Principles of heat transfer in porous media*. New York: Springer-Verlag, 1991.

[2] T. J. Lu, A. Hess, and M. F. Ashby, "Sound absorption in metallic foams," *J. Appl. Phys. J. Acoust. Soc. Am*, vol. 85, no. 123, 1999.

[3] O. Doutres, N. Atalla, and K. Dong, "Effect of the microstructure closed pore content on the acoustic behavior of polyurethane foams," *J. Appl. Phys.*, vol. 110, no. 6, 2011.

[4] T. J. Lu, F. Chen, and D. He, "Sound absorption of cellular metals with semiopen cells," *J. Acoust. Soc. Am.*, vol. 108, no. 4, pp. 1697–1709, 2000.

[5] C. Lin and M. H. Cohen, "Quantitative methods for microgeometric modeling," *J. Appl. Phys.*, vol. 53, no. 6, pp. 4152–4165, 1982.

[6] J. Koplik, C. Lin, and M. Vermette, "Conductivity and permeability from microgeometry," *J. Appl. Phys.*, vol. 56, no. 11, pp. 3127–3131, 1984.

[7] W. B. Lindquist, A. Venkatarangan, J. Dunsmuir, and T. Wong, "Pore and throat size distributions measured from synchrotron X-ray tomographic images," *J. Geophys. Res. Solid Earth*, vol. 105, no. B9, p. 21,509-21,527, 2000.

APPENDIX 2

X-Ray Computerized Tomography (CT) Image Processing

The raw data from the CT Scanning was processed using FIJI imageJ software, with a Macro program. ImageJ software has options to directly convert the raw CT images to black and white images. However, due to the low resolution of the sintered fiber images, the direct conversion cannot be done. Thus, the images were processed manually using some steps:

1. Define the circular frame of the sample.
2. Crop the sample.
3. Clear the image outside the circle.
4. Define the threshold value to convert into binary image (black and white).
5. Calculate the 2D porosity in one image by comparing the black and total pixels inside the circle.
6. The overall porosity (3D) was the averaged value of the 2D of images porosity.
7. Compare the calculated 3D porosity with the known volume based porosity.
8. If the difference between the calculated 3D porosity and the known volume based porosity was higher than 0.05, the thresholding value was revised.

The processing steps are also presented in block diagram in Fig. A2.1. The example of image processing step of A-0500 of sample A are provided in Fig. A2.2. However it is important to note that the 2D porosity deviate widely to the mean 3D porosity near the two surface of the sample as illustrated in Figure A2.3. Therefore, we disregard the analysis near the surface of the samples as illustrated in Figure A2.4. For sample A, the analysis was conducted from image no. 150 to 1349 as indicated in Fig. The 3D porosity from image processing and the volume based porosity as the reference are listed in Table

A2.1. These sequences of black and white images then can be constructed into 3D body. The examples of 3D body of the samples obtained from ImageJ are shown in Figure A2.5 and A2.6. The 3D data of the sample then can be used for further analysis such as actual fiber measurement, pore size, pore throat size, and even for numerical simulation.

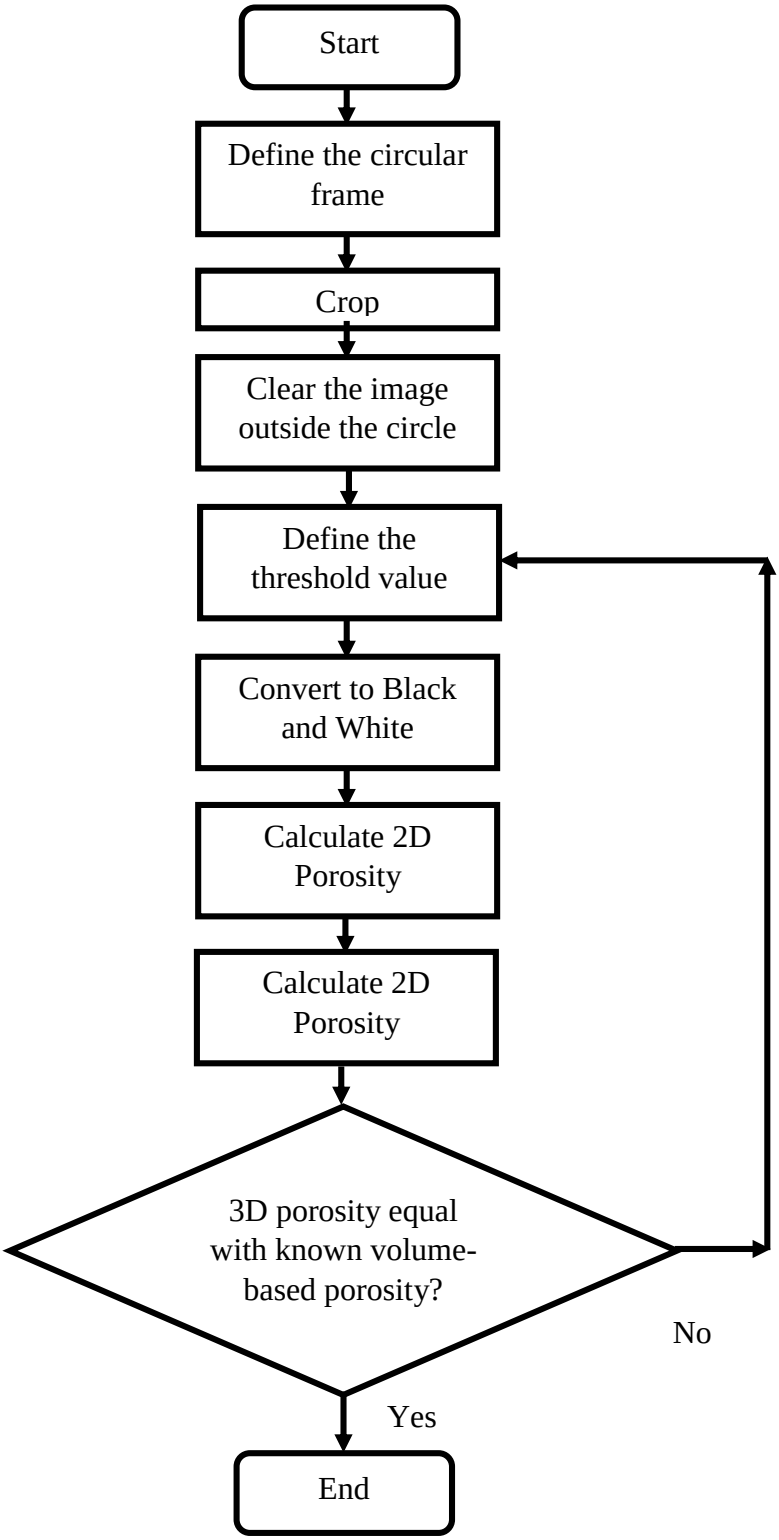

Figure A2.1. Block diagram of Image processing.

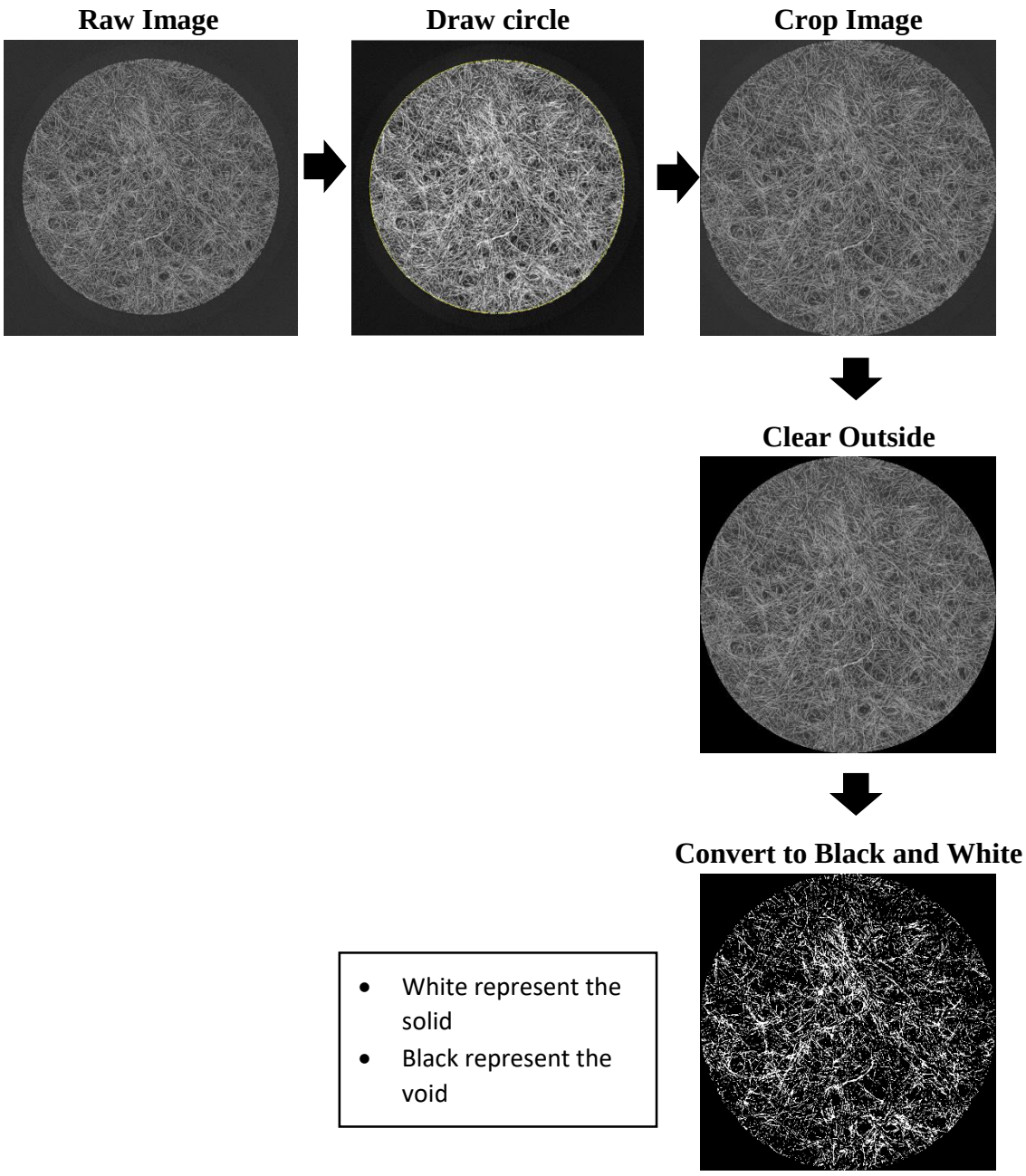

Figure A2.2. Examples of image processing of CT Scanning images of sample A Image A-0500.

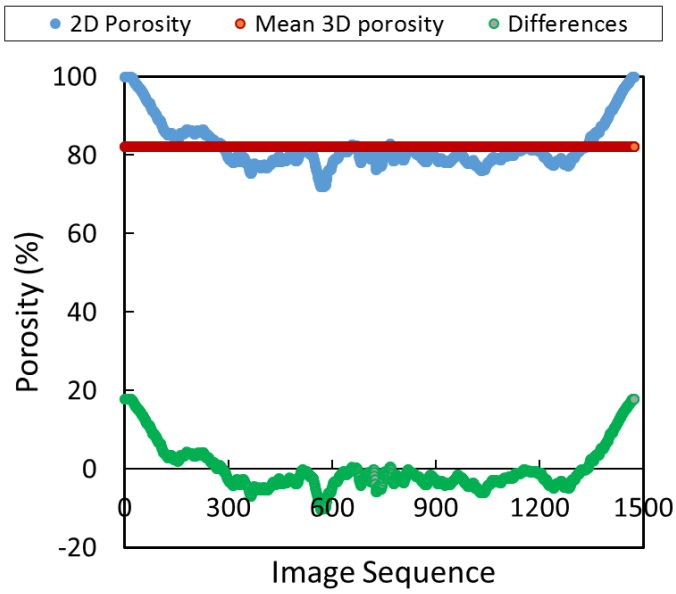

Figure A2.3. Illustration of variation of the 2D porosity along the sample length, for sample A image A-0000 to A-1476 with threshold 0 to 31700.

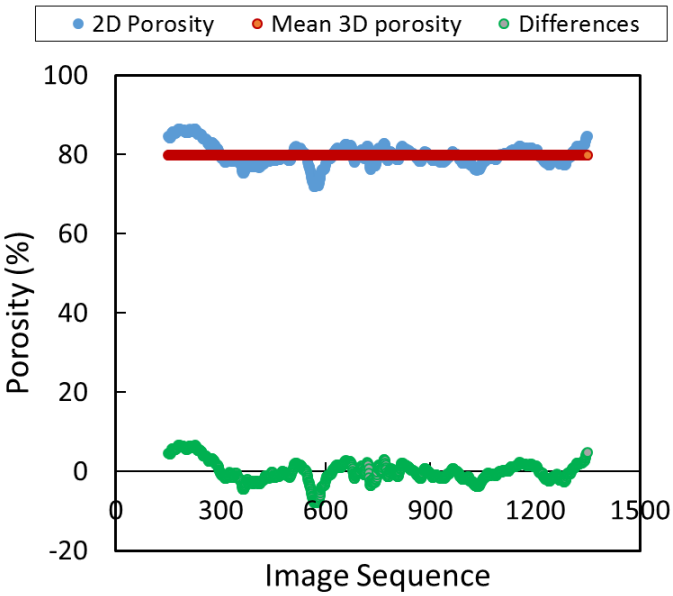

Figure A2.4. Illustration of variation of the 2D porosity along the sample length, for sample A image A-0150 to A-1349 with threshold 0 to 31700.

Table A2.1. Porosity of the samples from two measurement methods

Sample	From volume ratio (%)	From Image processing (%)	Low Threshold	High Threshold
Sample A	79.94	79.90±2.6	0	31700
Sample B	83.18	83.19±3.21	0	29540

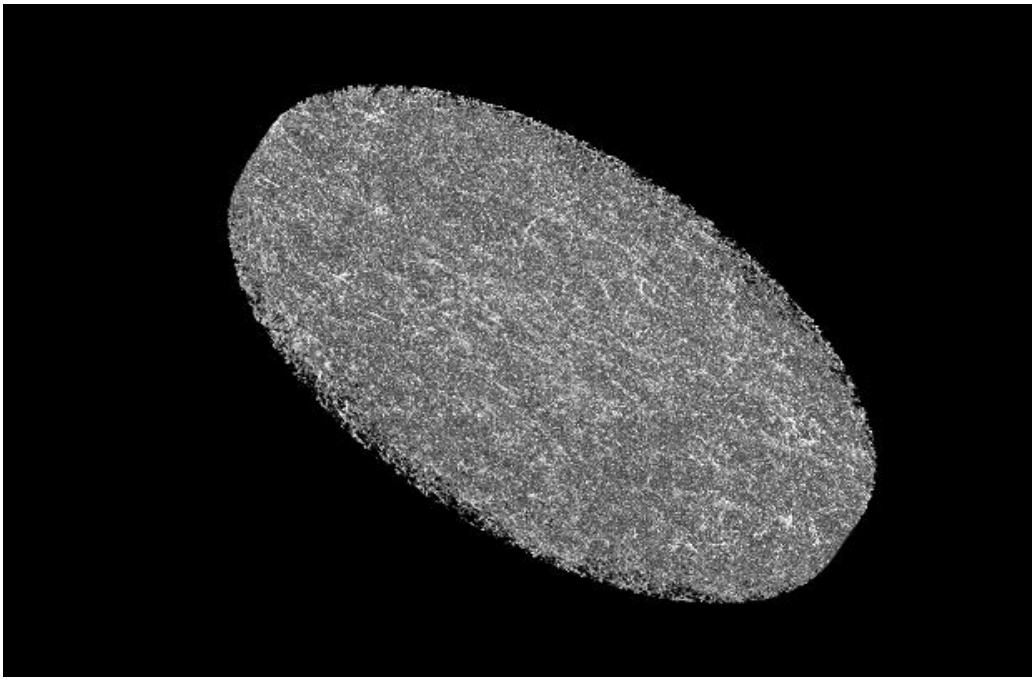

Figure A2.5. 3D structure of sample A from image sequence A-0150 to A-0249.

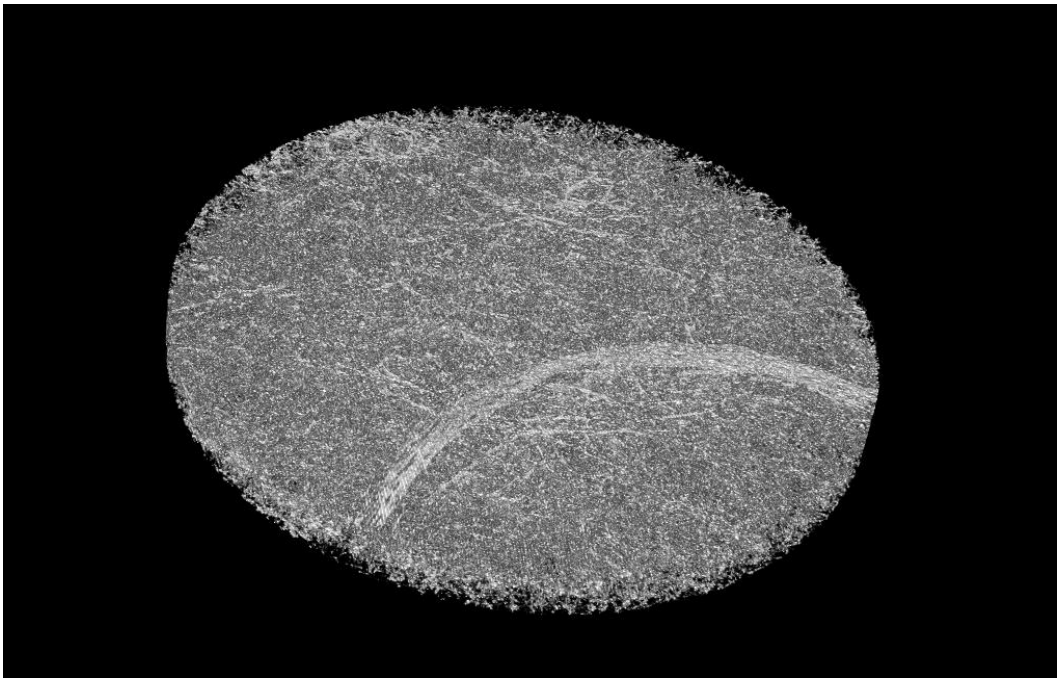

Figure A2.6. 3D structure of sample B from image sequence A-0550 to A-0549.

CHAPTER 3

Flow Resistivity of Porous Metal

In this chapter, the flow resistivity of the porous samples is reported. Flow resistivity represents the resistance encountered by fluid flow through a porous material. Furthermore, this parameter is widely considered to be related to the sound propagation through porous materials.

3.1 Introduction

The study of fluid flow through porous material is closely related to the work by D'arcy in 1856. D'arcy conducted experiments to observe the flow of water through sand. From this experimental data, he established the D'arcy equation as follows.

$$\bar{q} = \frac{k_D \Delta P}{l\eta} \tag{3.1}$$

where $\bar{q}$ is the velocity flux inside the tube, k_D is the permeability of the medium, ΔP is the pressure drop, l is the thickness of the sample, and η is the dynamic viscosity of the fluid. Equation 3.1 is analogous to Ohm's law in the field of electrical network so that the permeability can be considered as the conductance of the fluid possessed by porous material. Furthermore, in D'arcy theory, the fluid is assumed to flow inside a capillary channel inside the porous material. Therefore, this theory is also referred as capillary model. This theory has been improved by Kozeny and Carman to predict the permeability of porous material. In addition, this theory was further modified for a specific structure [1].

Another model of the flow through porous material is based on drag force. In this model, the fluid was considered to flow over an immersed body. Therefore, the drag force based models are usually directly developed to a certain microstructure [2], [3]. Iberall developed a

drag models are to estimate the permeability of a random distribution of circular cylindrical fibers [2]. Iberall stated that drag force analysis of fibrous material can be conducted when the space between fibers and the length of individual fiber are larger than the fiber diameter. This assumption indicated that the disturbance due to the adjacent fibers on the flow around a particular fiber is low. Thus, this drag model to calculate the permeability of fibrous sample might be suitable for material with porosity varied from 50% up to 98%.

The permeability of porous material is usually used for the study related to geological application such as groundwater flow. However, in the acoustic application, the characteristic of the fluid flowing through porous material is also important. Instead of permeability, the flow resistivity is the parameter used in acoustic field. Flow resistivity represents the resistance encountered by fluid flow through a porous material. The flow resistivity can be calculated using equation 3.2.

$$\sigma = \frac{\Delta P}{\bar{q} l} \tag{3.2}$$

where ΔP is the pressure drop, $\bar{q}$ is the velocity flux inside the tube, and l is the thickness of the sample. Therefore, the flow resistivity can be considered as the reciprocal of the permeability. Using electrical network analogy, the permeability might be considered as the conductance whereas the flow resistivity is the resistance.

Bies and Hansen. stated that the information on flow resistivity of porous material is enough to predict its acoustic properties [4]. Furthermore, flow resistivity become one of the main input parameters for acoustic models for porous material [5]–[7]. Kuczmarski et al. even illustrated using electrical network analogy that flow resistivity represents the resistance in DC current, whereas acoustic impedance represents electrical impedance in AC current.

Considering the importance of flow resistivity for the prediction of sound attenuation of porous material, the flow resistivity of the samples was measured and discussed in this chapter. The effect of the porous structure on the flow resistivity was also investigated.

Furthermore, the accuracy of a drag model flow resistivity for fibrous material was verified. The information on the flow resistivity of the samples will provide a basis for acoustic analysis in the next chapter.

3.2 Experimental Methods

3.2.1 Sample

Flow resistivity measurement was conducted on the cylindrical porous samples. The samples consist of three foam samples and ten sintered fiber samples. The lists of the samples are given in table 3.1 and 3.2.

Table 3.1 The properties of sintered fiber samples

Batch	Sample No.	Fiber Orientation	ϕ	Fiber diameter (mm)
1st	1	Planar	64.95%	0.03
	2	Planar	77.88%	0.03
	3	Planar	79.94%	0.03
2nd	1	Planar	83.18%	0.03
	2	Planar	83.48%	0.03
	3	Planar	83.55%	0.03
	4	Planar	83.84%	0.03
	5	Planar	82.73%	0.03
	6	Planar	84.24%	0.03
	7	Normal	82.35%	0.03

Table 3.2 The properties of foam samples

Sample	Fiber diameter (mm)	Pore size (mm)	Pore throat Size (mm)	Pore throat – pore ratio	ϕ
MF-80A	-	0.40±0.04	0.15±0.01	0.39	81.34%
MF-40	-	0.60±0.06	0.27±0.02	0.45	84.81%
MF-20	-	1.35±0.20	0.74±0.11	0.55	95.99%

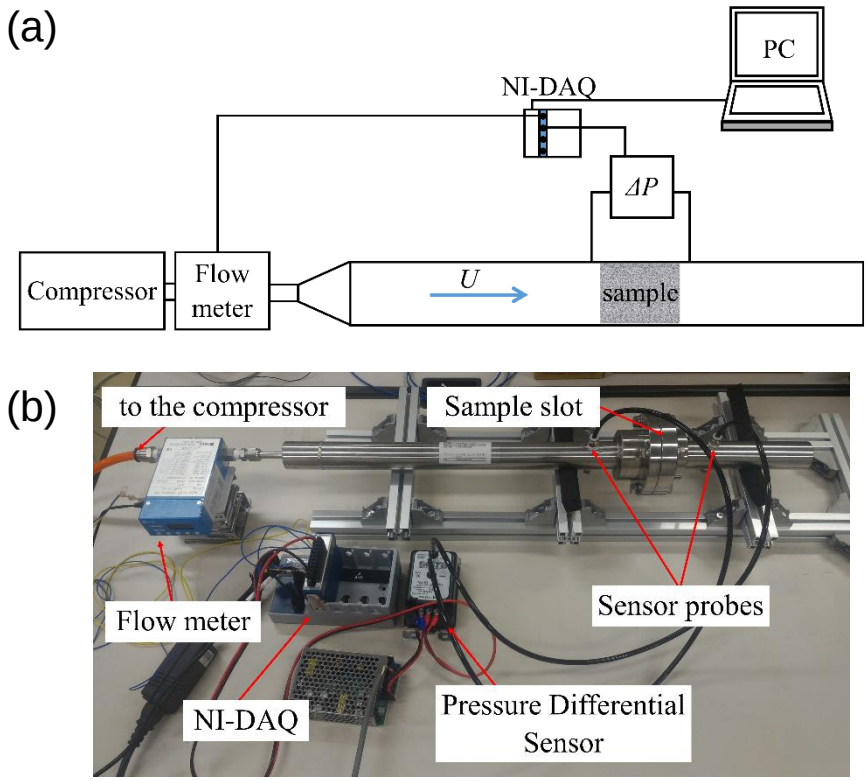

Fig. 3.1. (a) Scheme and (b) photograph of the flow resistivity measurement setup.

3.2.2 Experimental Setup

Flow resistivity of the porous metal was measured using a setup consists of a stainless steel pipe, a compressor, a flow meter, a pressure differential sensor, and National Instrument data acquisition device (NI-DAQ) as shown in Fig. 3.1. The inner diameter of the pipe is 23 mm and the total length is 650 mm. The sample was inserted in the slot where the sample surface is at a distance of 440 mm from the start of the pipe. A compressor was attached to the inlet of the tube to generate air flow inside the pipe. A flow meter was installed between the compressor and the pipe to measure the flow rate of the air. Furthermore, there is a converter to facilitate the difference between the outlet pipe diameter of the flow meter and stainless steel pipe diameter. A pressure differential sensor was attached to measure pressure drop of the air flow through the porous sample. Each probe of the sensors was attached at location 65 mm from the sample.

Three pressure differential sensors were used because the pressure drop range of each sample differs. Each of the sensors has a different pressure range reading - 100 kPa to 100 kPa, -500 kPa to 500 kPa, and -2500 kPa to 2500 kPa, all of which were Setra model 264. The sensor with pressure range - 100 kPa to 100 kPa was used for foam sample with ϕ = 96%. The sensor with pressure range - 500 kPa to 500 kPa was used for the rest of the foam samples. The sensor with the widest pressure range was used for all the fibrous samples as they caused much higher pressure drop than the foam samples.

The flow meter used in this study was KOFLOC Model 8500 MC/MM with flow rate range 10SCCM up to 20SLM or about 0.000167×10^{-3} m^3/s to 0.333333×10^{-3} m^3/s. This flow rate corresponds to air velocity within the range of 0.0004 m/s to 0.8023 m/s. The flow rate of the air from the compressor was changed by tighten or loosen the gate valve of the compressor. The flow rate was displayed in the screen of the flow meter. The flow rate range for each samples was also different depend on the maximum pressure drop that can be read by the pressure sensor.

The flow meter and the pressure differential sensor were connected to National Instrument Data Acquisition Device, NI-cDAQ-9174 containing NI 9215. The data were recorded using LabView Signal Express. The sampling rate for the measurement was 1000 samples/s. For each value of flow rate, the data was recorded for 3 s. The final values of the flow rate and the pressure were the average of the 3 s of data. The flow resistivity then can be calculated by using equation (3.2).

3.3 Mathematical Model for Flow Resistivity

To complement their acoustic model, Sides et al. derived an equation to calculate the flow resistivity of fibrous material based on drag force model [7]. This equation simplified the fibrous structure to be stacked cylinder structure illustrated in Fig. 3.2 (a). The actual structure of our sintered fiber is also shown in Fig. 3.2 (b). The flow resistivity per unit thickness of fibrous sample under perpendicular steady air flow is given by

$$\sigma = \frac{4\eta(1-\phi)}{\phi r^2}\left[\frac{1}{ln\left(\frac{3.7\eta\phi}{r\rho_f V}\right)} + \frac{2}{\pi}(1-\phi)\left\{3 - \frac{2}{ln\left(\frac{3.7\eta\phi}{r\rho_f V}\right)}\right\}\right] \tag{3.3}$$

where η is the viscosity of the air, v is the velocity of air near the fiber, e is the dilatation of the solid, r is the fiber diameter, and ρ_f is the density of the air. The velocity chosen for the calculation was 0.003 m/s.

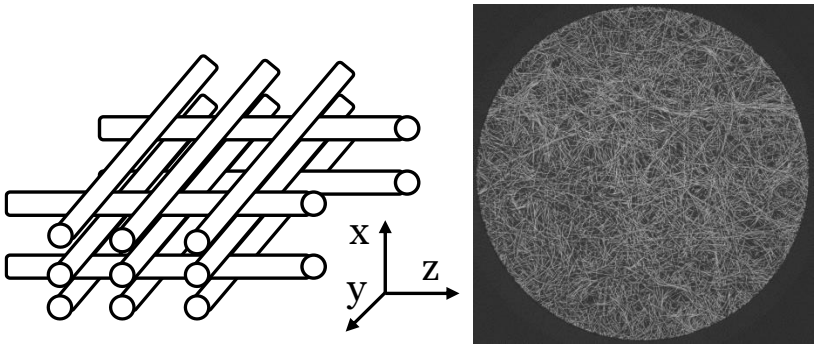

(a) (b)

Fig. 3.2 (a) Stacked cylinders structure assumption used by Sides et al and (b) the actual surface of the fibrous sample with ϕ = 80%

3.4 Results and Discussion

3.4.1 Pressure Drop

Figure 3.3 (a) shows the pressure drop of the sintered fiber sample with ϕ = 80%, from the 1st batch, obtained by two pressure differential sensors, sensor 1 with ±2500 kPa range and sensor 2 with ±500 kPa range. The sensor with pressure range with ±100 kPa was not used for the sample with ϕ = 80% because the velocity range that can be read by

this sensor is narrow and low. In the experiment, the steady flow rate can be measured as low as 0.5 SLM or 0.0083 $\times 10^{-3}$ m^3/s that corresponds to velocity 0.02 m^3/s. The flow rate below this value is difficult to be achieved using the compressor. The pressure drop read by the two sensor matches as shown in Fig. 3.3 (a). Further analysis was conducted using the sensor with ±2500 kPa range as it provided data in wider velocity range.

The pressure drop of each sample was measured in two directions as illustrated in Fig. 3.4. Figure 3.3 (b) shows that the measurement in the two direction of the sintered fiber sample with ϕ = 80% from the 1st batch, yield to similar results. Fig. 3.3 (b) shows that the pressure drop of the sample increased exponentially as the velocity increases. However, for the analysis this pressure drop results can be considered as linear in low velocity range. For the sample with ϕ = 80%, the velocity limit of linear range was 0.3 m/s whereas above this velocity limit the pressure drop increase was not linear. The pressure drop that will be used for the flow resistivity calculation is the ones within the linear range. The limit of linear pressure drop varied for each sample.

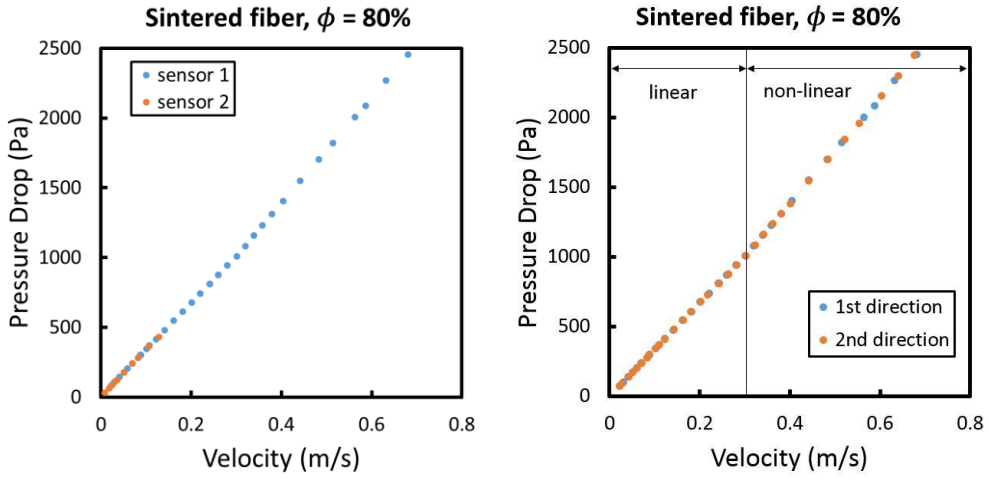

(a) (b)

Fig. 3.3. The pressure drop of sintered fiber sample from the 1st batch with ϕ = 80%, obtained from (a) two pressure differential sensors, sensor 1 (±2500 kPa) and sensor 2 (±500 kPa) and (b) measurement of the sample in two direction using sensor 1

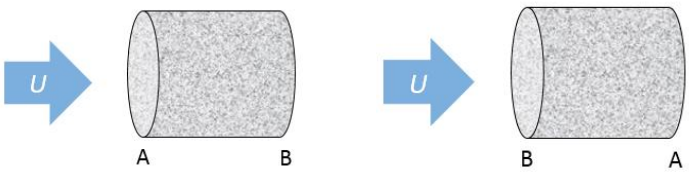

1st direction 2nd direction

Fig. 3.4. The two directions of the sample placement for the flow resistivity measurement.

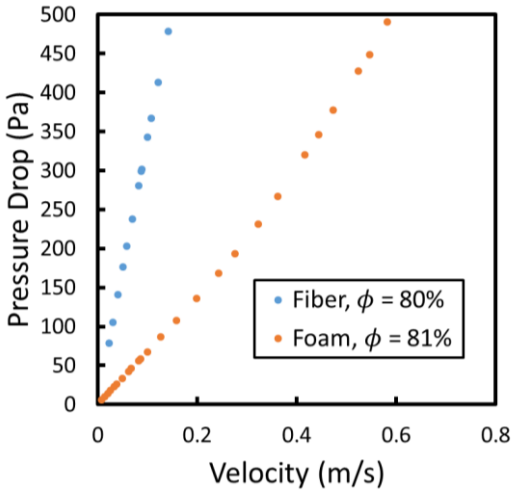

Fig. 3.5. The pressure drop of sintered fiber sample with ϕ = 80% and the foam sample ϕ = 81%

The comparison of the pressure drop of the sintered fiber sample with ϕ = 80% from the 1s batch and the foam samples with ϕ = 81% is shown in Fig. 3.5. The y axis of Fig. 3.5 is only up to 500 Pa, which is narrower than Fig. 3.3. It should be noted that the limit for linear pressure drop of the foam sample was observed at lower velocity, 0.15 m^3/s. The pressure drop data are shown in narrow pressure drop range to highlight the differences between the two samples. The pressure drop of the foam sample is lower than that of the fiber sample. Even though the porosity of both samples is similar, as previously stated in chapter 2, the shape of the void channel inside the foam is different from that of sintered fiber. The void inside the foam material was formed by interconnected cell whereas the void of sintered fiber material was formed by interconnected gap between the fibers. The channel dimension of the foam sample with ϕ = 81% ranges around the pore throat diameter and the pore size, 0.15 mm and 0.40 mm,

respectively. On the contrary, the void channel diameter of the sintered fiber material could not be measured from the structure characterization. The high pressure drop of the sintered fiber sample might be caused by a smaller size of void channel and the high tortuosity of the structure. Therefore, air flow experienced more obstruction to flow and more viscous loss occurred inside the sintered fiber sample.

The pressure drop of the sintered fiber samples from the 2nd batch with planar and normal fiber orientation is shown in Fig. 3.6. The porosity is almost the same i.e. ϕ = 82.73% and ϕ = 82.35%, respectively. However, Fig. 3.6 shows that when air flow through the sample normal fiber, the pressure drop is lower than the planar sample. This is because the air channels inside the normal sample were formed between the fibers that are parallel to the air direction. Therefore, these channels are relatively straight connecting both surfaces of the porous sample. Conversely, inside the planar sample, the fibers are perpendicular to the air direction. Thus, the planar fibers created more severe obstruction for the air flow. Furthermore, the placement of the fibers on each layer might create torturous channels inside the planar sample. More viscous loss occurred inside the torturous channel than that inside the straight channel. As a result the pressure drop inside the planar sample is higher than in normal sample. The pressure drop results of the other samples are provided in Appendix.

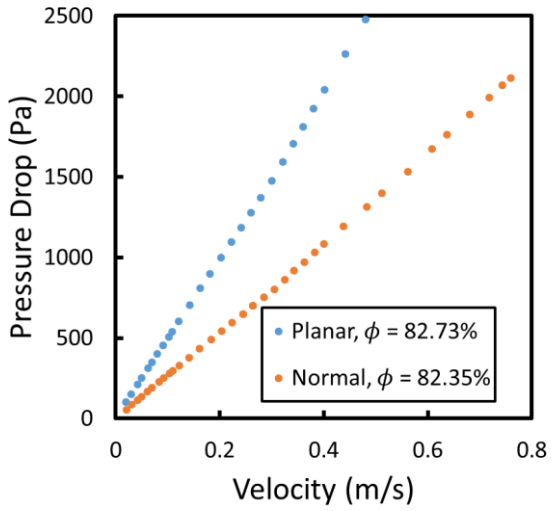

Fig. 3.6 The pressure drop of sintered fiber samples with planar and normal fiber orientation

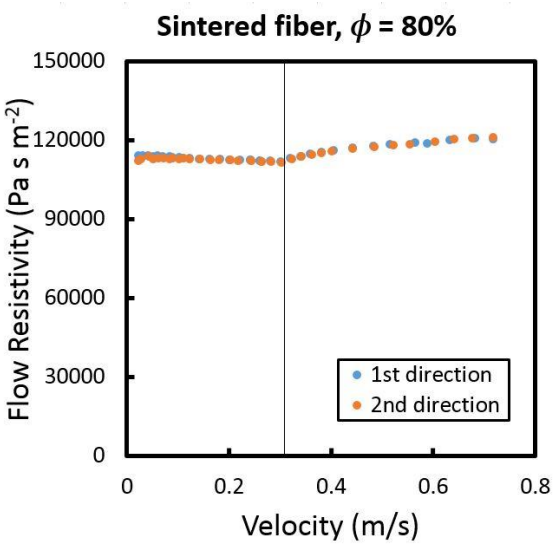

Fig. 3.7. The flow resistivity of sintered fiber sample with ϕ = 80% from the 1st batch, obtained from measurement of the sample in two direction using sensor 1

3.4.2 Flow Resistivity

The flow resistivity of sintered fiber sample with ϕ = 80% from the 1st batch is shown in Fig 3.7. The flow resistivity calculated from two direction measurement matched well. Furthermore, the flow resistivity was constant within the linear pressure drop range, 0 m/s up to 0.3 m/s. In higher velocity, the flow resistivity started to increase. The flow

resistivity value used for further calculation and analysis in the next chapter was the average of the flow resistivity values within the linear range.

The flow resistivity of the sintered fiber, from the 1st and 2nd batch, and the foam samples are shown in Fig 3.8. It is shown that the flow resistivity of the sintered fiber samples from the 1st batch was lower than the samples from the 2nd batch. The higher flow resistivity of the samples from the 2nd batch might be caused by the inhomogeneity such as the cluster of gathered fibers revealed in chapter 2. On the other hand, the foam samples have much lower flow resistivity. This is because the channel size inside the foam samples might be larger than that in the sintered fiber samples. The lowest flow resistivity was that of the sample with ϕ = 96%. This sample has the largest pore size and pore throat size of all the foam samples. Thus, the air can flow through this sample easily with low obstruction.

Since the pressure drop of the sintered fiber sample with normal fiber orientation is lower than that of the planar fiber sample, the flow resistivity of the normal fiber sample is also lower than that of the planar sample. The flow resistivity values of all the samples are listed in Table 3.3 and 3.4.

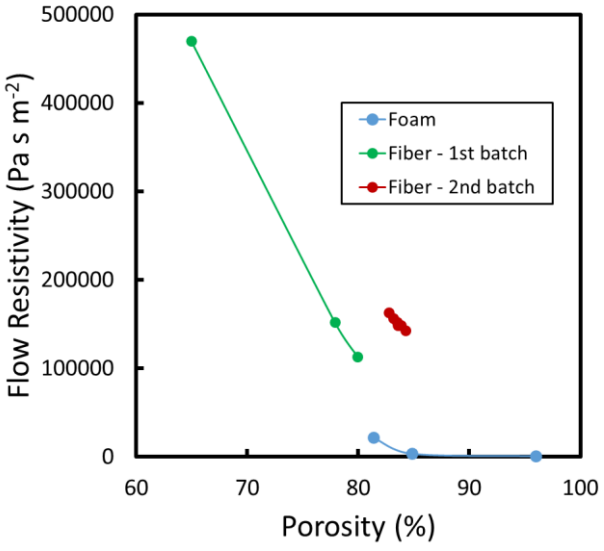

Fig. 3.8. The flow resistivity map of the sintered fiber and foam samples

Table 3.3 The measured flow resistivity of the sintered fiber samples

Batch	Sample No.	Fiber Orientation	ϕ	Fiber diameter (mm)	Flow Resistivity (Pa s m^{-2})
1st	1	Planar	64.95%	0.03	469942
	2	Planar	77.88%	0.03	151914
	3	Planar	79.94%	0.03	113140
2nd	1	Planar	83.18%	0.03	156504
	2	Planar	83.48%	0.03	151964
	3	Planar	83.55%	0.03	148347
	4	Planar	83.84%	0.03	148327
	5	Planar	82.73%	0.03	162846
	6	Planar	84.24%	0.03	142929
	7	Normal	82.35%	0.03	87696

Table 3.4 The flow measured flow resistivity of the foam samples

Sample	Fiber diameter (mm)	Pore size (mm)	Pore throat Size (mm)	Pore throat – pore ratio	ϕ	Flow Resistivity (Pa s m^{-2})
MF-80A	-	0.40±0.04	0.15±0.01	0.39	81.34%	21603
MF-40	-	0.60±0.06	0.27±0.02	0.45	84.81%	3411
MF-20	-	1.35±0.20	0.74±0.11	0.55	95.99%	606

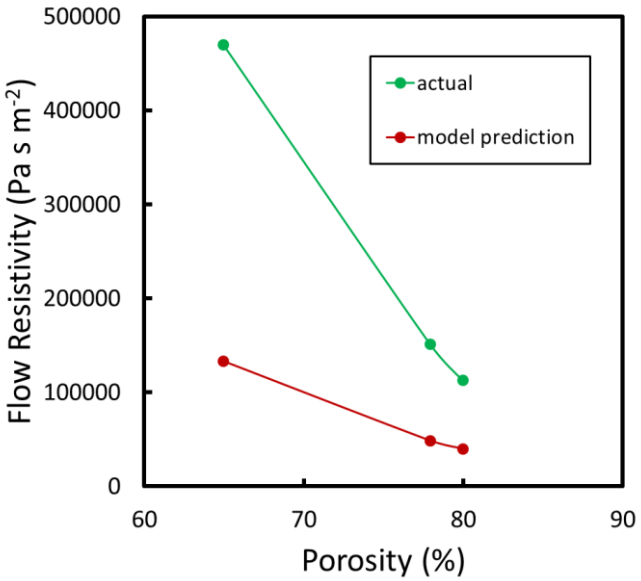

Fig. 3.9. The measured and calculated flow resistivity of the sintered fiber

The flow resistivity calculated using drag based model for the old sintered fiber samples is shown in Fig. 3.9. The calculated flow resistivity were lower than the

measured flow resistivity of the sintered fiber samples. Therefore, the drag force analysis might not be appropriate for the sintered fiber sample because the structure is more similar to a material with capillary channels, instead of the stacked cylinders. Thus, the capillary based analysis might yield to a better flow resistivity prediction of the sintered fiber samples. In the paper written by Sides et al., they used drag based model to predict the flow resistivity of their fibrous samples but did not compare it to the actual values [7]. However, the predicted flow resistivity, which was then used in their acoustic model analysis, was able to provide an accurate prediction of the acoustic properties of Rocksil mineral wool. Therefore, for some type of fibrous materials such as mineral wool, the drag based model might be used for the flow resistivity prediction, whereas capillary model might be more appropriate for the other types of fibrous material such as our metallic sintered fibers. Thus, the fibrous material might have different structures, i.e. different diameter and different channel size that will affect the flow resistivity of the material.

3.5 Conclusion

The structure of the porous material affects the flow resistivity of porous samples. The foam samples have larger void channel dimensions than that of the sintered fiber samples. As a result, the foam samples yield to flow resistivity up to 3 orders of magnitude lower than of the sintered fiber samples. Furthermore, inhomogeneity in sintered fiber materials might increase the total flow resistivity.

3.6 References

[1] B. T. Åström, R. B. Pipes, and S. G. Advani, "On Flow through Aligned Fiber Beds and Its Application to Composites Processing," *J. Compos. Mater.*, vol. 26, no. 9, pp. 1351–1373, 1992.

[2] A. S. Iberall, "Permeability of Glass Wool and Other Highly Porous Media," *J. Res. Natl. Bur. Stand. (1934).*, vol. 45, no. 5, pp. 398–406, 1950.

[3] V. Tarnow, "Airflow Resistivity of Models of Fibrous Acoustics Materials," *J. Acoust. Soc. Am.*, vol. 100, no. 6, pp. 3706–3713, 1996.

[4] D. A. Bies and C. H. Hansen, “Flow resistance information for acoustical design,” *Appl. Acoust.*, vol. 13, no. 5, pp. 357–391, 1980.
[5] M. E. Delany and E. N. Bazley, “Acoustical properties of fibrous absorbent materials,” *Appl. Acoust.*, vol. 3, no. 2, pp. 105–116, 1970.
[6] J.-F. Allard and Y. Champoux, “New Empirical Equations for Sound Propagation in Rigid Frame Fibrous Materials,” *J. Acoust. Soc. Am.*, vol. 91, no. 6, pp. 3346–3353, 1992.
[7] D. J. Sides, K. Attenborough, and K. A. Mulholland, “Application of a Generalized Acoustic Propagation Theory to Fibrous Absorbents,” *J. Sound Vib.*, vol. 19, no. 1, pp. 49–64, 1971.

APPENDIX 3

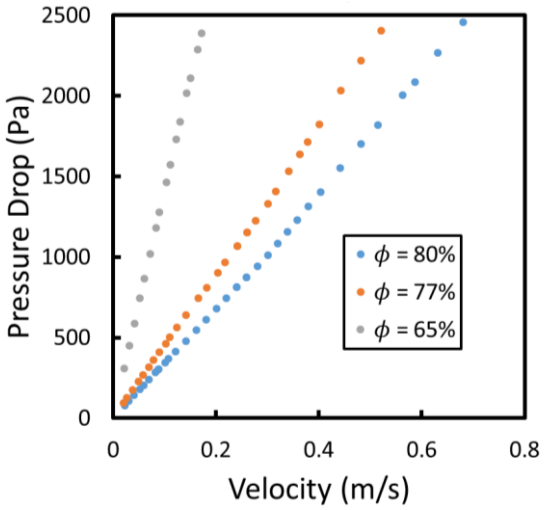

Fig. A1. The pressure drop of sintered fiber samples from the 1st batch with varied porosity

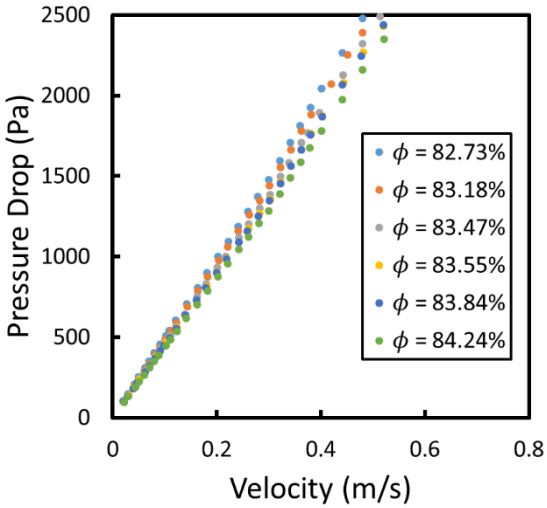

Fig. A2. The pressure drop of sintered fiber samples from the 2nd batch with varied porosity

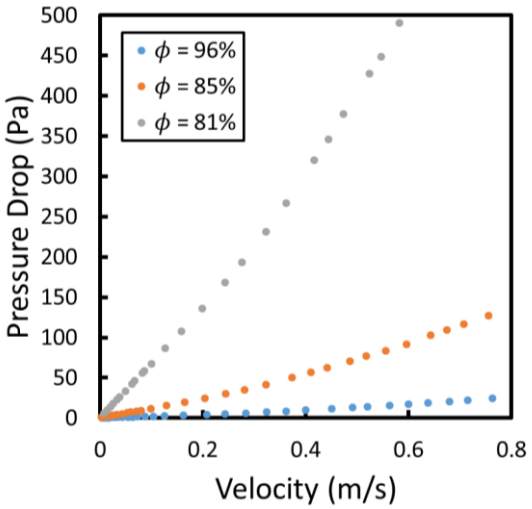

Fig. A4. The pressure drop of the foam sample with varied porosity

CHAPTER 4

Normal Incident Soundwaves on Porous Metal

In this chapter, the acoustic attenuation mechanism under normal incident wave of the sintered fiber and foam stainless steel were investigated using an impedance tube setup. Further analysis using acoustic model to better understand the sound attenuation mechanisms inside the porous metal was conducted. Furthermore, the parameter to affect the sound attenuation characteristic was discussed.

4.1 Introduction

When sound wave propagated through porous material, some attenuation mechanism might occur i.e. viscous loss, acoustic damping, fiber scattering, and resonance effects in the air cavity [1]–[3]. There are variations on the microstructure porous material, such as fibrous, cellular, or granular structures. Each of these microstructures might yield to a different attenuation characteristic. Furthermore, the material of the porous structure related to mechanical properties i.e. the stiffness of the solid frame might also affect the sound attenuation mechanism. For flexible porous material, the incident acoustic energy might deform the flexible solid frame. In contrast, for stiff material, the solid frame does not deform so that the acoustic energy was converted into heat by viscous loss and dissipated. In designing porous material based acoustic liner for the nacelle of jet engine, elevated temperature and pressure in the jet engine requires the use of material that can withstand this adverse environment [4], [5]. Therefore, in this project we used metal porous material made of stainless steel. Furthermore, by considering the future prospect of the porous material

availability in the market, the porous metal samples used in this project were purchased from manufacturer. Two type of porous metal were chosen: sintered fiber and foam.

To understand the acoustic characteristic of porous material, some acoustic models have been developed. These models usually assume normal incident sound waves without air flow to simplify the analyses. Thus, these models well represent the condition in an impedance tube setup. The acoustic models for porous materials can be classified into three categories. The first category is for the empirical models that are built directly using experimental acoustic data of porous material from the impedance tube. The most well-known empirical model was developed by Delany and Bazley [6]. This model also has been improved by Miki and Komatsu [7], [8]. The second category is for models that use effective medium approaches whereby the porous material was considered as an effective fluid with some characteristic properties: effective density and an effective bulk modulus [9], [10]. The impedance and the propagation constant of the porous material then can be calculated using the effective density and the effective bulk modulus. The last category pertains to models that were theoretically derived based on the analysis of sound wave interaction with the structure of the porous material [11]–[14]. Acoustic models in the third category were usually used for the prediction of sound attenuation by specific microstructures.

The parameters to affect the sound attenuation might be different for each type of material microstructure. Furthermore, the parameters directly related to the structure of the material varied for different types of porous material. For the sintered fiber material, the geometric parameter is only the fiber diameter. In this study, the fiber diameter is constant, thus, the effect of the fiber diameter on the acoustic properties cannot be verified from experiments. For the foam material, the geometric parameters comprise of the pore size, pore throat, and pore throat – pore ratio. This parameter might significantly affect the sound attenuation characteristic of foam material as stated by Lu et al. [11].

By considering the difficulties to directly measure the geometric parameter and relate it to the acoustic properties of porous material, some general parameters related to structure of material are used in analysis. General parameters usually used for characterizing porous material are porosity, flow resistivity, tortuosity, and reticulation rate. First parameter is the porosity, which indicates the ratio of the void volume to the total volume of porous material but does not provide information of the dimension and characteristic of the structure, such as the size of the void and the connectivity of the void. Second, flow resistivity is a parameter that widely considered being a proper parameter to predict the acoustic properties of porous material as it represents the resistance faced by fluid to flow through the porous material. As stated in chapter 3, flow resistivity can be calculated from the pressure drop of the fluid when it flows through the material. Thus, this parameter is related to viscous loss of the fluid. Next parameter, tortuosity represent the ratio between the length of the channel connecting two points in the front surface and back surface to the closest distance between the two surface. Lastly, Doutres et al. stated that the reticulation rate also affects the sound attenuation in foam materials [15]. Reticulation rate of foam material indicates the connectivity of the pores. Material with low reticulation rate contains pores each of which separated by well-defined wall. Conversely, material with high reticulation rate has not so well-defined solid wall separating the pores and the solid part os in the reticulated structure. In this project we are able to measure the actual porosity and flow resistivity of the porous samples but not the tortuosity and the reticulation rate.

In this chapter, we investigated the acoustic characteristic of two types of porous metal, sintered fiber and foam, under normal incident sound wave. The validity of available acoustic model to predict the acoustic properties of the sample is verified. The experimental results and model calculation was then analyzed to identify the sound attenuation mechanism inside porous material. The effect of the microstructure on the sound attenuation mechanism was

also investigated. Furthermore, the parameters to affect the sound attenuation mechanism were also discussed.

4.2 Experimental Methods

4.2.1 Sample

The samples used in the impedance tube measurement are the same cylindrical samples used in flow resistivity measurements in Chapter 3 and structure characterization in Chapter 2. The diameter of the sample is about 25 mm and the thickness of the sample is about 30 mm. The samples used in the impedance tube measurement are listed in Table 4.1. Each sample was made of stainless steel. The fiber diameter of sintered fiber samples is 0.03 mm. The details of the structure dimension of the samples have been reported in chapter 2. The pore size and pore throat size of the foam sample varied as the porosity varied. The properties of the samples are shown in table 4.1. and 4.2.

Table 4.1 The properties of sintered fiber samples

Batch	Sample No.	Fiber Orientation	ϕ	Fiber diameter (mm)	Flow Resistivity (Pa s m^{-2})
1st	1	Planar	64.95%	0.03	469942
	2	Planar	77.88%	0.03	151914
	3	Planar	79.94%	0.03	113140
2nd	1	Planar	83.18%	0.03	156504
	2	Planar	83.48%	0.03	151964
	3	Planar	83.55%	0.03	148347
	4	Planar	83.84%	0.03	148327
	5	Planar	82.73%	0.03	162846
	6	Planar	84.24%	0.03	142929
	7	Normal	82.35%	0.03	87696

Table 4.2 The properties of foam samples

Sample	Fiber diameter (mm)	Pore size (mm)	Pore throat Size (mm)	Pore throat – pore ratio	ϕ	Flow Resistivity (Pa s m^{-2})
MF-80A	-	0.40±0.04	0.15±0.01	0.39	81.34%	21603
MF-40	-	0.60±0.06	0.27±0.02	0.45	84.81%	3411
MF-20	-	1.35±0.20	0.74±0.11	0.55	95.99%	606

4.2.2 Impedance Tube Setup

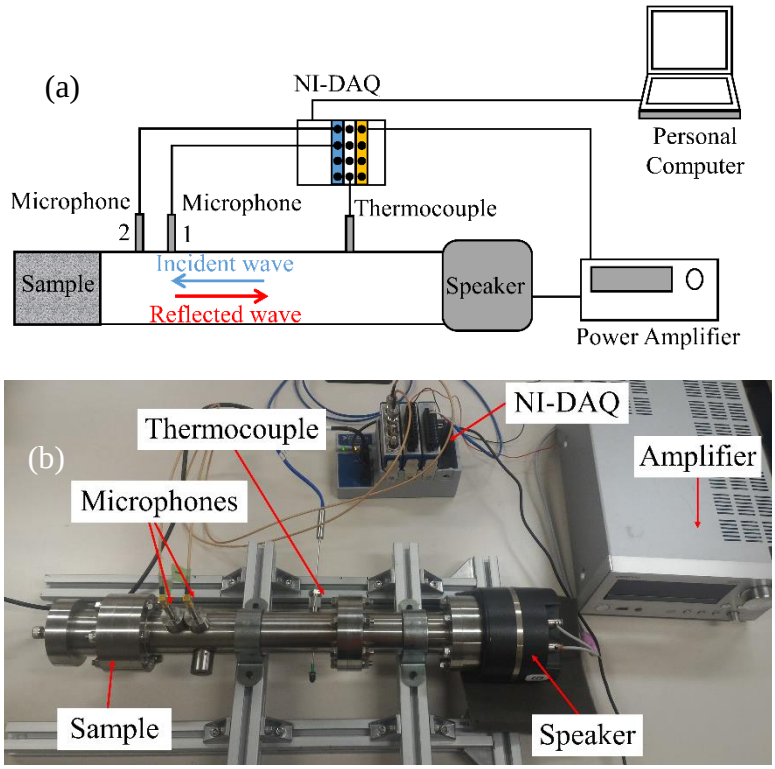

Figure 4.1. The (a) scheme and (b) photographs of the impedance tube setup

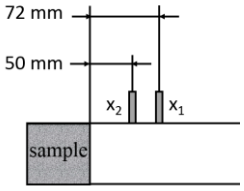

Figure 4.2. The location of microphone 1 and 2

The acoustic properties of the porous sample under normal incident soundwave were measured using an impedance tube with two microphone methods. The setup was designed according to ISO 10534–2. The setup consisted of a stainless steel tube, a speaker, power amplifier, two microphones, a thermocouple, and a National Instrument data acquisition device, NI-cDAQ 9174 as shown in Fig.4.1. The inner diameter of the tube was 25 mm and its total length is 335 mm. The porous sample was inserted to the sample slot in one end of the tube whereas a speaker was connected to opposite end as the

sound wave generator. The speaker was connected to an amplifier which then connected to the NI-DAQ 9263 and a PC. Two microphones were installed distances of 72 mm and 50 mm from the sample surface as illustrated in Fig. 4.2. The two microphones were connected to NI-DAQ 9234. A thermocouple was used to measure the air temperature inside the tube. The thermocouple was connected to NI-DAQ 9211. The frequency obtainable by the tube is limited by the diameter of the tube and the distance between the microphones as indicated by eq. (4.1) and (4.2)

$$f_{up} = \frac{0.586 c_a}{d_{IT}} \tag{4.1}$$

$$0.05 \frac{c_a}{l_{12}} < f_r < 0.45 \frac{c_a}{l_{12}} \tag{4.2}$$

which resulted in to 772 Hz < f_r< 6954 Hz. The frequency range shown in this report is limited between 800 Hz < f_{IT}< 6800 Hz.

Two LabView programs were used for the experiments. The first program generated white noise signal to the power amplifier. Power amplifier was connected to the speaker and initiate white noise inside the tube. Power magnification was conducted by turning the knob of the amplifier. The sound level of the white noise is kept 40 dB at maximum. The white noise then propagated toward the samples. Some of the incident wave on the sample surface was absorbed and the rest was reflected. The microphone 1 and 2 measured the pressure of the incident waves and reflected waves at the two locations. This pressure was recorded and processed by the second Labview program.

The acoustic properties of the samples, i.e. the normalized surface impedance, *Z*, the reflectance, R, Sound Absorption Coefficient, SAC, were calculated by using following steps. The pressure measured at the location of microphone 1 and 2 are given by

$$p_1 = p_{1i} + p_{1r} = A_i e^{i(\omega t - k x_1)} + A_r e^{i(\omega t + k x_1)} \tag{4.3a}$$

$$p_2 = p_{2i} + p_{2r} = A_i e^{i(\omega t - k x_2)} + A_r e^{i(\omega t + k x_2)} \tag{4.3b}$$

where ω is the angular frequency, k is the wave number, A_i and A_r are the pressure amplitudes of incident waves and reflected waves respectively. The transfer functions, H_1, H_2, and H_{12} are given by

$$H_1 = \frac{p_{2i}}{p_{1i}} = e^{ik(x_1 - x_2)} \tag{4.4}$$

$$H_2 = \frac{p_{2r}}{p_{1r}} = e^{-ik(x_1 - x_2)} \tag{4.5}$$

$$H_{12} = \frac{p_2}{p_1} = \frac{e^{-jkx_2} + e^{jkx_2}\left(\frac{A_r}{A_i}\right)}{e^{-jkx_1} + e^{jkx_1}\left(\frac{A_r}{A_i}\right)} \tag{4.6}$$

in this study, the H_{12} was obtained from H_{12} = $FFT_{cross12}$ / $FFT_{power11}$, where the $FFT_{cross12}$ is the fast Fourier transform (FFT) cross spectrum of pressure between Microphones 1 and 2 and $FFT_{power11}$ is the FFT power spectrum of pressure of Microphone 1. This H_{12} was calculated by the second LabView Program for each frequency, from 800 Hz to 6800 Hz with interval of 10. These transfer functions were used to calculate the reflectance, *R*, the sound absorption coefficient, *SAC*, and the normalized surface impedance, *z*, of the sample by using Eqs. (4.7)–(4.9). Normalized surface impedance *z* is the ratio of surface impedance, Z_i, to characteristic impedance of air, Z_0 (=$\rho_0 c_0$, where ρ_0 is the density of air and c_0 is the speed of sound), which is referred as impedance in further analysis.

$$R = \frac{A_r}{A_i} = \frac{H_{12} - H_1}{H_2 - H_{12}} e^{-2ik(x_1)} \tag{4.7}$$

$$Z = \frac{Z_l}{Z_0} = \frac{1+R}{1-R} \tag{4.8}$$

$$SAC = 1 - |R|^2 \tag{4.9}$$

4.2.3 Validation of the Impedance Tube

Validation of the impedance tube setup was conducted without any sample, i.e. the hardwall condition. The magnitude of transfer function obtained from the hardwall condition is shown in Fig. 4.3 (a) and (b) whereas the phase is shown in Fig. 4.4 (a) and (b). The magnitude of the transfer function have some peaks value related to standing

wave observed at the location of microphone 1 as the reference point, as shown in Fig. 4.3 (a). Because the location of Microphone 1 is x = 72 mm (location of the hard wall is x = 0), when 1/4 λ, 3/4 λ, and 5/4 λ (λ: wave length) are equal to 72 mm, the frequencies of the sound wave at c = 340 m/s should be f = 1181, 3542 and 5903 Hz, respectively. As comparison the transfer function using microphone 2 as the reference point, $H_{21} = FFT_{cross21}/FFT_{power22}$, shows peak at different frequencies. The calculated frequencies of standing wave for both microphone 1 and 2 as the reference points are listed in Table 4.3 and 4.4. This frequencies match with the peak frequencies from the measurements.

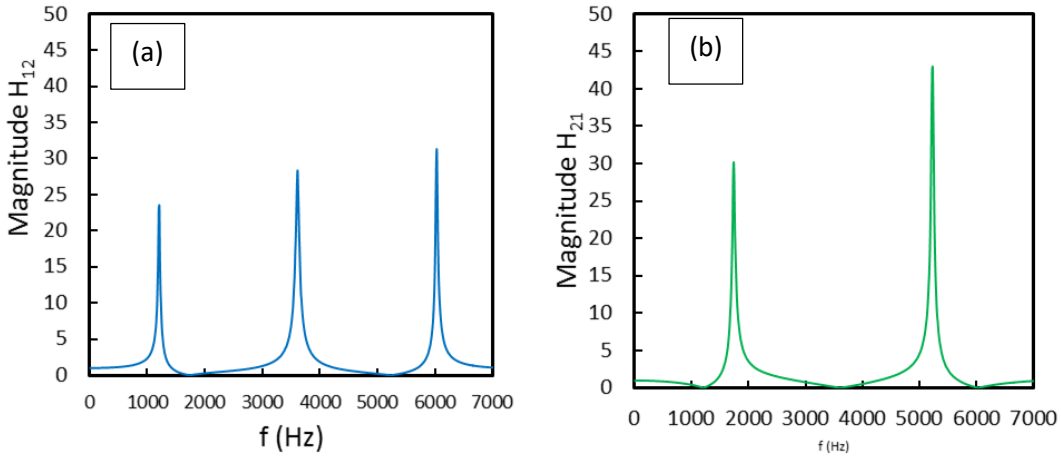

Figure 4.3. Magnitude of the transfer functions of (a) H_{12} and (b) H_{21} ($|H_{12}|$ and $|H_{21}|$) in Hardwall condition

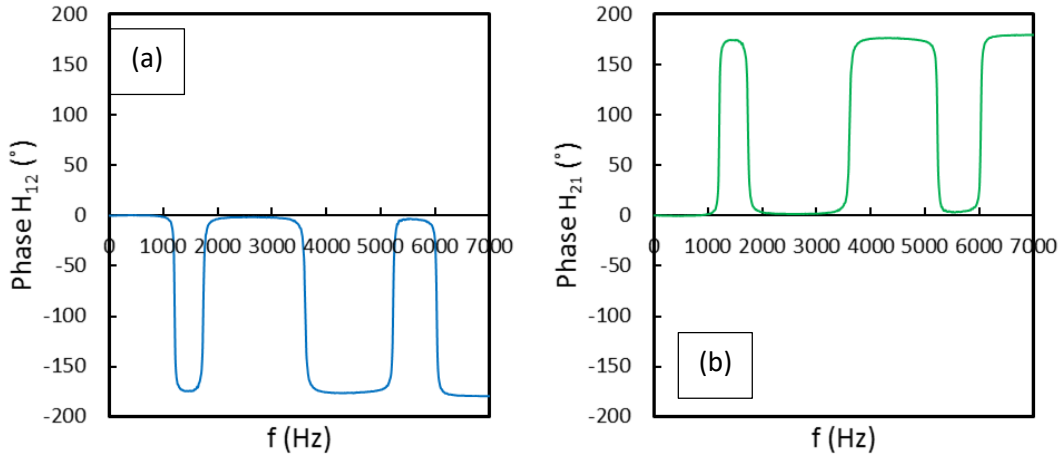

Figure 4.4. Phase of the transfer functions of (a) arg(H_{12}) and (b) arg(H_{21}) in Hardwall condition

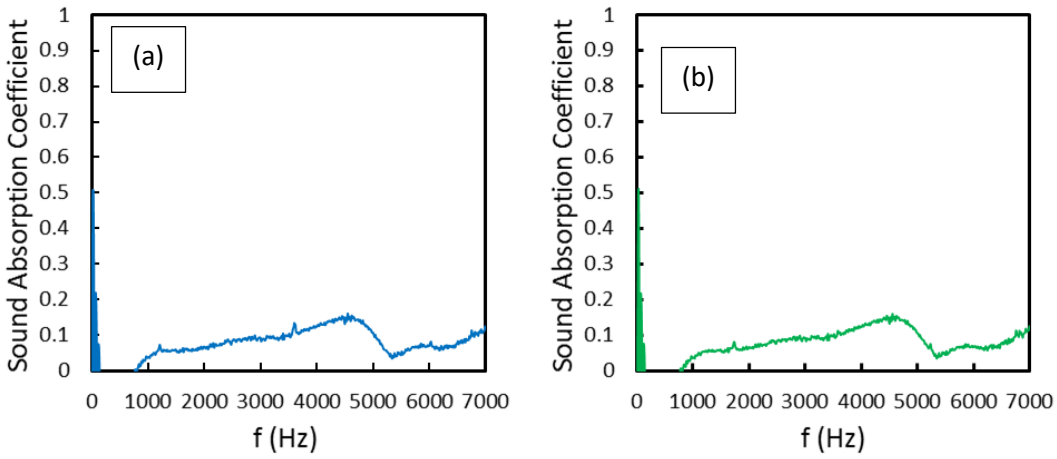

Figure 4.5. The hardwall SAC calculated using transfer function (a) H_{12} and (b) H_{21}

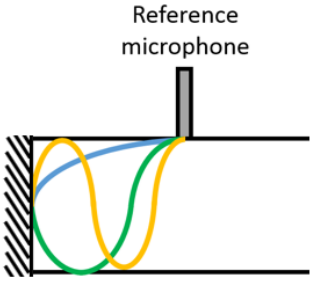

Figure 4.6. Standing waves using microphone location as reference point

Table 4.3 Frequency of standing wave when $\mathbf{x_1}$ set as the reference (H_{12}):

	f (Hz)	x_1 (m)	c (m/s)
1/4λ	1181	0.072	340
3/4λ	3542	0.072	340
5/4λ	5903	0.072	340
7/4λ	8264	0.072	340

Table 4.4 Frequency of standing wave when $\mathbf{x_2}$ set as the reference (H_{21}):

	f (Hz)	x_1 (m)	c (m/s)
1/4λ	1700	0.05	340
3/4λ	5100	0.05	340
5/4λ	8500	0.05	340
7/4λ	11900	0.05	340

The SAC of hardwall condition obtained using H_{12} and H_{21} are shown in fig. 4.5 (a) and (b). The ideal SAC of the hardwall condition should be zero as all of the incident waves should be reflected back by the hardwall and the impedance of the hardwall become infinity. However, in the actual system many deviation from the ideal case could occur inside an impedance tube as stated by Niresh et al. in ref. [16]. In our system, the hardwall SAC could be maintained below 0.2. The SAC tend to increase as the frequency increase, but a trough occurs around 6000 Hz. The reason behind this trough is not really well understood, but it might be related to the characteristic of the impedance tube or the phase difference of the microphones. Spikes of SAC were observed from both curves at the same frequency with the frequencies of the magnitude peak of the transfer functions. Therefore, these SAC spikes observed in hardwall condition are caused by standing wave occurred in reference of the location of the reference microphone.

4.3 Acoustic Model for Porous Material

The acoustic properties of the porous samples under normal incident soundwave were analyzed using some available models. The accuracy of the acoustic model to predict the acoustic properties were verified. Three acoustic models were used in this study:

4.3.1 **Delany-Bazley** [6]

Delany and Bazley used experimental acoustic data of glass fiber and mineral wools from the impedance tube to build two empirical equations to calculate the characteristic impedance and propagation constant of fibrous materials. The equations are given by

$$Z_c = \rho_0 c_0 \left\{1 + 0.0497 \left(\frac{f}{\sigma}\right)^{-0.754} - i0.0758 \left(\frac{f}{\sigma}\right)^{-0.732}\right\} \tag{4.10}$$

$$k = \frac{\omega}{c_0}\left\{0.160 \left(\frac{f}{\sigma}\right)^{-0.618} + i\left[1 + 0.109 \left(\frac{f}{\sigma}\right)^{-0.618}\right]\right\} \tag{4.11}$$

The main input parameter of the equations is only the flow resistivity. Thus, this model is relatively simple and straight forward. The surface impedance of the fibrous sample with thickness, *l*, was then calculated using equation (4.12)

$$Z_{l\,DB} = Z_c \ coth(kl) \tag{4.12}$$

For further discussion is this report, we used the normalized impedance i.e. the ratio between the surface impedance and the characteristic impedance of air, $Z = Z_l/Z_0$. Equation (4.8) then can be modified to calculate the reflectance, *R*, using known impedance to be

$$R = \frac{Z-1}{Z+1} \tag{4.13}$$

The SAC can be calculated using equation (4.9). In this project, we would like to verify the use of this model not only for our sintered fiber samples but also the foam samples.

4.3.2 **Sides** [17]

In this model, Sides et al. assumed fibrous material as stacked cylinders structure as shown in Fig. 4.7. They then built an acoustic model for the stacked cylinders based on the Biot theory [18]–[20]. Biot developed a theory for wave propagation in fluid saturated porous elastic material. The calculation requires four elastic coefficients that are usually obtained from measurements. However, the Biot theory does not include the detail of the porous structure i.e. it assumes that the medium is homogeneous and its porosity is uniform throughout. Thus, Sides et al. theoretically derived equations to calculate the four elastic coefficients for the stacked cylinder structure. The steps are provided below.

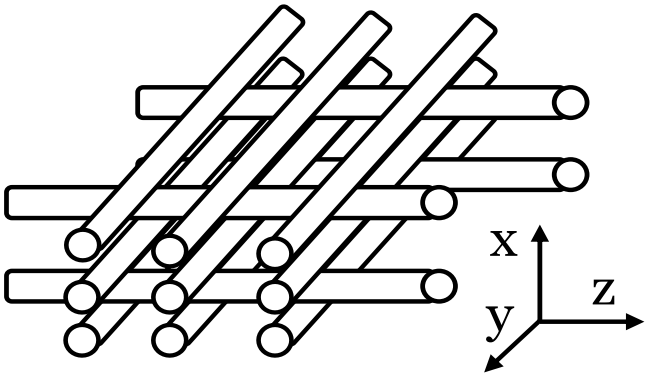

Figure 4.7. Stacked cylinders structure assumption used by Sides et al.

The dissipation inside a cylindrical pore for Poiseuille flow is given by

$$d_p = 8\pi\eta_0 F(\mu) \tag{4.14}$$

where η_0 is the viscosity of air and $F(\mu)$is a correction for the deviation from Poiseuille flow.

$$F(\mu) = -\frac{1}{4}\left[\frac{\mu\sqrt{j}T(\mu\sqrt{j})}{1-2/\mu\sqrt{j}T(\mu\sqrt{j})}\right] \tag{4.15}$$

where $\mu = a_0\sqrt{\omega\rho_0/\eta}$ and $T(\mu\sqrt{j}) = J_1(\mu\sqrt{j})/J_0(\mu\sqrt{j})$. J_1 and J_0 are Bessel functions of first and zero order and a_0 is the radius of the effective pore. The dissipation of a single pore per unit area is given by

$$d_{sg} = \frac{\phi d_p}{\pi a_0^2} = \frac{8\eta\phi F(\mu)}{a_0^2} \equiv bF(\mu) \tag{4.16}$$

where $b = 8\eta\phi/a_0^2$. The pore radius were calculated using the value of flow resistivity, σ_f, by using equation (4.17).

$$a_0^2 = 8\eta/\phi\sigma_f \tag{4.17}$$

By substituting the stress-strain relations isotropic medium, kinetic energy and dissipation functions into Lagrange's equations, then taking the divergence, the governing equations of the dilatational waves propagation inside fluid saturated porous elastic material can be obtained.

$$\nabla^2(Pe + Q\varepsilon) = \frac{\partial^2}{\partial t^2}(\rho_1 e) + bF(\mu)\frac{\partial}{\partial t}(e - \varepsilon) \tag{4.18}$$

$$\nabla^2(Qe + R\varepsilon) = \frac{\partial^2}{\partial t^2}(\rho_2\varepsilon) - bF(\mu)\frac{\partial}{\partial t}(e - \varepsilon) \tag{4.19}$$

From tedious derivation, four of Biot elastic coefficient, N, Q, A, R following equations can be obtained.

$$N = \frac{E_b}{1+\nu_b} \tag{4.20}$$

$$Q = (1 - \beta)K_f \tag{4.21}$$

$$A = \frac{2N\nu_b}{1-2\nu_b} + \frac{(1-\phi)^2}{\phi K_f} \tag{4.22}$$

$$R = \phi K_f \tag{4.23}$$

Where E_b is the Young's Modulus and ν_b is the Poisson ratio. The bulk modulus was then calculated using equation (4.24).

$$K_f = \gamma P_0 / \left[1 + \frac{2(\gamma-1)}{\mu\sqrt{j}}\frac{J_1(\mu\sqrt{j})}{J_0(\mu\sqrt{j})}\right] \tag{4.24}$$

Where P_0 is the equilibrium pressure and γ is the ratio of the specific heats of the fluid, $\gamma = C_p/C_v$.

The governing equation of wave propagation, equations (4.18) and (4.19) then can be solved using a method proposed by Biot. A periodic solution is assumed and the two dilatations are written as

$$e = a_s e^{-j(\omega t - kx)} \tag{4.25}$$

$$\epsilon = a_f e^{-j(\omega t - kx)} \tag{4.26}$$

k is a propagation constant. By solving the substitution of equation (4.25) and (4.26) to the governing equations, we can obtain.

$$k' = \pm\left[\frac{\omega^2 m_2}{R} + i\omega bF(\mu)\left(\frac{A+2N+R}{(A+2N)R}\right)\right]^{1/2} \tag{4.27}$$

Further derivation will provide the equation to calculate the characteristic impedance of fibrous material.

$$Z_c = \frac{K_f k'}{\omega \phi} \tag{4.28}$$

The surface impedance of the fibrous sample with thickness, l, was then calculated using equation (4.29)

$$Z_{l\,DB} = Z_c \ coth(-jk'l) \tag{4.29}$$

Unlike the Delany - Bazley model, Sides model is more elaborate and requires tedious calculation. Furthermore, the input parameters of this model includes the mechanical properties, thermal properties, physical properties and geometry related properties. In this study, Sides model was used for sintered fiber material.

4.3.3 **Lu** [11]

Lu et al. modeled foam material as cellular structure as shown in Fig. 4.8. For the acoustic analysis, this structure was further simplified as multi layers of perforated plates. Each of the perforated layers was analyzed using method made by Maa [21]. The impedance of a perforated plate and an air gap behind is the summation of the impedance of the orifice and the air gap. The impedance of the air inside the cell can be calculated as follows.

$$Z_f = -i\rho_0 c_0 \, cot(\omega \overline{D}/c_0) \tag{4.30}$$

where $\overline{D}$ is the thickness of the air gap. The impedance of the orifice can be calculated as follows.

$$z_a = \frac{32\eta t_p}{d^2}\left\{\sqrt{1+\beta^2/32} + \sqrt{\beta d/4t_p}\right\} + i\omega\rho_0 t_p\left\{1 + 1/\sqrt{9+\beta^2/2} + 0.85d/t_p\right\} \tag{4.31}$$

where t_p is the thickness of the plate, d is the diameter of the orifice, and β is the acoustic Reynold number that can be calculated by using equation (4.32).

$$\beta = \frac{d}{2}\sqrt{\frac{\omega\rho_0}{\eta}} \tag{4.32}$$

It should be noted that Eq. (4.31) is valid for $1 < \beta < 10$, thus, it is limited to a certain range of pore throat diameter and a range of frequency. The equation might fail for smaller pore throat diameter or lower frequency and larger smaller pore throat or higher frequency.

It is important to note that only some parts of sound waves incident on the open orifice area and the attenuated by the orifice and the air gap. The sound wave incident on the plate was reflected back. Thus the impedance of the orifice is corrected by divide equation (4.32) with open area ratio, $a_r = d^2/{D_c}^2$.

$$Z_a = \frac{32\eta t_p}{a_r d^2}\left\{\sqrt{1+\beta^2/32} + \sqrt{\beta d/4t_p}\right\} + \frac{i\omega\rho_0 t_p}{a_r}\left\{1 + 1/\sqrt{9+\beta^2/2} + 0.85d/t_p\right\} \quad (4.33)$$

The impedance of the system consists of one perforated plate and an air gap is given by

$$Z_{1\,layer} = Z_a + Z_f \quad (4.34)$$

To apply Maa analysis methods on the foam model i.e. cellular cells, the unknown geometric parameters were estimated using known pore size, pore throat size and porosity. In the first stage of simplified structure, the cell is in hexagonal shape. The volume of this cell can be calculated by $3\sqrt{3}D^2\overline{D}/8$. The depth of the hexagonal cell, $\overline{D}$, was then estimated from the spherical volume of the pore with diameter D to obtain $\overline{D} = 0.806D$. Next, to calculate the thickness of the plates, t_p, surrounding the cell calculation was made by using the known porosity value. The porosity of the cellular structure can be estimated as

$$\phi = 1 - \frac{[3D\overline{D} + 2(3\sqrt{3}D^2/8) - 8(\pi d^2/2)](t_p/2)}{3\sqrt{3}D^2\overline{D}/8} \quad (4.35)$$

The plate thickness t_p then can be calculated using equation (4.36)

$$t_p \approx \frac{(1-\phi)D}{3.55 - 6(d/D)^2} \quad (4.36)$$

To estimate the open area ratio $a_r = d^2/{D_c}^2$, the hexagonal cell was modeled as cylindrical cell of equal cross-sectional area, with diameter equals to $D_c = 0.909D$. Finally, total impedance of multilayers of perforated plates could be calculated by using parallel circuit analysis of impedance of the orifice and the air cavity as shown in illustrated in Fig. 4.9. The equation to calculate the impedance of a foam material with thickness, l, is given by

$$Z_d = Z_{a1} + \cfrac{1}{\cfrac{1}{Z_{f1}} + \cfrac{1}{Z_{a2} + \cfrac{1}{\cfrac{1}{Z_{f2}} + \cfrac{1}{\ldots + \cfrac{1}{Z_{aN} + Z_{fN}}}}}} \tag{4.37}$$

where N represents the number of perforated plates that can be obtained by rounding down the result of $l/(\overline{D} + t_p)$.

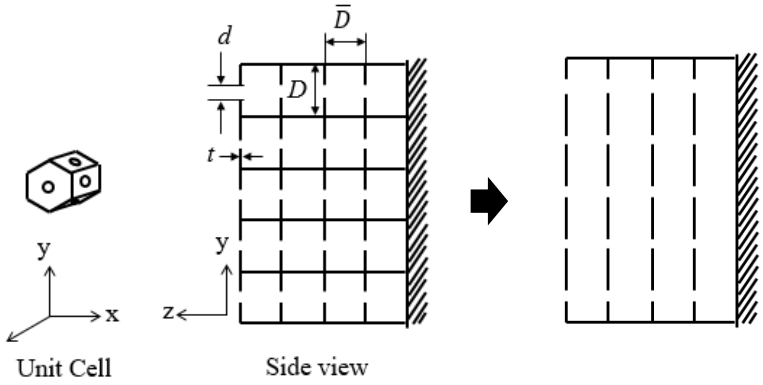

Figure 4.8. Modelling of foam material as multilayer perforated plates.

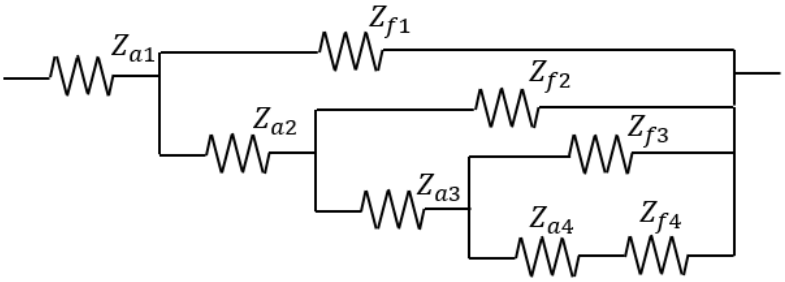

Figure 4.9. Analysis of the multilayer perforated plates as the parallel circuit of orifice impedance and air cavity impedance.

4.4 Results and Discussion

4.4.1 Measured Sound Absorption Properties

The acoustic properties obtained from impedance tube measurement setup are provided below. The results presented here are processed from transfer function using microphone 1 as the reference point (H_{12}).

A. Sintered fiber vs foam

Figure 4.10 shows the SAC and the impedance of the sintered fiber sample with ϕ = 80% and foam sample with ϕ = 81%. This figure indicates that there is some differences in sound attenuation inside sintered fiber sample and foam sample even though the porosity is similar.

The SAC of the sintered fiber increased along the increase of frequency. The fiber material was stainless steel that can be considered as rigid. Therefore, the relative velocity of air particle oscillating inside the void of the material and the zero velocity of the air at the fiber surface caused friction loss and viscous loss. Thus the kinetic energy of the air particle dissipated into heat to the fiber. The increase of the sound attenuation as the increase of the frequency was because at higher frequency the wavelength of the sound wave was shorter. Thus, the wavelength becomes equal to the length of the sample. Furthermore, two SAC spikes occurs at f = 2600 Hz and f = 5400 Hz while a shallow through occurs around f = 5500 Hz. Cumming stated that porous material with high flow resistivity are susceptible to measurement error such as due to air gaps around the sample [22]. Thus, the SAC spikes occurred for the sintered fiber might be attributed to the high flow resistivity value of the sintered fiber sample. Meanwhile, the reason of the through occurs around f = 5500 Hz is not identified. This trough is similar to trough occurred at 6000 Hz in hardwall condition. However, the sharp SAC due to the reference microphone spikes observed in

Hardwall condition around 1200 Hz, 3500 Hz, and 5900 Hz did not occur in the measurement of the sintered fiber sample.

On the other hand, the foam sample with ϕ = 81% provide a different trend of SAC. The SAC curve consists of peaks and troughs occur at some frequencies. The prominent peaks indicate that this foam sample acted like a resonator. The highest peak reached 1 at f = 1800 Hz. The trough around 6000 Hz and SAC spikes observed at hardwall condition did not occur. Furthermore, there is no SAC spikes occurs due to measurement error in sintered fiber sample case. Furthermore,

Further analysis of the impedance also reveal different acoustic attenuation characteristic of the two samples. Figure 4.10 (c) and (d) show the resistance, Re(z), of the sintered fiber sample and the cellular foam sample, respectively. The resistance of the sintered fiber sample with ϕ = 80% decreases at low frequency range and tend to be constant at higher frequency. On the other hand, the resistance of the foam sample with ϕ = 81% has a peak at 3500 Hz. Figure 4.10 (e) and (f) show the reactance, Im(z), of the sintered fiber sample and the cellular foam sample, respectively. The reactance of the sintered fiber sample was in negative values that exponentially approaches zero toward higher frequency range. Meanwhile, the reactance of the foam sample shows some zero cross point. Furthermore, the SAC peak occurs at the zero cross reactance point which is a characteristic of resonators.

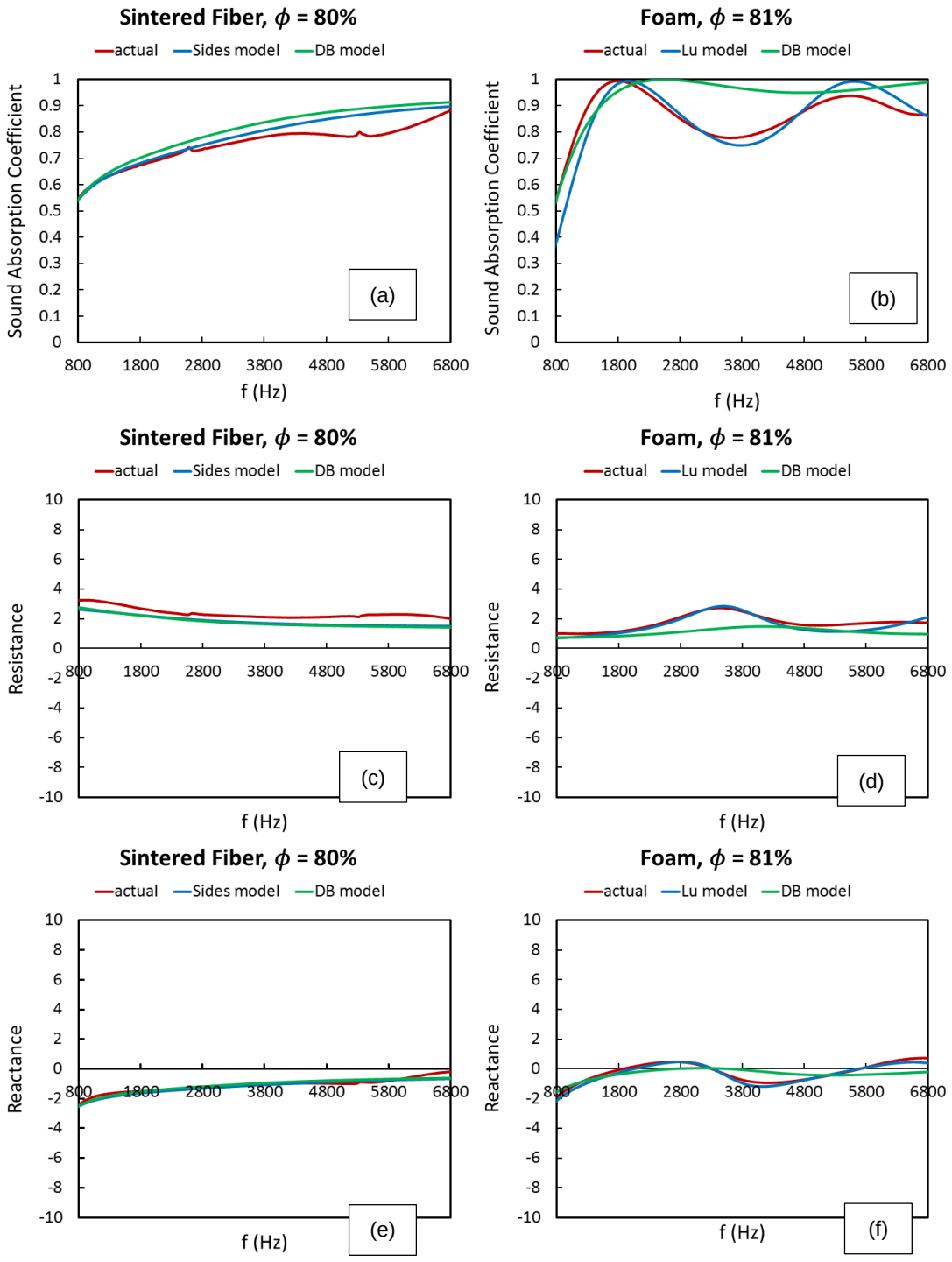

Figure 4.10. The SAC and Impedance of sintered fiber sample with ϕ = 80% vs. foam samples with ϕ = 81%.

B. Variation of porosity

Figure 4.11 shows the SAC of sintered fiber samples from the 1st batch with varied porosity. The SAC of hardwall condition is also included in Fig. 4.11. The SAC curve of every sintered fiber samples has a similar trend that is logarithmic increase toward higher frequency. Therefore, the sound attenuation mechanism was the same for every sintered fiber sample that is caused by viscous loss. Furthermore, the SAC curves are higher for the sample with higher porosity. Figure 4.11 also shows that an SAC trough around 5000 Hz for every sintered fiber sample that might be the characteristic of the hardwall. Similar to the sintered fiber sample with ϕ = 80%, SAC spikes also occur for the sample with ϕ = 78%, in slightly different frequencies, f = 2400 Hz and f = 5600 Hz. These spikes might also be caused by air gaps around the sample. In contrast, SAC spikes were not observed for the sample with ϕ = 65%. This sample might be well fitted into the slot.

Figure 4.12 shows the SAC of cellular foam samples with different porosity. The trend of SAC curve was different especially for the sample with ϕ = 96%. The SAC curves of the samples with ϕ = 81% and ϕ = 85% have prominent peaks and troughs, indicating the effect of resonance inside the cellular foam sample. On the contrary, the SAC trend of the sample with ϕ = 96% is more similar to the SAC trend of the sintered fiber sample that an SAC trough occurs around 5500 Hz. However, this trough is deeper than that observed for sintered fiber samples. The overall SAC curve of the sample with ϕ = 96% is the lowest out of the cellular foam samples.

The SAC spikes at 1200 Hz, 3500 Hz, and 5900 Hz in hardwall condition was not observed in the measurement results of all the porous samples. However, the trough around 6000 Hz occurred in the measurement of all the sintered fiber samples and the foam sample with ϕ = 96%.

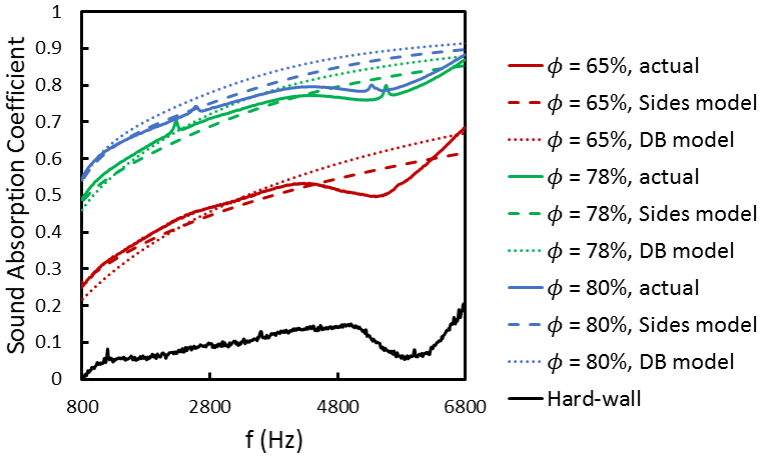

Figure 4.11. The SAC of sintered fiber samples with different porosity.

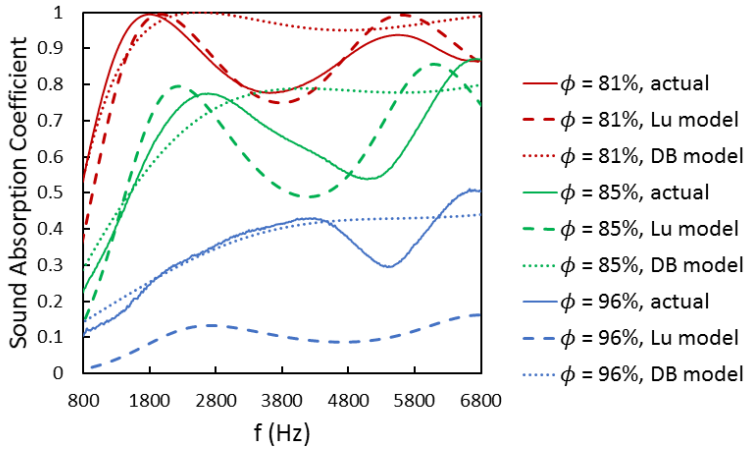

Figure 4.12. SAC of foam samples with different porosity.

C. Validation of the acoustic properties of fiber samples

In chapter 2, the X-Ray scan results indicated that the microstructure of sintered fiber samples from different batches was not uniform. The samples from the first batch have a homogenous structure whereas the second batch samples have a non-homogeneous structure. Therefore, the flow resistivity of the samples from different batches was in a different range as reported in chapter 3. In this chapter we show the difference of acoustic properties of the sintered fiber sample due to inhomogeneity of the microstructure. Figure 4.13 shows the SAC of the samples form the 1st batch with ϕ = 65% and ϕ = 80% and the samples from the 2nd batch porosity of which is ranging from 82% to 84%. The trend of SAC is the same for all the samples. This indicates that even there is some inhomogeneity inside the samples from new batch,

the sound attenuation characteristic is still the same with sample with another batch, i.e. by viscous loss. A trough occurred around 5000 Hz for every sample. Furthermore, some SAC spikes were also observed for every sample from the 2nd batch.

Furthermore, Fig. 4.13 shows that the SAC of the samples from the 2nd batch is lower than the sample from the 1st batch with ϕ = 80% even though the porosity of the 2nd batch sample is higher. Analysis of the sintered fiber samples from the 1st batch shows that higher porosity yields to a lower the flow resistivity. This low flow resistivity yields to a higher SAC. However, due to the inhomogeneity inside the 2nd batch samples, e.g. gathered fiber, the flow resistivity become higher. Thus, it is more difficult for air to flow through the samples from the 2nd batch. Likewise, it is more difficult for the sound waves to propagate into the new samples so that sound attenuation was lower. Moreover, it is shown that the sample with the highest porosity in the 2nd batch, sample 6 with ϕ = 84.24% did not provide the highest SAC among the new samples. The SAC curve of sample 6, ϕ = 84.24%, coincides with sample 4, ϕ = 83.84%. The highest SAC curve was attained by sample 3 with ϕ = 83.55%. Thus, the degree of inhomogeneity microstructure might vary even within samples from the 2nd batch.

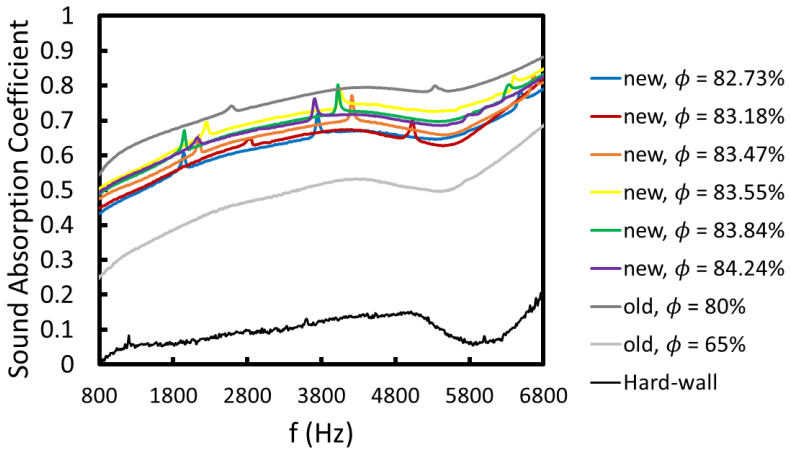

Figure 4.13. Sound absorption coefficient of sintered fiber samples from the 2nd batch with old sample with ϕ = 65%, ϕ = 80% and hardwall SAC as comparison

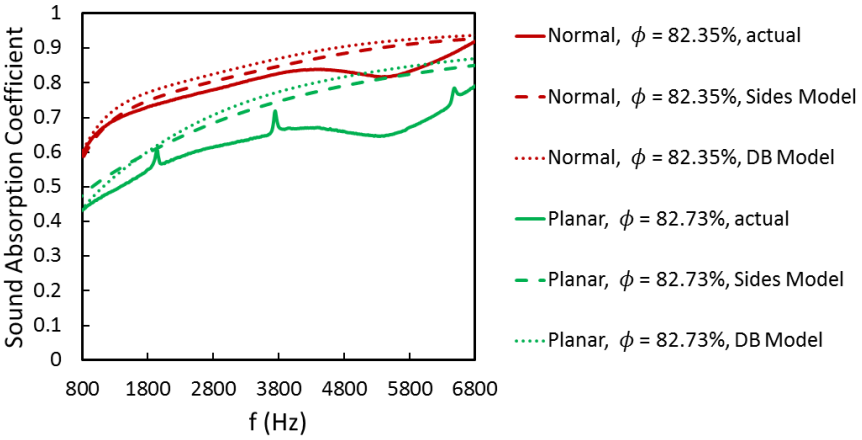

(a)

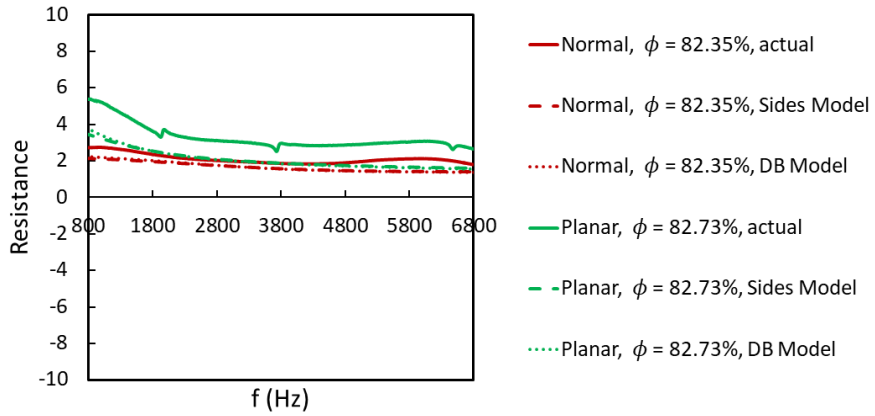

(b)

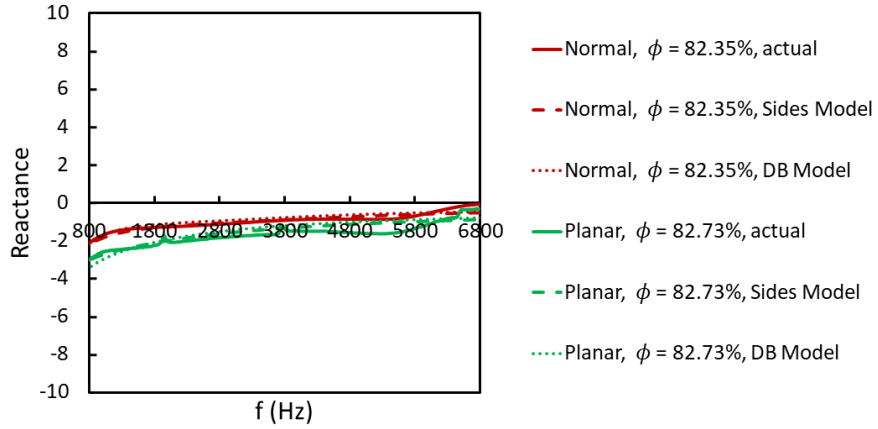

(c)

Figure 4.14. (a) The SAC, (b) resistance, and (c) reactance of the sintered fiber sample with normal and planar fiber direction

There is one sample from the 2nd batch that have a different fiber orientation i.e. the fiber direction is normal to the sample surface. As reported in chapter 3, this normal fiber sample has significantly lower flow resistivity than the other new samples with similar porosity as reported in chapter 3. The gap between these fibers forms a straight channel connecting the front surface and the back surface of the sample. Therefore, air can flow easier through the normal sample. For the acoustic measurement, this normal sample provided a better SAC curve than the other sample with planar fiber as shown in Fig. 4.14. This improved SAC might be closely related e to the lower flow resistivity of the normal sample that the sound wave can propagate further into the sample. However, the SAC curve of the normal sample has the same trend with the other sintered fiber samples. Thus, the sound attenuation inside sintered fiber samples is the same disregarding the orientation of the fibers. Thus, the sound attenuation inside all of the sintered fiber samples is caused by the viscous loss.

4.4.2 Accuracy of Model Prediction

Based on the analysis of the 1st batch of sample results, the DB and Sides model yielded to similar predictions of the SAC and impedance. The DB and Sides model were able to provide a good prediction of SAC and impedance of the sintered fiber sample as shown in Fig. 4.11, except the trough around 5000 Hz. Thus, the Sides model might be used for the prediction of acoustic properties of fibrous material with porosity as low as 65%, even though the model was developed to be valid only for materials with high porosity, $\phi \geq 90\%$ [17]. The Sides model is more elaborate as it was developed from the Biot theory. This model also considers the elasticity of the solid fiber material. However, the samples was made of stainless steel, thus, the fiber can be regarded as rigid. Therefore,

the consideration of the material of the fiber in the analysis might not improve the results. By way of contrast, the DB model is simple and straightforward.

Figure 4.14, shows that both DB model and Sides model failed to predict the acoustic properties of the samples from 2nd batch with planar fiber. As shown in fig 4.14, the discrepancies between the predicted and actual resistance of the planar sample was large, but not for reactance. The reason is that the sample was in homogenous and anisotropic. Thus, analysis using isotropic assumption in both Sides model and DB model was failed. Conversely, both models provided a more accurate SAC and impedance prediction for the sample with normal fiber orientation. The inhomogeneity inside the material i.e. the gathered fiber might not affect the void channel in normal condition very much. It is indicated that the Sides model and DB model can be valid for the sintered fiber material with normal fiber orientation.

The Lu model accurately predicted the acoustic properties of the foam sample with ϕ = 81% and ϕ = 85% as shown in Figs. 4.10 (b), (d), (f) and 4.12. Slight shift of the SAC peak frequency might be caused by the inaccuracy of the pore size and pore throat size of the samples because the two parameters were obtained from estimations as explained in chapter 2. However, this estimated pore size and pore throat size was shown to predict good overall predicted acoustic properties, especially for the sample with ϕ = 81%. The analysis using Lu model also successfully predicts the resistance peak around f = 3500 Hz and the zero cross points of reactance measured from experiments. This further proof that resonance inside these samples is prominent because the Lu model was developed based analysis of resonance in perforated plates. In contrast, the DB model could predict the maximum SAC value of the cellular foam material, but failed to predict the fluctuation of the SAC curve and over-predicted the SAC value at high frequency. The DB model also failed to predict the zero cross point of reactance.

A different results was obtained for the foam sample with ϕ = 96%. The Lu model under predicted the SAC of the sample. The reason was because the β parameter of the sample with ϕ = 96%, calculated from equation 4.32, does not lie within the valid range for Lu model i.e. 1 to 10. The β of each foam sample between 800 Hz and 6800 Hz is shown in Figure 4.15. The foam sample with ϕ = 96% has β larger than 10 at $f > 1800\ Hz$. However, at $f < 1800\ Hz$, even though the β was inside the applicable range of Lu model, the model also failed to give an accurate SAC prediction. The parameter β only includes d, pore throat size, that represent the structural dimension of the foam. This parameter might be not enough to characterize the sound attenuation mechanism occurs inside the material. In contrast, the DB model provided a good prediction of the SAC curve for the cellular foam sample with ϕ = 96%, except the trough around 5000 Hz. Thus, resonance might not occur inside this sample and the structure of this sample might not be correctly assumed as multilayer of perforated plates in Lu analysis. This different mechanism cannot be determined only based on the pore throat size of the foam material as considered in β.

Figure 4.16 shows the averaged SAC within 800 Hz up to 6800 Hz of every sample obtained from experiments and model calculation as a function of flow resistivity. The relation between the flow resistivity and the averaged SAC will be discussed further in 4.43. The triangle points represent the foam samples whereas the square points represent the sintered fiber samples. The averaged SAC of the fiber sample with higher flow resistivity and lower porosity was accurately predicted by the Sides model even though this model was developed for sample with high porosity close to 1. Meanwhile, the DB model overestimated the averaged SAC of all the samples, not only the sintered fiber samples but also the foam samples. For the foam sample with ϕ = 81% and ϕ = 85%, the β of which was within 1 to 10, the averaged SAC obtained from experiments coincides

with the Lu prediction. In contrast, the actual averaged SAC of the sample with ϕ = 96% was 3 times larger than the Lu prediction. As previously mentioned, the beta parameter for this sample is out of the valid range for the Lu model. Thus, Lu model cannot be used to predict the acoustic properties of this sample. For this sample, the DB model also failed to predict the averaged SAC.

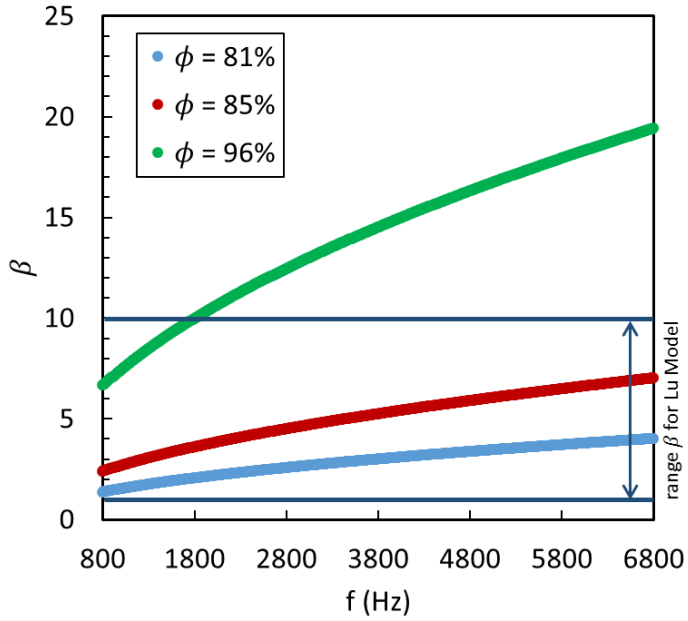

Figure 4.15. (a) The β for each foam samples within 800 $Hz < f <$ 6800 Hz

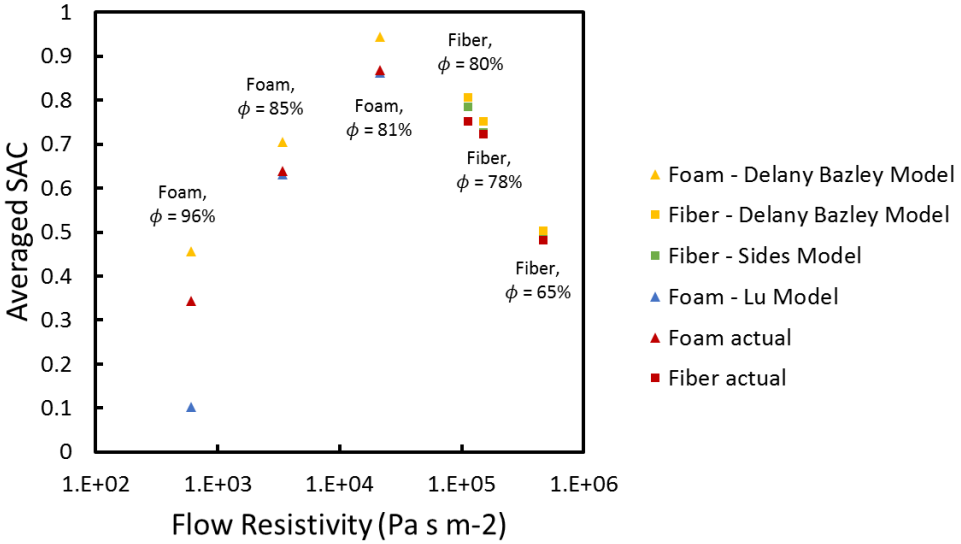

Figure 4.16. The averaged sound absorption coefficient, SAC_{ave}, of the samples.

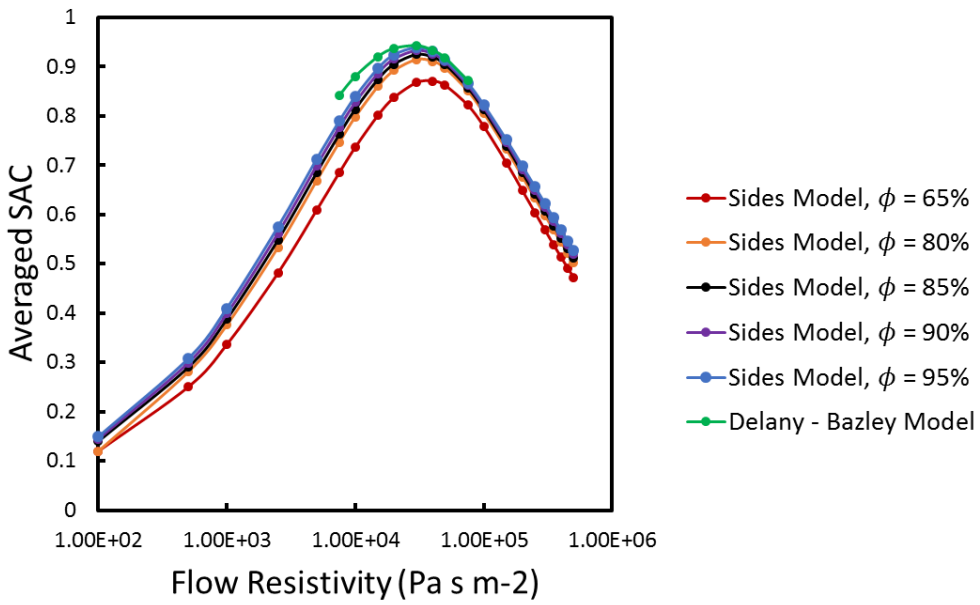

Figure 4.17. Relation between flow resistivity, σ, and model predicted SAC_{ave}.

4.4.3 Effect of Flow Resistivity on the Acoustic Properties

The relation between flow resistivity and the acoustic properties of porous metal was then investigated. Flow resistivity is considered to be a good parameter for the prediction of the acoustic properties of porous materials [23]. Figure 4.16 shows that the averaged SAC for foam and fibrous samples is a function of flow resistivity. In this figure we only include the sintered fiber from the 1st batch as the structure is relatively isotropic and homogenous. As the flow resistivity increased to 2×10^4 Pa s m^{-2}, the SAC_{ave} increased until the averaged SAC reach 0.87. The foam samples lies within this low flow resistivity range. As the flow resistivity increase, the averaged SAC decrease. The sintered fiber samples lies in this range.

The SAC_{ave} obtained from Delany – Bazley and Sides model for various flow resistivity values is shown in Fig. 4.17. In Fig. 4.17, the SAC_{ave} obtained from the Delany – Bazley model is plotted within a flow resistivity range, 2000 Pa s m^{-2} to 80000 Pa s m^{-2},which is the range of the flow resistivity of fibrous material they used to build the model.

For the Sides model, the flow resistivity was varied for some constant value of porosity ranging from 65% to 95%. Every curve of SAC_{ave} in Fig. 4.17 indicates the same trend with Fig. 4.16. The SAC_{ave} increased as the flow resistivity increased until a maximum point. After the peak, the SAC_{ave} decreased as the flow resistivity increase further. The peak of SAC_{ave} shifted slightly for every porosity values. The SAC_{ave} curve of DB model coincide with the Sides model curve with ϕ = 95%. The Sides model based SAC_{ave} curve become lower as the porosity decreased.

Low flow resistivity indicates that the sound wave could easily propagate through the porous material. Thus, the sound wave sustains small attenuation inside the porous material. As a result, the sound attenuation coefficient is low when the flow resistivity low. As the flow resistivity increase, the resistance for the sound propagation inside the material increase. Hence, the sound wave sustained more attenuation. However, further increase of the flow resistivity provides higher resistance for sound propagation inside the material. This condition can be interpreted in the following ways. One interpretation is that the sound wave cannot penetrate far into the porous material, and thus the attenuation occurs only near the surface of the porous material. The other is that the flow resistivity of the porous material is so high that the incident sound wave is reflected on the surface without being attenuated.

Furthermore, the comparison of the SAC of normal and planar samples in Fig. 4.14 shows that the normal sample with σ = 87696 Pa s m^{-2} yielded to a higher SAC curve than the planar sample with σ = 162846 Pa s m^{-2}. This flow resistivity value of 80000 Pa s m^{-2} is located around the optimum range of flow resistivity indicated in Fig. 4.16. Thus, the relation between SAC and the flow resistivity in the case of inhomogeneous material might be approached in a similar way to the homogeneous material.

The relation between flow resistivity and averaged SAC shown in Fig. 4.16 and Fig. 4.17 could be useful for rough estimation on the performance of porous sound absorbers. For the type of material used in this research, the flow resistivity from 20000 Pa s m^{-2} to 40000 Pa s m^{-2} will provide the best SAC. However, the mechanism of sound wave attenuation in porous materials could depend on the types of porous structure and the sound wave frequency. The flow resistivity could not predict this SAC distribution of each porous material in wide range of frequency. Furthermore, by Lu et al. stated that the flow resistivity correlation with the porosity and the pore size of foam material is poor [11]. Furthermore, the flow resistivity obtained from the pressure drop of fluid flow is related to the viscous loss effect. Thus, flow resistivity could accurately predict the SAC of porous material inside where only viscous and friction loss are the main sound attenuation mechanism. Thus, flow resistivity based DB empirical model cannot be used for foam material prediction.

4.4.4 Sound Attenuation Mechanism inside Porous Material

The measured acoustic properties of the foam samples indicated that variation of structure inside the material could lead to different mechanism of sound propagation. Visual based characterization reported in chapter 2 indicates that the pores inside every foam sample are interconnected. However, the reticulation rate might be varied. Thus, the sound attenuation varied for the foam samples as Doutres et al. stated that the foam sample with high reticulation rate acted more similar to fibrous material [15].

The acoustic properties of the sample with ϕ = 81% and ϕ = 85% indicated that the pore inside the material acted as resonator. Thus, it can be interpreted that these sample has low reticulation rate so that the each pores could be regarded as independent cells that act as sound resonator. Conversely, the acoustic properties of the sample of the foam

sample with ϕ = 96% does not indicate the significant effect of resonance. The SAC of this sample has the same characteristics with the fibrous samples. Thus this foam sample might have high reticulation rate. Thus, the viscous loss was the dominant mechanism of sound attenuation inside the foam samples with ϕ = 96%.

In the case of fibrous material, the sound attenuation characteristic was the same for every sample, even for the fibrous sample with homogenous structure, samples with inhomogeneous structure, and the sample with normal fiber orientation. The void channel inside the fibrous samples was formed between the fibers. Thus, the channel was in the form of interconnected ducts. When the sound wave propagates in the void channels, it causes air particles to oscillate. Because the metal fibers are rigid, the relative velocity of an air particle to the metal fiber causes the loss of kinetic energy of the air particle, resulting in the heat dissipation and the sound attenuation. The mechanism is similar to the sound attenuation inside the foam sample with high reticulation rate. However, the sound attenuation inside this foam sample was lower than the sintered fiber samples because the pore size and channel dimension are larger and the surface area of the solid is smaller than those of the fibrous sample. As a results, the viscous loss was lower than those of the fibrous sample.

Direct comparison of the SAC curve between the foam sample with ϕ = 81% and the fibrous sample with ϕ = 80% could provide design guideline for sound absorbers. Even the mass and porosity of both samples is similar, the experimental result suggest that the foam sample with ϕ = 81% performed better than the fibrous sample with ϕ = 80% for a specific weight limitation. Furthermore, the foam sample with ϕ = 81% performed the best among the all samples because it attained the highest SAC (SAC $\approx$ 1) and provided the highest SAC curve in the entire frequency range.

4.5 Conclusion

In this study, the viscous loss and resonance was observed as the sound attenuation mechanism inside porous material. The sound attenuation due to resonance was prominent inside the foam material consists of pores separated by wall which resembling aggregated cells. However, the foam material which consisted of reticulated structure cannot accommodate the resonance inside the pores as each pore was highly connected. Conversely, sound attenuation due to viscous loss occurred inside such foam materials. The sound attenuation inside the sintered fiber material was due to viscous loss for both planar and normal fiber orientation. Viscous loss was also the main sound attenuation mechanism both in homogenous and inhomogeneous material.

Regarding modeling, the DB model, which considered only flow resistivity in the calculation, provided accurate predictions for the acoustic properties of fiber samples with homogenous structure and the foam material with high porosity. The relatively simple DB model also provided a similar prediction with the Sides model, even though the Sides model is more elaborate in the calculation. However, both the model failed to provide an accurate prediction for the fiber samples with inhomogeneous structure. Therefore, DB model is preferable for fast analysis of the sintered fiber material with homogenous structure. The DB model also could provide an estimation of the maximum SAC range for the foam sample but failed to predict the peaks and trough. On the other hand, the acoustic properties of the foam sample with cellular structure can be accurately predicted using acoustic model for cellular material developed by Lu et al.

The relation between flow resistivity and averaged SAC was also investigated. The averaged SAC increased as the flow resistivity increased until it attaining a maximum value, and then started to decrease as the flow resistivity further increase. Flow resistivity was closely related to viscous loss occurs as the air flow through porous material structure.

Thus, the flow resistivity could be used for the accurate analysis of sound attenuation inside porous material if the viscous loss is the dominant mechanism. Flow resistivity, however, cannot be used for the acoustic analysis of porous sample with resonance as the dominant sound attenuation mechanism.

Furthermore, porous material with similar porosity value might yield to a different sound attenuation characteristic. The porosity does not provide detailed information on the structure. Thus information on porosity only cannot be used for predicting the acoustic properties of porous material. However, this condition could serve as a guideline for design process. For a limited mass for porous material and a given material, the structure of the porous material can be chosen to satisfy the desired sound attenuation profile.

4.6 References

[1] M. A. Kuczmarski and J. C. Johnston, "Acoustic Absorption in Porous Materials," *NASA/TM—2011-216995*.

[2] J. P. Arenas and M. J. Crocker, "Recent Trends in Porous Sound-Absorbing Materials," *J. Sound Vib.*, vol. 44, pp. 12–18, 2010.

[3] T. J. Lu, A. Hess, and M. F. Ashby, "Sound absorption in metallic foams," *J. Appl. Phys. J. Acoust. Soc. Am*, vol. 85, no. 123, 1999.

[4] D. L. Sutliff and M. G. Jones, "Low-Speed Fan Noise Attenuation from a Foam-Metal Liner," *J. Aircr.*, vol. 46, no. 4, pp. 1381–1394, 2009.

[5] D. L. Sutliff, M. G. Jones, and T. C. Hartley, "High-Speed Turbofan Noise Reduction Using Foam-Metal Liner Over-the-Rotor," *J. Aircr.*, vol. 50, no. 5, pp. 1491–1503, 2013.

[6] M. E. Delany and E. N. Bazley, "Acoustical properties of fibrous absorbent materials," *Appl. Acoust.*, vol. 3, no. 2, pp. 105–116, 1970.

[7] Y. Miki, "Acoustical properties of porous materials - Modifications of Delany-Bazley models-," *J. Acoust. Soc. Jpn.*, vol. 11, no. 1, 1990.

[8] T. Komatsu, "Improvement of the Delany-Bazley and Miki models for fibrous sound-absorbing materials."

[9] W. Chen, T. Chen, F. Xin, X. Wang, X. Du, and T. J. Lu, "Modeling of sound absorption based on the fractal microstructures of porous fibrous metals," *JMADE*, vol. 105, pp. 386–397, 2016.

[10] J.-F. Allard and N. Attala, *Propagation of Sound in Porous Media*, Second Edi. A John Wiley and Sons, 2009.

[11] T. J. Lu, F. Chen, and D. He, "Sound absorption of cellular metals with semiopen cells," *J. Acoust. Soc. Am.*, vol. 108, no. 4, pp. 1697–1709, 2000.

[12] Y. Kawasima, "Sound Propagation in a Fibre Block as a Composite Medium," *Acustica*, vol. 10, no. 208, p. 217, 1960.

[13] K. Attenborough and A. Walker, "Scattering Theory for Sound Absorption in Fibrous Media," vol. 49, 1971.

[14] L. L. Beranek, "Acoustical Properties of Homogeneous, Isotropic Rigid Tiles and Flexible Blankets," *J. Acoust. Soc. Am.*, vol. 19, no. 4, pp. 556–568, 1947.

[15] O. Doutres, N. Atalla, and K. Dong, “Effect of the microstructure closed pore content on the acoustic behavior of polyurethane foams,” *J. Appl. Phys.*, vol. 110, no. 6, 2011.
[16] J. Niresh, S. Neelakrishnan, and S. Subha Rani, “Investigation and correction of error in impedance tube using intelligent techniques,” *J. Appl. Res. Technol.*, vol. 14, no. 6, pp. 405–414, 2016.
[17] D. J. Sides, K. Attenborough, and K. A. Mulholland, “Application of a Generalized Acoustic Propagation Theory to Fibrous Absorbents,” *J. Sound Vib.*, vol. 19, no. 1, pp. 49–64, 1971.
[18] M. A. Biot, “Theory of Propagation of Elastic Waves in a Fluid-Saturated Porous Solid.,” *J. Acoust. Soc. Am.*, vol. 28, no. 2, p. 13, 1956.
[19] M. A. Biot and D. Willis, “The elastic coefficients of the theory of consolidation,” *J. Appl. Mech.*, vol. 24, pp. 594–601, 1957.
[20] M. A. Biot, “Mechanics of Deformation and Acoustic Propagation in Porous Media,” *J. Appl. Phys.*, vol. 33, no. 4, pp. 1482–2495, 1962.
[21] D.-Y. Maa, “Microperforated-Panel Wideband Absorbers*,” *Noise Control Eng. J.*, vol. 29, pp. 77–84, 1987.
[22] A. Cummings, “Impedance tube measurements on porous media: The effects of air-gaps around the sample,” *J. Sound Vib.*, vol. 151, no. 1, pp. 63–75, 1991.
[23] D. A. Bies and C. H. Hansen, “Flow resistance information for acoustical design,” *Appl. Acoust.*, vol. 13, no. 5, pp. 357–391, 1980.

CHAPTER 5

Sound Attenuation by Porous Metal inside a Flow Duct

In this chapter, the sound attenuation of the porous material was investigated inside a flow duct. The sample was inserted in the wall of the duct and there air flow could be generated inside the duct. These experiments represent better the condition inside the jet engine. The acoustic properties of the porous sample from impedance tube experiments and from flow duct in the absence of air flow were compared. Then, the effect of the air flow and air speed to the sound attenuation was investigated.

5.1 Introduction

The sound attenuation characteristic by porous metal under normal incident sound waves was reported in chapter 4. It was reported that the structure of the porous metal affect the sound attenuation performance. The foam sample with ϕ = 80% provided the best sound attenuation in the Impedance tube (IT). However, unlike the IT, in the actual application, the porous liner will be attached in the wall of the duct of the combustor or the exhaust duct of the low pressure turbine. Furthermore, air flow existed inside the jet engine. Therefore, there might be complex interplay between the sound wave, air flow, and the structure of porous metal. As a consequence, the sound attenuation by porous metal inside the actual jet engine might be different from the IT case.

Some researchers have also investigated the sound attenuation performances of porous materials for aircraft noise reduction. Nordin et al. [1] investigated the acoustic performance

of hybrid nickel foam and perforated metal structure inside a high-temperature duct to represent the conditions inside the hot stream areas of jet engines. Sutliff et al. [2], [3] investigated the performance of cobalt foam which was used as an acoustic liner positioned above the rotor to reduce fan noise. In 2018, Knobloch et al. [4] investigated the performance of ceramic fiber materials to reduce the noise from auxiliary power units (APUs). These researchers have successfully demonstrated that the porous metals could yield to the reduction of sound pressure level of the noise. Thus, porous material is potential for acoustic liners in jet engine. However, from these researches, the noise reduction mechanisms, especially, the interplay between the porous structure, sound wave propagation, and fluid flow for noise reduction have not been understood yet. The understanding of this interplay is critically important to predict the sound absorption properties of porous metals in jet engine and to design porous-metal-based acoustic liners. Thus, a more fundamental research to investigate the sound attenuation by porous metal in the presence of flow should be conducted inside a flow duct.

A flow duct (FD) setup is widely used to characterize the sound attenuation of Helmholtz resonator based acoustic liners [5]–[7]. Helmholtz resonator liner consisted of perforated layer backed by air cavity inside a cell. The cell is usually in the shape of hexagonal, i.e. honeycomb liner, or square [8]. The resonance characteristic of this device makes it effective to reduce noise in a narrow range of frequency. Therefore, this type of liner is widely used to reduce fan noise. However, even though the sound attenuation ability of the resonator based acoustic liner is well known, the basic knowledge of the impedance of the liner is not well understood yet.

Currently, there is no standard for the FD setup for measuring acoustic properties of acoustic liners. Each research groups in the world is using different size of FD and different impedance eduction methods [6], [7], [9]–[12]. These different FD dimension and eduction

methods might lead to different results. Furthermore, the improvements of impedance eduction methods is still being developed to obtain the impedance of the resonator liner [13]–[18]. Moreover, some researcher is trying to visualize the condition inside FD by several method such as Particle image velocimetry (PIV) or frequency modulated Doppler global velocimetry (FM-DGV) [19], [20]. Some numerical simulation was conducted to further understand the mechanism of the sound attenuation due to a resonator liner [21], [22].

The porous liner might have a different sound attenuation mechanism from the resonator liner. Resonator acoustic liners with cells act as locally reacting liner, that the impedance is the same in the FD and IT. In contrast, porous material might act as either locally reactive or non-locally reactive [23]–[25]. The acoustic properties inside the IT could be compared to that inside FD. If the FD results are similar to the IT results, then it could be interpreted that the sample acts similarly to a locally reactive liner. Furthermore, the acoustic measurement of porous metal inside FD might help to understand the sound attenuation mechanism by porous material in the presence of air flow.

In the case of the resonator acoustic liner, the sound attenuation mechanism was further investigated by using numerical simulation. Tam et al. conducted numerical simulation to study the cause of acoustic energy dissipation without grazing flow [26]. They found that at low Sound Pressure Level (SPL) the sound attenuation of resonator liner is by viscous loss due oscillatory boundary layer around the opening of the resonator. At higher SPL, the dissipation was due to vortex shedding. On the other hand, simulation conducted by Enomoto et al. [22] showed that when the air speed inside the flow duct is low, 0 Ma and 0.1 Ma, the acoustic energy dissipation was due to viscous loss on the neck of the resonator. This shows the mechanism of how a resonators cause sound dissipation. However, at higher air speed, 0.2 Ma and 0.3 Ma the energy dissipation was due to vortex generated on the downstream corner of the resonator opening. This paper also indicated that the acoustic liner might also produce

additional sound. Another paper by Tam et al. also indicated the same phenomena that the resonator liner could generate self-noise [21]. However, in the case of porous material the sound attenuation mechanism, especially under grazing flow, should be verified.

In this research, the acoustic properties of the porous metal were measured inside a flow duct with a rectangular cross-section. The porous sample was attached on one of the walls of the flow duct. The air speed inside the flow duct was varied from 0 Ma up to 0.3 Ma. The Reflection, Transmission, and Sound attenuation coefficient was calculated using the scattering matrix method. Furthermore, the impedance of the sample was educed using a method based on the Pridmore - Brown equation. These methods were usually used for locally reacting liner, i.e. the resonator types. The sound attenuation characteristics of the porous metal samples inside the FD without flow were compared to IT results. Then, the effect of air speed on the sound attenuation by the porous samples was observed.

5.2 Experimental Methods

5.2.1 Sample

The slab samples were used for the acoustic properties measurement inside the flow duct. The slab samples were 280 mm in length, 60 mm in width, and 30 mm in thickness as illustrated in Fig. 5.1 and shown in Fig. 5.2. Two sintered fiber samples and two foam samples were used as listed in Table 5.1. The sintered fiber samples for the FD were from the first batch. Furthermore, every sample was made of stainless steel.

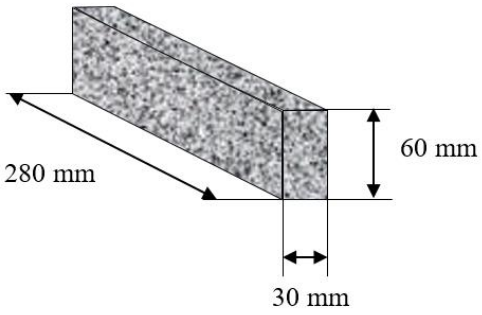

Figure 5.1. Dimension of the cylindrical and slab samples.

Figure 5.2. Photographs of some slab samples

Table 5.1 The properties of cylindrical samples

Sample	Fiber diameter (mm)	Pore size (mm)	Pore Opening Size (mm)	Porosity
Sintered Fiber				
1	0.03	-	-	65%
2	0.03	-	-	80%
Foam				
MF-80A	-	0.40±0.04	0.15±0.01	81%
MF-40	-	0.60±0.06	0.27±0.02	85%

5.2.2 Flow Duct Setup

The acoustic properties of the porous sample with grazing flow were measured in a flow duct setup shown in Fig. 5.3 (a) and (b). The flow duct has a rectangular cross section with dimension 60 mm x 80 mm as shown in the inset of Fig. 5.3 (a). The duct consisted of three sections: upstream, sample, and downstream. The porous sample was inserted in the slot available in one side of the duct wall illustrated in the inset of Fig. 5.3 (a). The test section length is 300 mm and the effective length of the sample windows is

280 mm. The height of the sample window is 60 mm. At both end of the duct, an anechoic termination was attached to reduce external noise in the duct.

The air flow was generated using a compressor attached in the inlet of the duct before the anechoic termination. The flow rate of the air was maintained and controlled using a regulatory valve. The maximum air flow velocity obtainable in the duct is 0.3 Ma measured in the center of the duct. The air speed for the experiment was varied to be 0Ma, 0.1 Ma, 0.2 Ma, and 0.3 Ma.

Two speakers were used in the setup, speaker A in the upstream section and speaker B in the downstream. The use of two speakers is required for the acoustic properties calculation. Furthermore, microphones were installed to record the pressure inside the flow duct in every sections of the FD: in the upper surface of the upstream section, in the upper surface of the downstream sections, and the side surface opposite of the sample surface. The seven microphones installed in both the upstream and downstream section as shown in Fig. 5.3 (a). Data from these microphones was used for the data processing as explained below. Furthermore, additional 16 microphones were installed on the opposite wall of the sample surface to detect the decrease of the pressure amplitude along the sample section. These face to face microphones are explained in more detail in the appendix.

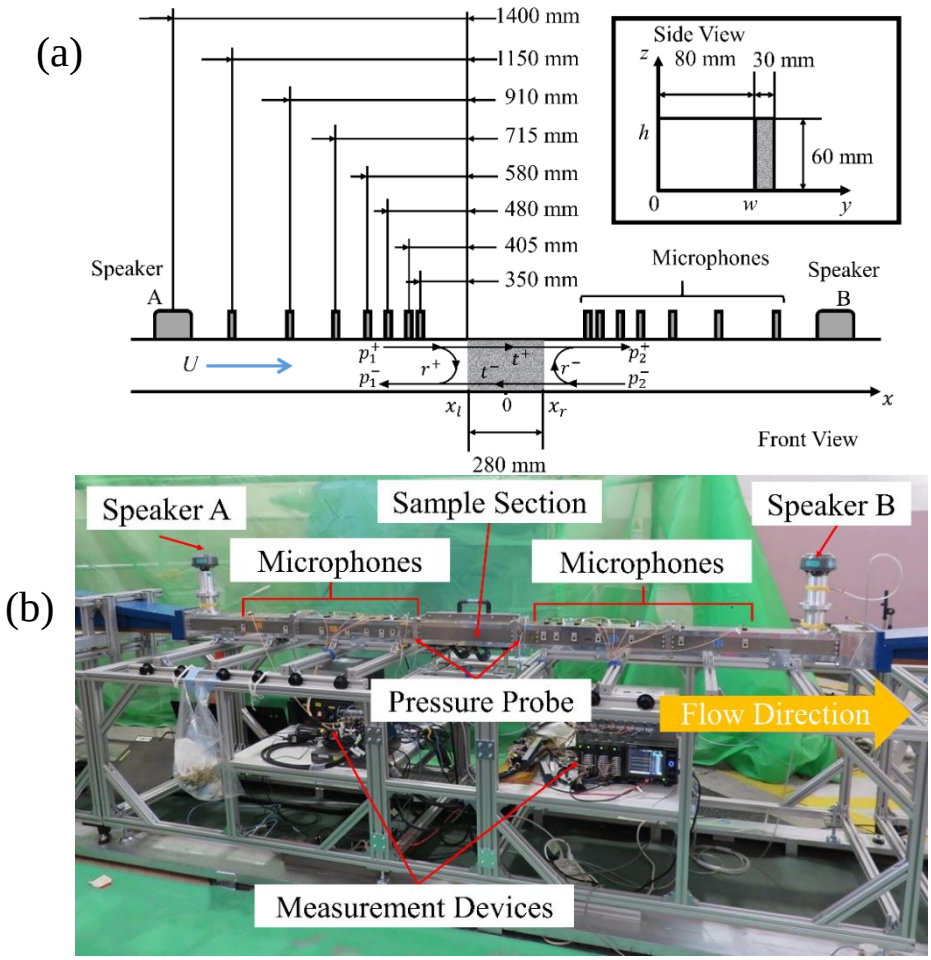

Figure 5.3. The scheme (top) and photograph (bottom) of the flow duct setup.

Sound generation by the speaker was accomplished by generating a single frequency sine wave using LabView. The signal was then inputted to the amplifier connected to the speaker. Power magnification of the amplifier was done by turning the knob of the amplifier. The *f* range of the FD is from 250 Hz to 2000 Hz, with interval 50 Hz between each measurement. For each frequency, the soundwave was generated by speaker A and speaker B alternately. The data from the microphones were recorded by using the National Instrument Data Acquisition System and a PC. The pressure drop data and environmental conditions were collected using PLATFORM GL 700 manufactured by GRAPHTECH. The details of the flow duct setup is also provided in Ref. [27], [28].

The reflection, transmission, and sound attenuation coefficient was calculated using scattering matric method[5]. Pressure data from the microphones were processed to obtain the pressure function, Eq. (5.9) – Eq. (5.12) at each duct section.

$$p_{1a}(x) = p_{1a}^{+}(x) + p_{1a}^{-}(x) = A_{1a}^{+}e^{-jk_1^{+}x} + A_{1a}^{-}e^{jk_1^{-}x} \text{ at } x \le x_l \quad (5.1)$$

$$p_{2a}(x) = p_{2a}^{+}(x) + p_{2a}^{-}(x) = A_{2a}^{+}e^{-jk_2^{+}x} + A_{2a}^{-}e^{jk_2^{-}x} \text{ at } x \ge x_r \quad (5.2)$$

$$p_{1b}(x) = p_{1b}^{+}(x) + p_{1b}^{-}(x) = A_{1b}^{+}e^{-jk_1^{+}x} + A_{1b}^{-}e^{jk_1^{-}x} \text{ at } x \le x_l \quad (5.3)$$

$$p_{2b}(x) = p_{2b}^{+}(x) + p_{2b}^{-}(x) = A_{2b}^{+}e^{-jk_2^{+}x} + A_{2b}^{-}e^{jk_2^{-}x} \text{ at } x \ge x_r \quad (5.4)$$

where the subscripts 1 and 2 denote the upstream and downstream sections, respectively, and the subscripts a and b indicated the speaker for the sound generation. The superscripts "+" and "-" denote the forward and reverse mode, respectively. Forward mode refers to condition where the sound wave propagated in the same direction as that of the air flow. Conversely, Reverse mode is the condition when the sound wave propagated in the opposite direction to the air flow. By considering the reflection and transmission of the sound wave at the edge of the sample, ($x = x_l$ and x_r), the following relations can be satisfied.

$$\begin{bmatrix} p_{1a}^{-}(x_l) & p_{2a}^{+}(x_r) \\ p_{1b}^{-}(x_l) & p_{2b}^{+}(x_r) \end{bmatrix} = \begin{bmatrix} p_{1a}^{+}(x_l) & p_{2a}^{-}(x_r) \\ p_{1b}^{+}(x_l) & p_{2b}^{-}(x_r) \end{bmatrix} \begin{bmatrix} r^{+} & t^{+} \\ t^{-} & r^{-} \end{bmatrix} \quad (5.5)$$

where $r^{\pm}$ is the amplitude ratio of the incident wave to the reflection wave, and $t^{\pm}$ is the amplitude ratio of the incident wave to the transmission wave of the (+) forward and (-) reverse modes, respectively. From Eq. (5.15), $r^{\pm}$ and $t^{\pm}$ can be expressed as follows.

$$\begin{bmatrix} r^{+} & t^{+} \\ t^{-} & r^{-} \end{bmatrix} = \begin{bmatrix} p_{1a}^{+}(x_l) & p_{2a}^{-}(x_r) \\ p_{1b}^{+}(x_l) & p_{2b}^{-}(x_r) \end{bmatrix}^{-1} \begin{bmatrix} p_{1a}^{-}(x_l) & p_{2a}^{+}(x_r) \\ p_{1b}^{-}(xx_l) & p_{2b}^{+}(x_r) \end{bmatrix} \quad (5.6)$$

The reflection, $R^{\pm}$, transmission, $T^{\pm}$, and Sound absorption coefficient, SAC, of the sample, were calculated based on Eqs. (5.17)–(5.19).

$$R^{\pm} = |r^{\pm}|^2 \quad (5.7)$$

$$T^{\pm} = |t^{\pm}|^2 \tag{5.8}$$

$$SAC^{\pm} = 1 - \left(\frac{(1\mp M)^2}{(1\pm M)^2} \cdot T^{\pm} + R^{\pm}\right) \tag{5.9}$$

where $M = U / c$. M is the averaged Mach number of the air flow, and U is the averaged flow velocity.

The normalized surface impedance of the sample was then then educed using Pridmore-Brown equation based method [6], [7]. The sound was considered to propagate in a two-dimensional channel, where the flow velocity U lies in the x-direction and is a function of y only. Thus, the pressure of the sound wave is given by

$$p = F(y)e^{j(\omega t - k_x x)} \tag{5.10}$$

where k_x is the complex wavenumber of the sound wave in the sample section (Eq. (24)) and $F(y)$ is the pressure amplitude of the sound wave as a function of y. The F(y) can be obtained by solving 2D Pridmore–Brown equation [29] given below.

$$\frac{d^2F}{dy^2} + \frac{2\kappa(dM/dy)}{1-\kappa M}\frac{dF}{dy} + k_0^2\{(1-\kappa M)^2 - \kappa^2\}F = 0 \tag{5.11}$$

where $k_o = \omega / c$ and $\kappa = k_x / k_o$. The boundary condition at the hard wall sample, which is the opposite side of the sample surface, is given by

$$\frac{dF}{dy} = 0 \text{ at } y = 0 \tag{5.12}$$

whereas the boundary condition at the sample surface is given by the Ingard–Myers's equation [30], [31].

$$\frac{dF}{dy} = -\frac{jk_0F}{z}(1-\kappa M)^2 \text{at } y = w \tag{5.13}$$

where z is the normalized surface impedance of the sample. In order to solve the Pridmore-Brown equation, the wavenumber k_x is required. The wavenumber k_x in the sample section was obtained from the calculated transmissivity $t^{\pm}$ by using equation in [7]

$$k_x^{\pm} = -\frac{arg(t^{\pm})}{l} + j\frac{(|t^{\pm}|)}{l} \tag{5.14}$$

where l is the length of the sample. Furthermore, the velocity profile, dM/dy, was varied to be uniform flow profile and shear flow profile. The velocity profile was measurement results of five resonator liners and hardwall, and is provided in Appendix.

5.3 Results and Discussion

The results and discussion will be divided into two main parts: the sound attenuation in the case of no air flow and in the case of air flow.

5.3.1 Acoustic Properties Acoustic Properties of the porous sample in FD when M = 0

A. Pressure of the sound wave inside the FD

Figure 5.4 (a) and (b) show the complex pressure amplitude, Re (P) and Im (P), of the soundwave with f = 500 Hz extracted from the microphones in the case of sintered fiber sample with ϕ = 80% generated by speaker A and speaker B, respectively. The complex pressure component were extracted to forward and reverse direction and shown in Fig. 5.4. Furthermore, the complex pressure, Re (P) and Im (P), of the soundwave with f = 500 Hz by speaker A in the complex plane is shown in Fig. 5.6. The pressure magnitude and the phase of the complex pressure of the same wave is given in Fig. 5.7. Figure 5.4, 5.5, 5.6, and 5.7 show the reduction of pressure amplitude of the sound wave inside the sample section due to the sintered fiber sample.

The pressure values at the edge of the sample section that is used for the calculation of the scattering matrix, given in equation (5.16), are marked as larger circles in Figure 5.5. By solving the scattering matrix, the reflectivity ratio, $r^{\pm}$, and the transmittivity ratio, $t^{\pm}$ can be obtained. Then, by using equation (5.17) to (5.19) the reflection coefficient, $R^{\pm}$, transmission coefficient, $T^{\pm}$, and sound absorption coefficient, $SAC^{\pm}$ can be calculated.

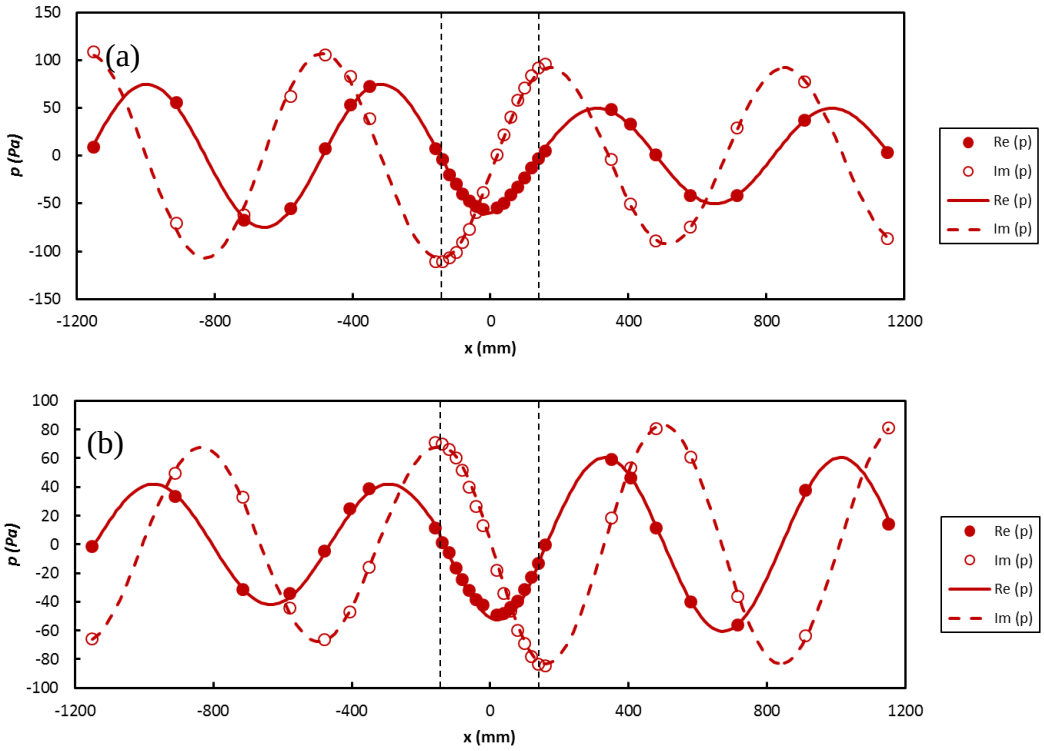

Figure 5.4 Complex pressure amplitude of the soundwave with f = 500 Hz in the case of sintered fiber sample with ϕ = 80% generated by (a) speaker A and (b) speaker B

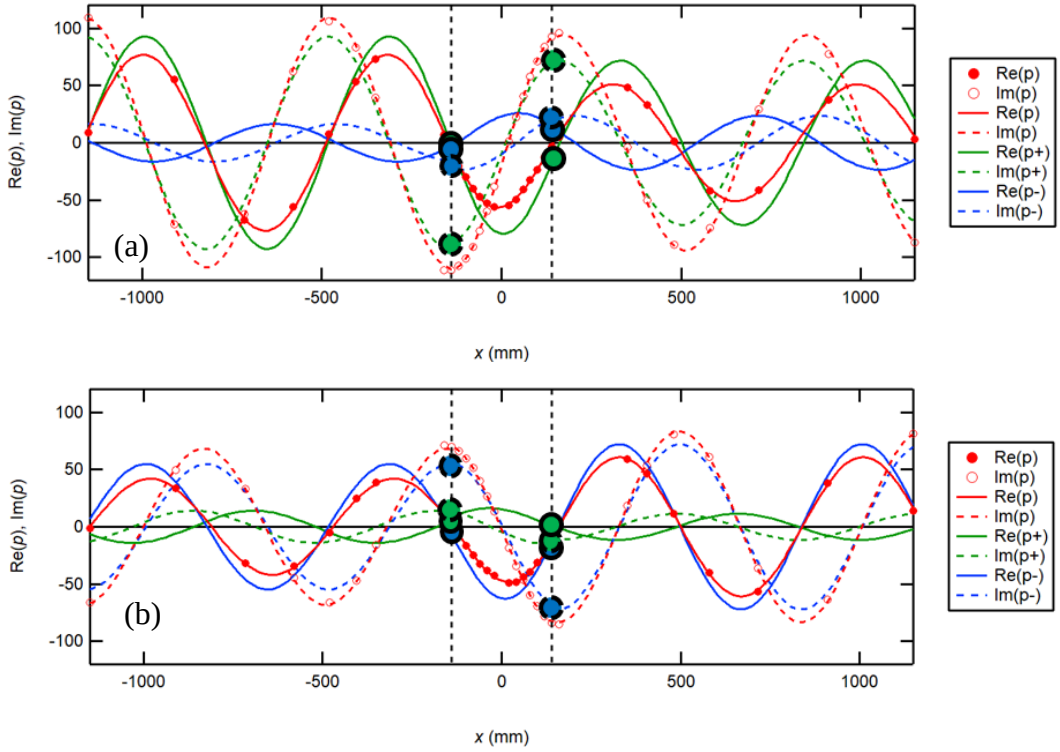

Figure 5.5 Forward and reverse complex pressure amplitude of the soundwave with f = 500 Hz in the case of sintered fiber sample with ϕ = 80% generated by (a) speaker A and (b) speaker B

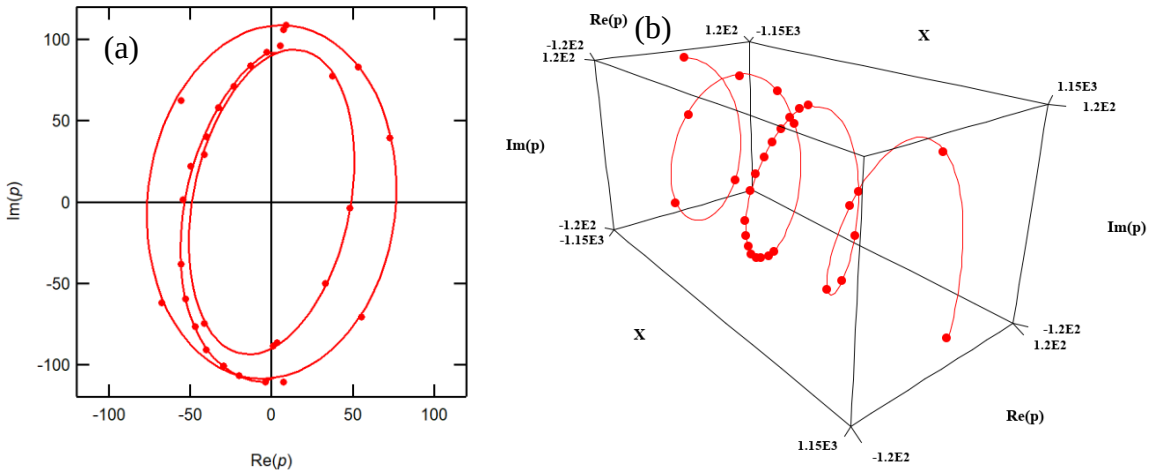

Figure 5.6 Complex pressure amplitude of the Forward soundwave with f = 500 Hz in the case of sintered fiber sample with ϕ = 80% generated by speaker A in (a) complex plane and (b) complex plane as the function of x.

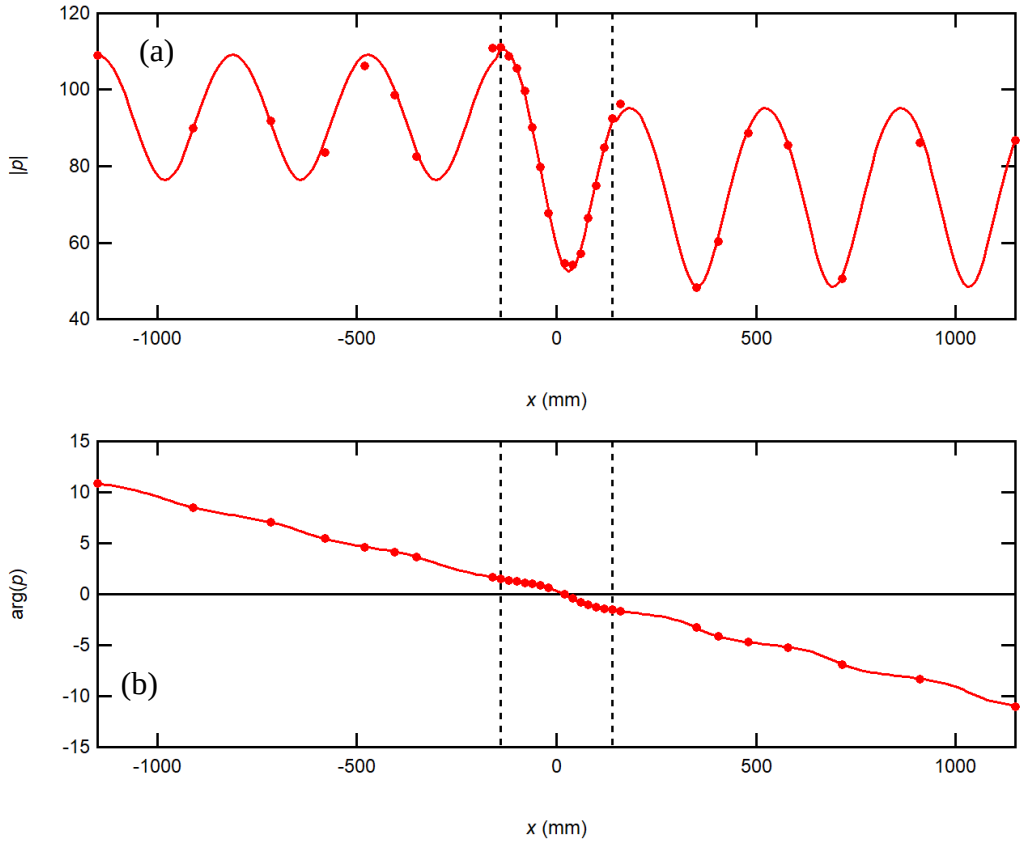

Figure 5.7 (a) Pressure magnitude and the (b) phase of the complex pressure of the soundwave with f = 500 Hz in the case of sintered fiber sample with ϕ = 80% generated by speaker A

B. Reflectance, Transmittance, and Sound Attenuation Coefficient

The reflectance in the FD setup has a different physical meaning from the reflectance in the IT. The reflectance in the FD represents the sound wave reflection at the edge of the sample section, not the reflection on the surface of the sample. This reflection is due to the mismatch between impedance in the sample section and the upstream section in the case of the forward mode (or the downstream section in the case of the reverse mode). The mismatch between the sample and the upstream or downstream section should be low, so that the reflectance measured were low especially for the sintered fiber sample as shown in Fig.5.8. In the case of foam samples, the reflection coefficient curve was fluctuating even in the absence of air flow. The peaks in the curves occurred at different frequencies for each samples. The fluctuation is the most severe for the sample with ϕ = 85%.

Furthermore, in the FD some part of the sound wave was transmitted after propagating through the sample section as shown in Fig. 5.9. Thus, in the FD setup, the difference between the total incident wave ratio and the summation of the reflection and transmission coefficient could be interpreted as the acoustic energy dissipated to the porous sample, referred as Sound Absorption Coefficient (SAC). As previously mentioned, the reflection coefficient was about zero for all the samples; thus, the sound wave propagated inside the flow duct was mainly attenuated or transmitted.

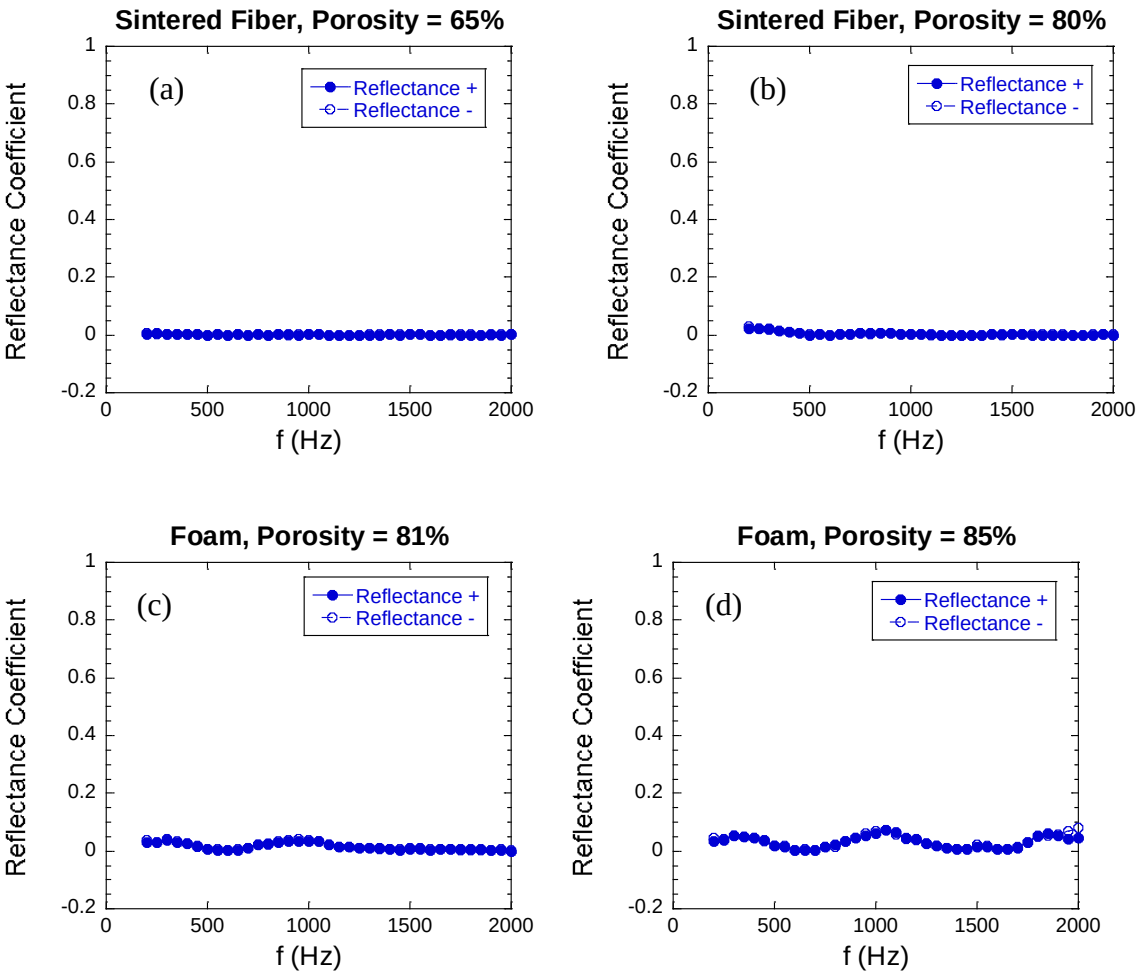

Figure 5.8. The reflection coefficient of the porous sample from flow duct experiment of the sintered fiber sample with (a) ϕ = 65% and (b) ϕ = 80% and foam sample with (c) ϕ = 81% and (d) ϕ = 85%

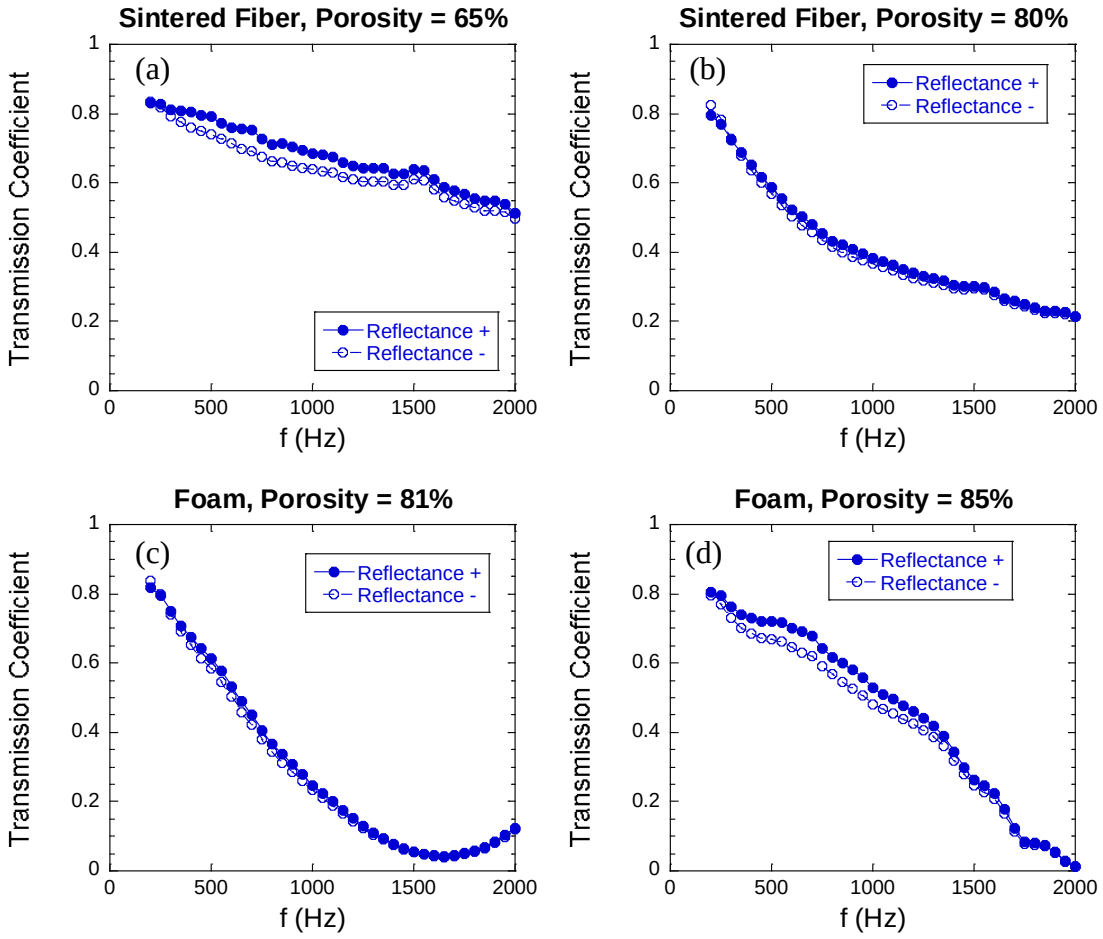

Figure 5.9. The transmission coefficient of the porous sample from flow duct experiment of the sintered fiber sample with (a) ϕ = 65% and (b) ϕ = 80% and foam sample with (c) ϕ = 81% and (d) ϕ = 85%

The SAC obtained from the FD is shown in Fig. 5.10. The SAC in forward and reverse mode of the porous sample with the same properties obtained from impedance tube experiments are provided also in Fig. 5.11. The trend of SAC curve of the sintered fiber sample and the foam sample with ϕ = 81% obtained from FD experiment is similar with the SAC curve measured in the IT. For the sintered fiber samples, the SAC increased logarithmically along the frequency. In the case of the foam sample with ϕ = 81%, the SAC in the FD also has a peak at 1600 Hz, slightly at lower frequency than the peak in the IT. The foam sample with ϕ = 85% shows the most different results. In the FD the SAC was improved a lot. The SAC curve increase was steeper and the overall SAC was

higher than in the IT. However, it is difficult to compare directly the SAC in the FD and SAC in the IT because the SAC is extrinsic parameter that is related to the size of the sample. The samples for the IT experiments are much smaller than those for the FD experiments. Thus the similarity of the SAC in the FD and IT for the sintered fiber sample and the foam sample with ϕ = 81% might be accidental.

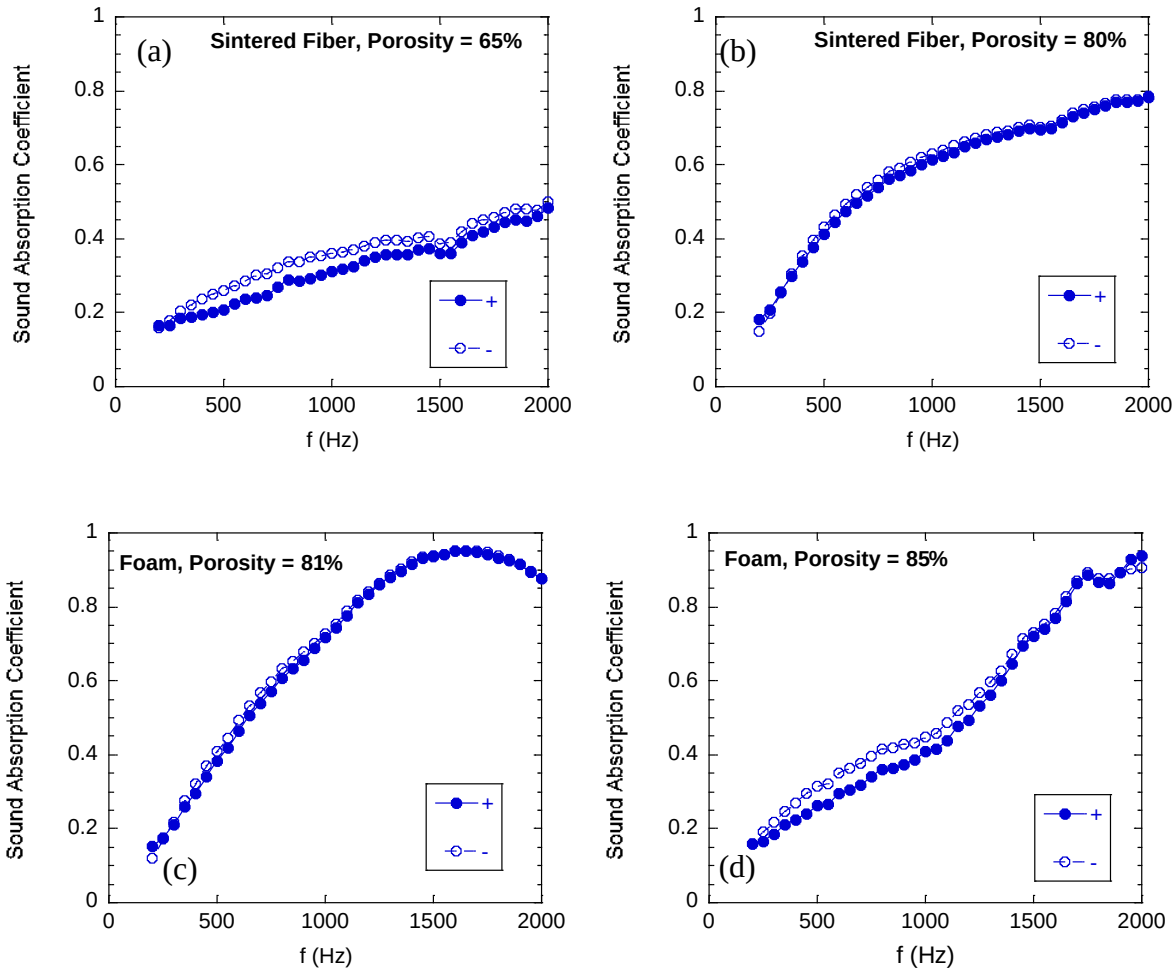

Figure 5.10. The sound absorption coefficient as a function of frequency, *f*, for the (a) sintered fiber sample with ϕ = 65%, (b) sintered fiber sample with ϕ = 80%, (c) foam sample with ϕ = 81%, and (d) foam sample with ϕ = 85%, obtained from the flow duct experiments.

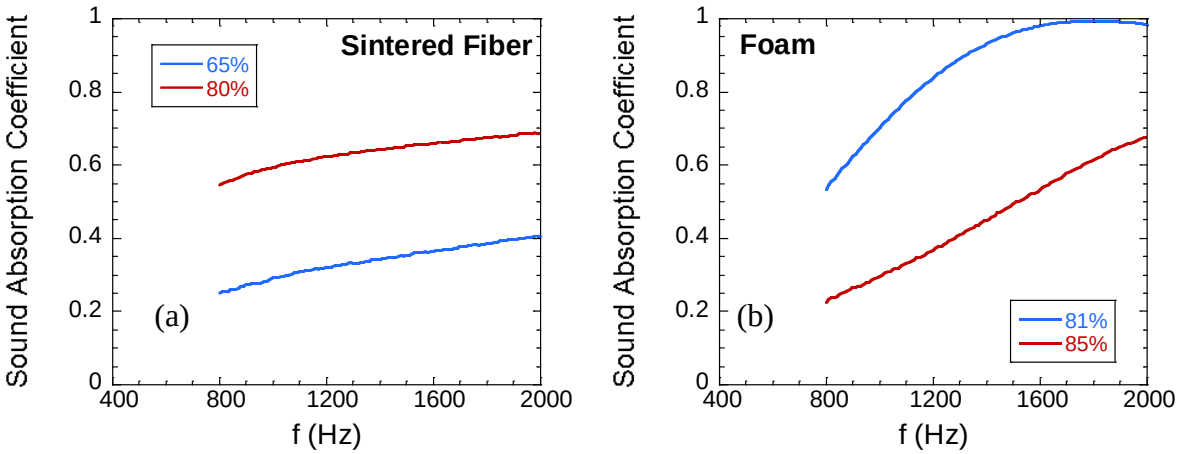

Figure 5.11. The sound absorption coefficient as a function of frequency, *f*, obtained from the impedance tube for the (a) sintered fiber sample with ϕ = 65%, and ϕ = 80%, and (b) foam sample with ϕ = 81%, and ϕ = 85%.

It should be noted that the flow duct system should be symmetric in x axis. Thus, in the case of no air flow, the *R*, *T*, and SAC in the forward and reverse mode should be the same. However, for the sintered fiber sample with ϕ = 65% and the foam sample with ϕ = 85%, the *T* and SAC in forward mode differed from the reverse mode. These samples might be less uniform than the other two samples.

C. Impedance

The surface impedance indicates the ratio between the acoustic pressure and acoustic velocity on the surface of the porous sample. In this research the surface impedance of the sample was educed using Pridmore - Brown equation based method. The Pridmore - Brown based impedance eduction method was usually used for locally reactive acoustic liner such as in the case of resonator type liner. Thus, that the impedance is uniform along the sample surface. The porous sample, on the other hand, might act as locally reactive or non-locally reactive depends on its structure. Thus, the actual impedance especially of some of porous material might be varied along the surface. However, in this research we use the Pridmore Brown equation to all of the samples. The educed impedance in the FD

when $M = 0$ was compared to the impedance measured in the IT. For the locally reactive liner, the impedance in the FD with no air flow and IT should be the same.

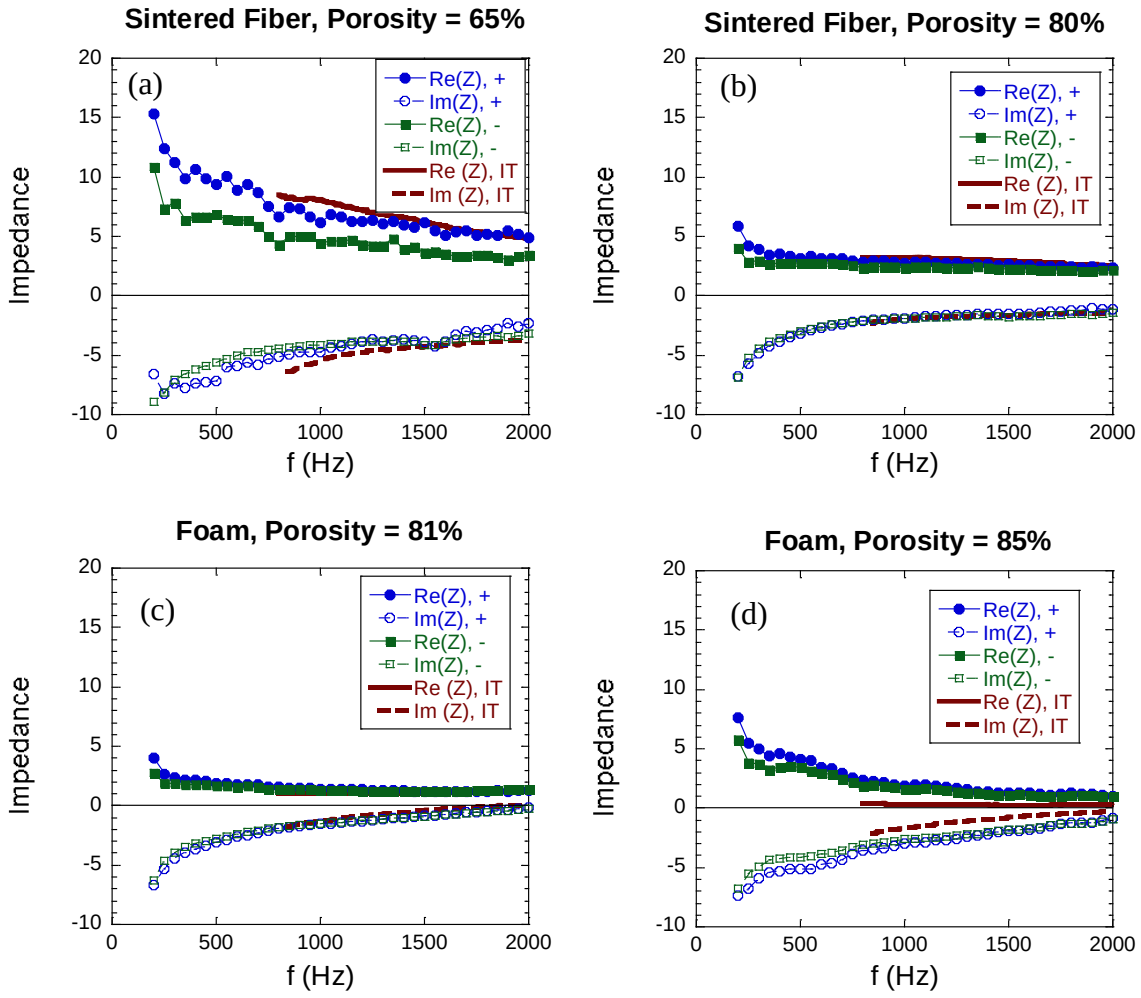

Figure 5.12. The surface impedance as a function of frequency, f, for the (a) sintered fiber sample with ϕ = 65%, (b) sintered fiber sample with ϕ = 80%, (c) foam sample with ϕ = 81%, and (d) foam sample with ϕ = 85%, obtained from the flow duct experiments. The corresponding results obtained from the IT experiments are also plotted.

Figure 5.12 shows the surface impedance of the porous sample in the case of $M = 0$. The impedance of the corresponding porous sample in the IT within the frequency range is also provided. In the case of the sintered fiber sample and the foam sample with ϕ = 81%, the impedance in the FD has a similar trend with that in the IT. On the other hand, the IT and FD impedance is different for the foam sample with ϕ = 85%. The |Re(z)| and |Im(z)| values obtained from the FD experiments at $M = 0$ are larger than those obtained from the IT experiments. Due to the low flow resistivity of this sample, in the FD the sound wave might propagate in x and y direction in the FD. In the IT the sound wave could penetrated far into the sample, but was reflected by the hard wall so that the resistance is close to zero whereas and the reactance is smaller than the corresponding values elicited in the FD experiments.

D. Surface wave and locally reactivity

The difference between the SAC and impedance of the foam sample in the IT and FD with $M = 0$ should be caused by the difference in direction of the sound wave to the sample surface. Figure 5.13 shows the normalized complex axial wavenumber of the sound wave in the sample section, $\kappa = k_x/k$, as a function of frequency, f, for the porous samples. The Re(kx/k) represents the physical wave number inside the sample section whereas the Im(kx/k) represents the change of the pressure amplitude of the sound wave. For the most of the samples, Re(kx/k) > 1 and Im(kx/k) < 0 in most part of the entire frequency range. In the case of the foam sample with ϕ = 81%, however, the Re(κ) < 1 at f > 1700 Hz.

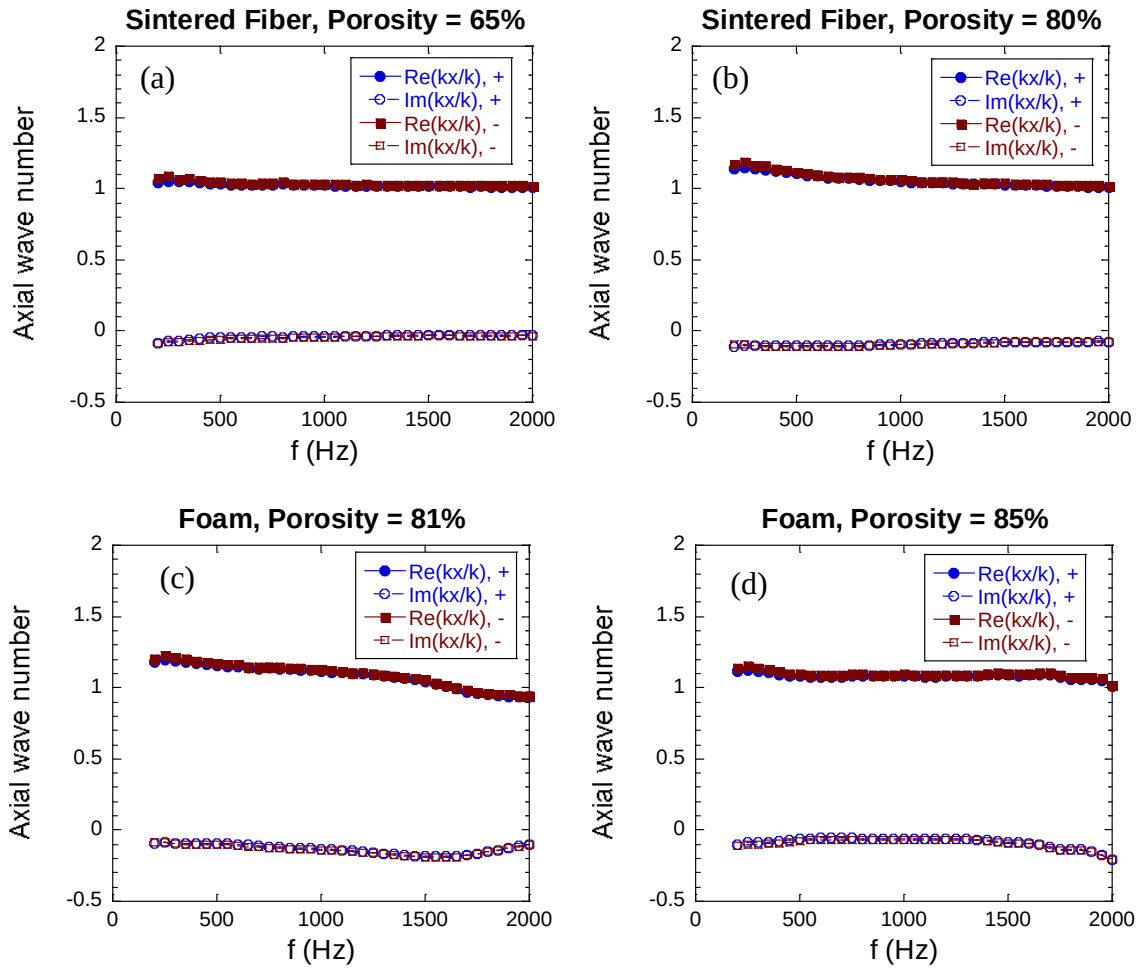

Figure 5.13. Axial wave number of the porous sample from flow of the sintered fiber sample with (a) ϕ = 65% and (b) ϕ = 80% and foam sample with (c) ϕ = 81% and (d) ϕ = 85%

The negative value of the imaginary wave number indicates that the pressure amplitude of the sound wave decreased along the sample section. It could be seen from the raw pressure data obtained in the sample section in Fig. 5.5. At M = 0, the Re(κ) is larger than 1, meaning that more waves in the sample section than in the upstream and downstream. The k and kx should follow the dispersion relation

$$k^2 = k_x^2 + k_y^2 \tag{5.24}$$

As Re(kx/k) > 1 and Im(kx/k) < 0, there should be sound wave propagate in y direction in order to satisfy the dispersion relation. On the other hand, the cut-off frequency of the (m,

n) mode in the sound wave propagation in the *y* and *z* directions (in the width and height directions of the rectangular duct) is given by [31]

$$f_{m,n} = \frac{c}{2}\sqrt{\left(\frac{m}{w}\right)^2 + \left(\frac{n}{h}\right)^2} \qquad (5.25)$$

The shape of the cross-section of the duct has a rectangular shape with a width (*w*) of 80 mm and a height (*h*) of 60 mm, that correspond to the cut-off frequency of (1, 0) and (0,1) modes at c = 340 m s^{-1} is $f_{1,0} = 2833$ Hz and $f_{0,1} = 2125$ Hz. The frequency range of the data from the FD is 250 Hz to 2000 Hz, which is below the cutoff frequency. Thus, the sound wave inside the duct should be propagating in x direction whereas no sound wave propagated in other directions. Considering this fact, there should be sound wave propagated in y direction but only near the surface of the samples. This wave could be referred as a surface wave that acts in similar manner with an evanescent wave.

The above discussion is based on the assumption that the porous metal sample can be regarded as a locally reactive surface such as Helmholtz resonator type acoustic liners. In the case of resonator, the local reactivity indicated that the sound wave was attenuated by each of resonator cells and each cells doesn't affect the neighboring cells. For them literature, porous materials generally could act as either locally reactive or non-locally reactive [23]–[25]. Brandao et al. [23] reported that a porous material of which flow resistivity is higher than 30,000 Pa s m^{-2} acts as local reactivity surface if the distance from the sound source is greater than or equal to 0.3 m, i.e. the sound wave can be considered as a plane wave. The flow resistivity of two foam samples used in this study is lower than 30,000 Pa s m^{-2}, while that of two sintered fiber samples is higher than 100,000 Pa s m^{-2}. According to the report by Brandao et al. [23], the sintered fiber sample can be regarded as a locally reactive surface, but the foam sample can be regarded as a

non-locally reactive surface. However, the current results indicated that the foam sample with ϕ = 81%might also acted in similar way to locally reactive liner. By contrast, for the foam sample with ϕ = 85%, it should be inherently difficult to obtain the surface impedance even at M = 0. The low flow resistivity of this sample might enable the sound wave to be attenuated in normal and parallel direction of the sample surface. In contrast, in the other samples, the high flow resistivity limited the sound wave to propagate only in normal direction.

5.3.2 Effects of Air Flow on the Sound Wave Attenuation inside the Flow Duct

A. Sound Attenuation Coefficient

Figure 5.14 shows the effect of air speed on the SAC of the porous sample. Generally, the increase of air speed shifted the SAC curve to a higher frequency in the forward mode. In contrast, the air flow shifted the SAC curve to a lower frequency in the reverse mode. The simple explanation is that the air flow changes the effective sound speed so that the frequency of the sound wave shifted. In the forward more, the air flow increased the effective air speed whereas the in the reverse mode, it reduced the air speed. This phenomenon shows the interaction between the air flow and the sound wave only, without considering the effect of the sample structure.

The foam samples however indicated more complicated phenomena than the sintered fiber samples. Unlike the other samples, in the case of the foam sample with ϕ = 85%, the effect of the air speed on the SAC in forward mode is insignificant. Furthermore, in the reverse mode, the increase of air speed reduces the SAC in high frequency. In the case of the foam sample with ϕ = 81%, the increase of air speed in the forward mode did not change the SAC. Thus, the SAC results for the foam samples in high frequency indicate another effect in addition the interaction between the air flow and sound wave.

It is also important to note that previously Tam and Enomoto, mentioned that interaction between air flow and the acoustic liner structure might generate sound. Thus, there is also possibility that the attenuation of the sound wave inside the sample section of the FD might be accompanied by sound wave generation too. However, in this report, the sound generation inside the sample is not considered..

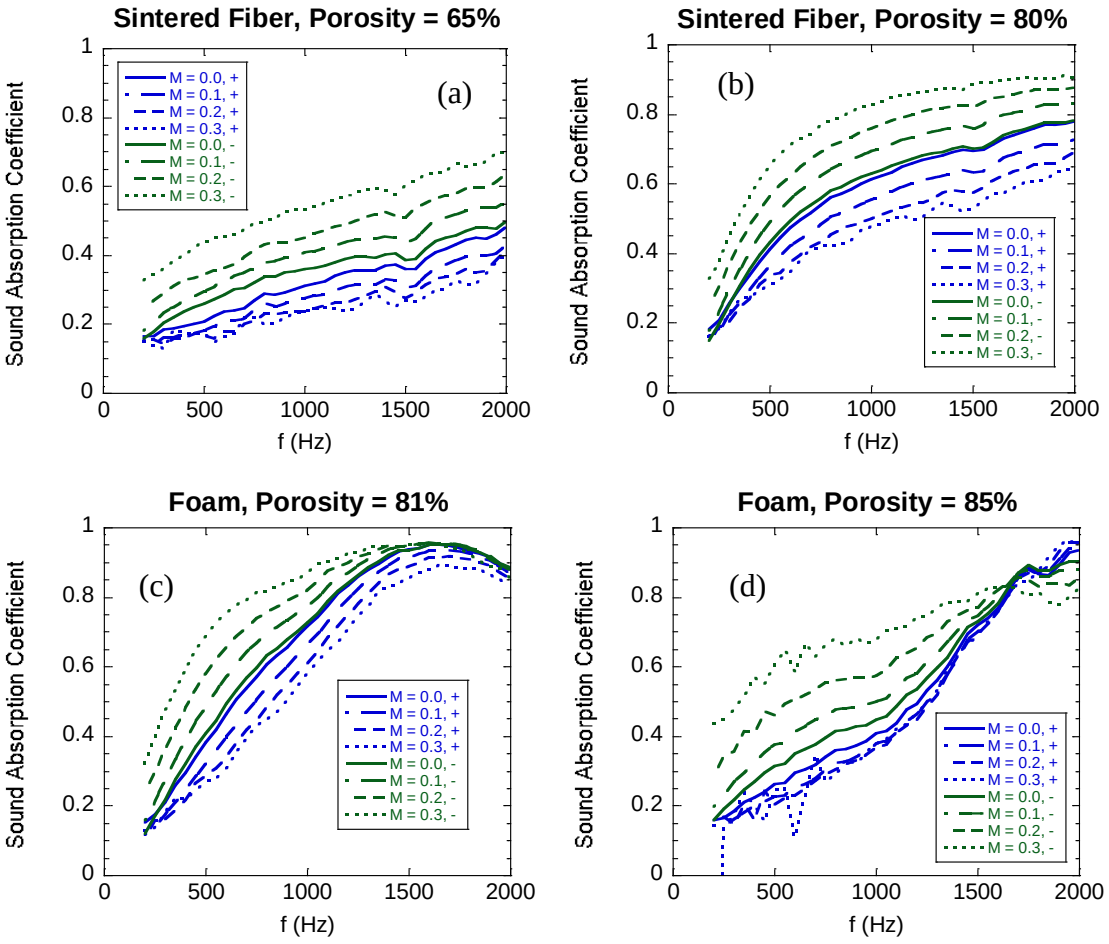

Figure 5.14. The effect of air speed on the sound absorption coefficient in the forward and reverse modes, as a function of frequency, *f*, for the (a) sintered fiber sample with ϕ = 65%, (b) sintered fiber sample with ϕ = 80%, (c) foam sample with ϕ = 81%, and (d) foam sample with ϕ = 85%, obtained from the flow duct experiments.

B. Axial wave number

Figure 5.15 and 5.26 show the effect of air speed on the axial wave number inside the sample section for the sintered fiber samples and the foam samples in forward and reverse mode, respectively. The effect of the air speed on the Re (*kx/k*) are the same for every sample. In the forward mode, the increase of air speed cause Re *(kx/k)* to decrease. Thus, the wave number was reduced as the air speed increase that might cause lower attenuation by the sample. On the other hand, in the reverse mode, the increase of the air speed causes the Re (kx/k) to increase. Thus, when the air speed increased in the reverse mode, there were more waves inside the sample section that might cause more attenuation by the sample. The Re(kx/k) represents the number of sound wave per unit length inside the sample section. Thus, the change of the wave number, Re(kx/k), inside the sample section might be related only to the interaction between the air speed on the effective sound speed. Furthermore, it is also shown that the shift of the Re *(kx/k)* curve due to the change of the air speed is the same for all the samples in each modes.

The effect of air speed on the Im(kx/k) was shown to be different for the samples and cannot be interpreted so simply. In the forward mode, the air speed does not affect the Im(kx/k) significantly. On the other hand, in the reverse mode, the increase of air speed caused the Im(kx/k) curve become lower. Thus, the attenuation was improved as the air speed increased. However, this improvement was varied for every sample. In the case of foam sample with ϕ = 81%, at low frequency, the increase of air speed reduced the Im(kx/k). However, when M = 0.3, the Im(kx/k) become flatter indicating that there might be an opposite effect growing as the frequency increase. When f > 1600 Hz, this effect canceld the reduction of Im(kx/k) due to air speed so that the Im(kx/k) curve become independent of the air speed. This agrees well with the corresponding SAC of

this sample that at high frequency, the SAC become independent of the air speed in reverse mode.

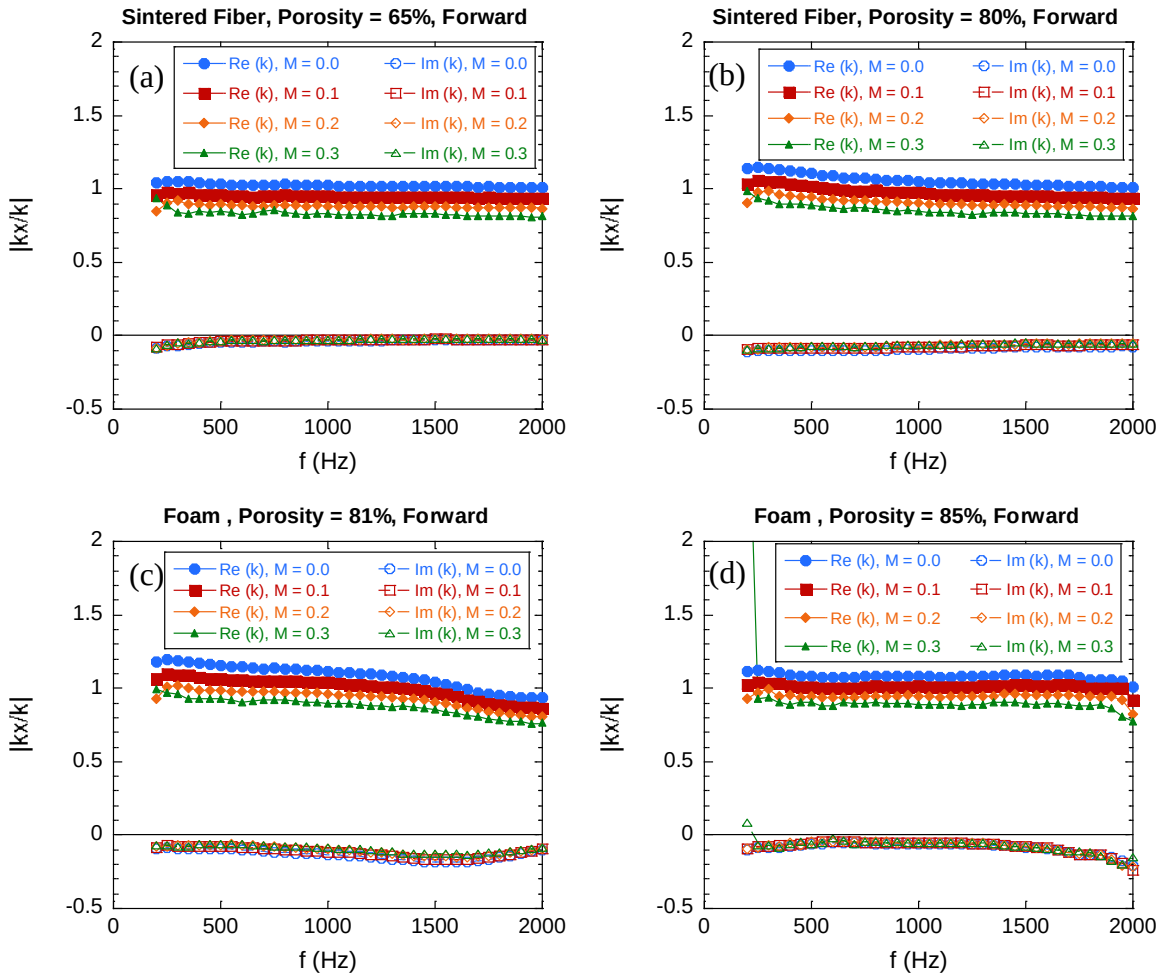

Figure 5.15. The effect of air speed on axial wave as a function of frequency, *f*, for the of sintered fiber sample with (a) ϕ = 65% and (b) ϕ = 80% and the foam sample with (c) ϕ = 81% and (d) ϕ=85% in the forward mode

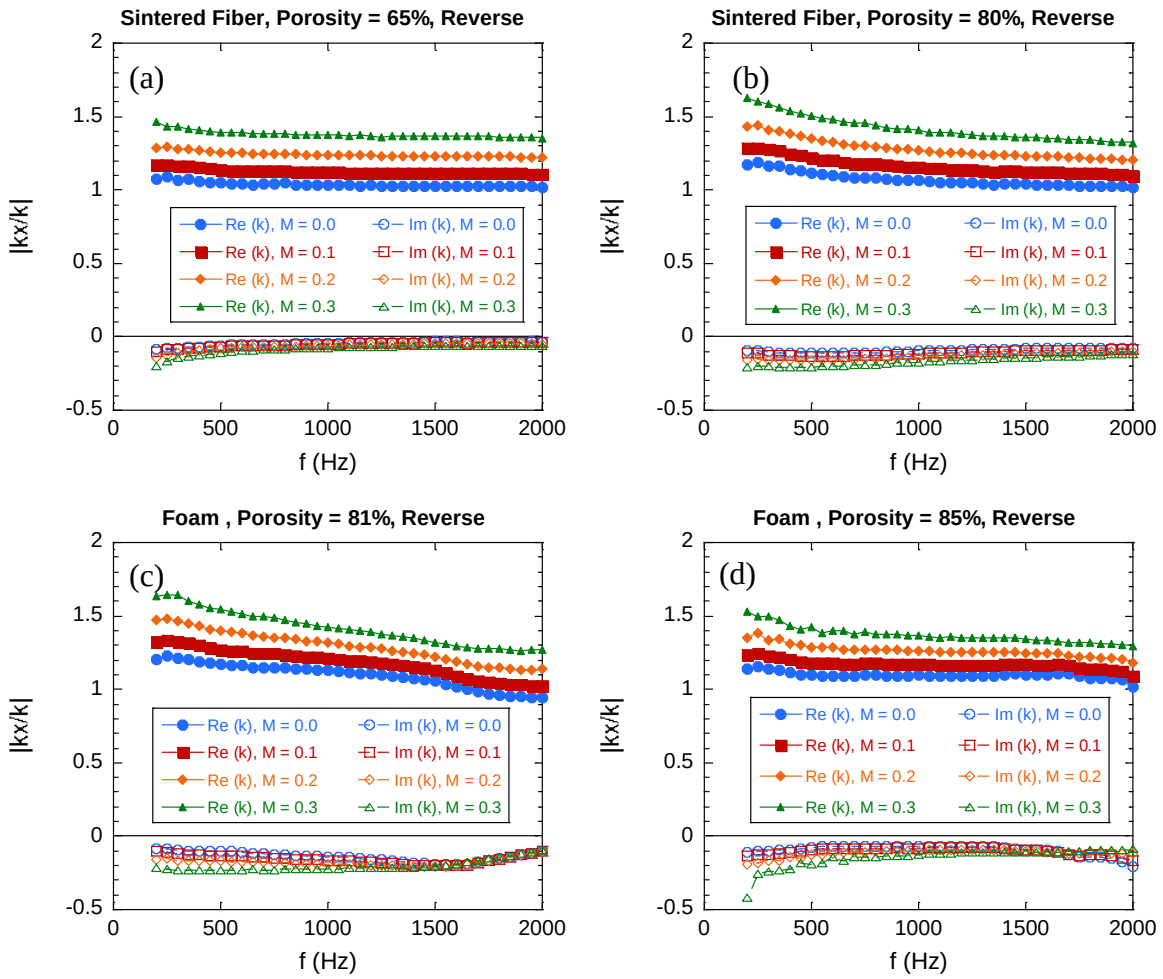

Figure 5.16. The effect of air speed on axial wave as a function of frequency, *f*, for the of sintered fiber sample with (a) ϕ = 65% and (b) ϕ = 80% and the foam sample with (c) ϕ = 81% and (d) ϕ=85% in the reverse mode

For the foam sample with ϕ = 85%, when f > 1600 Hz, the effect of air speed on the Im(kx/k) became the opposite. At high frequency, the increase of air speed causes the Im(kx/k) curve to increase. Thus, the attenuation become lower as the air speed increased as indicated by the SAC in figure 5.18. The Im(kx/k) might be related not only the interaction between the air flow and sound wave, but also the sample structure. The structure of the sample might affect the boundary layer in the surface of the sample and affect the attenuation.

C. Impedance

The SAC results show that at low frequency, the air flow effect might be due to interaction between the air flow and sound speed. However, the results at higher frequency, especially in the case of foam samples, indicate the significance of other effects that might include other effect, for example the boundary layer. The boundary layer might relate the air flow and porous structure. Furthermore, the boundary layer might interact with the sound wave and affect the sound attenuation by the porous sample. The effect of air speed on the attenuation coefficient, Im(kx/k), also might not only be related to the interaction between the air flow and sound wave, but also the boundary layer. Both the SAC and axial wave number, *kx*, were obtained from the scattering matrix that does not include the boundary layer on the calculation but the effect of boundary layer might still be observed. On the other hand, in the impedance eduction process, in the other hand, the boundary layer effect could be considered by changing the velocity profile.

Figure 5.17, 5.18, 5.19 and 5.20 show the impedance of the samples educed using non uniform velocity profile and shear velocity profile for solving the Pridmore Brown equation. When the uniform velocity profile was assumed as uniform, $dM/dy = 0$ in the impedance eduction process, the boundary layer is neglected. Thus the impedance might only consider that the air flow affects only the sound speed and the interplay between the air flow and the sound wave whereas the flow boundary layer is not considered. On the other hand, when shear the uniform velocity profile was assumed as uniform, $dM/dy \neq 0$, the boundary layer inside the duct was considered. The velocity profile was the average of flow profile measurement in the case of hardwall and five types of resonator liners, and is provided in appendix 5.2. The velocity profile might not be accurate for the porous sample, but it might show the effect of the boundary layer for the impedance eduction

process. The impedance obtained using the uniform and non-uniform velocity profile could be compared to observe the effect of the boundary layer.

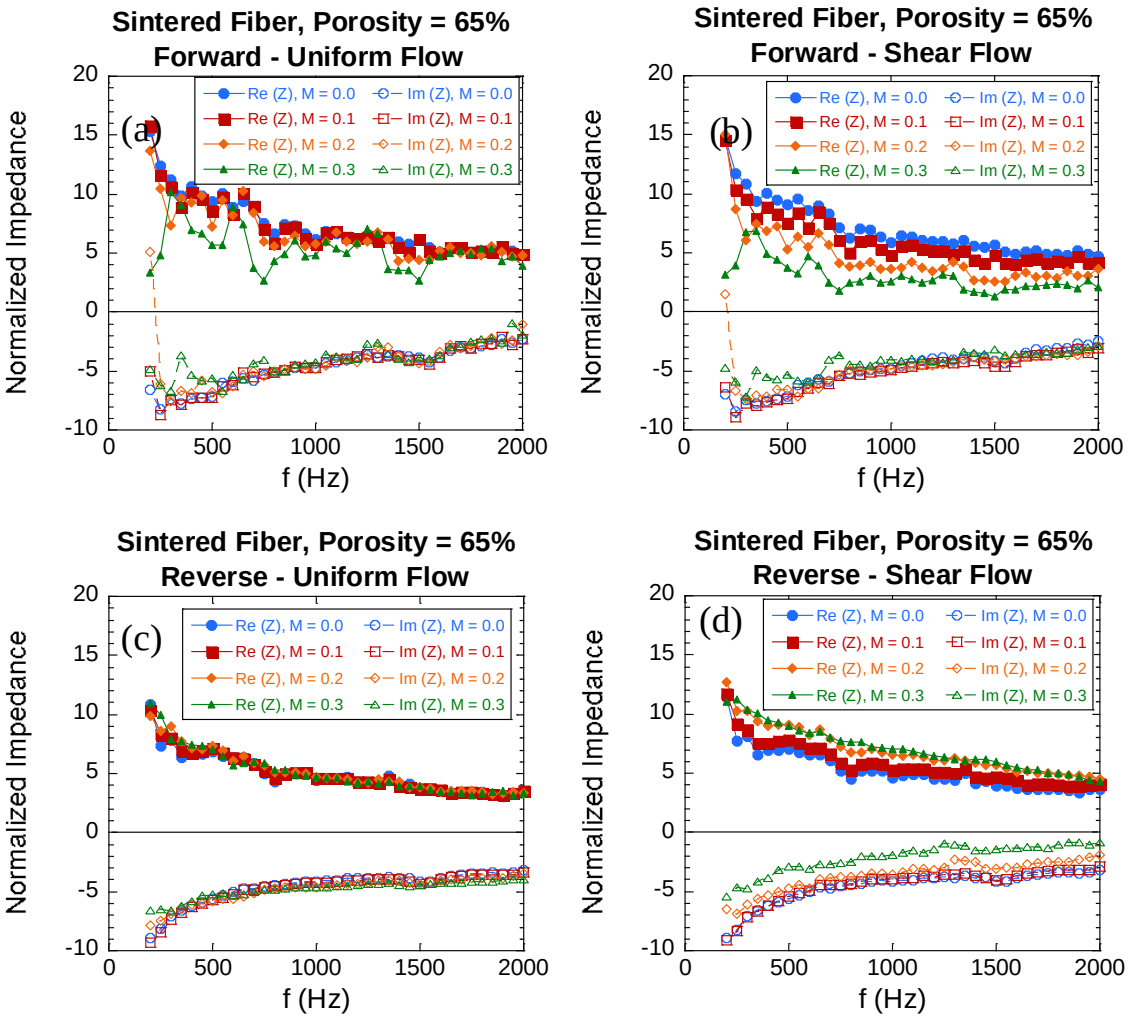

Figure 5.17. The impedance, Re(z) and Im(z), as a function of frequency, f, for the sintered fiber sample with ϕ = 65% in forward mode educed using (a) uniform flow profile and (b) shear flow profile and reverse mode educed using (c) uniform flow profile and (d) shear flow profile

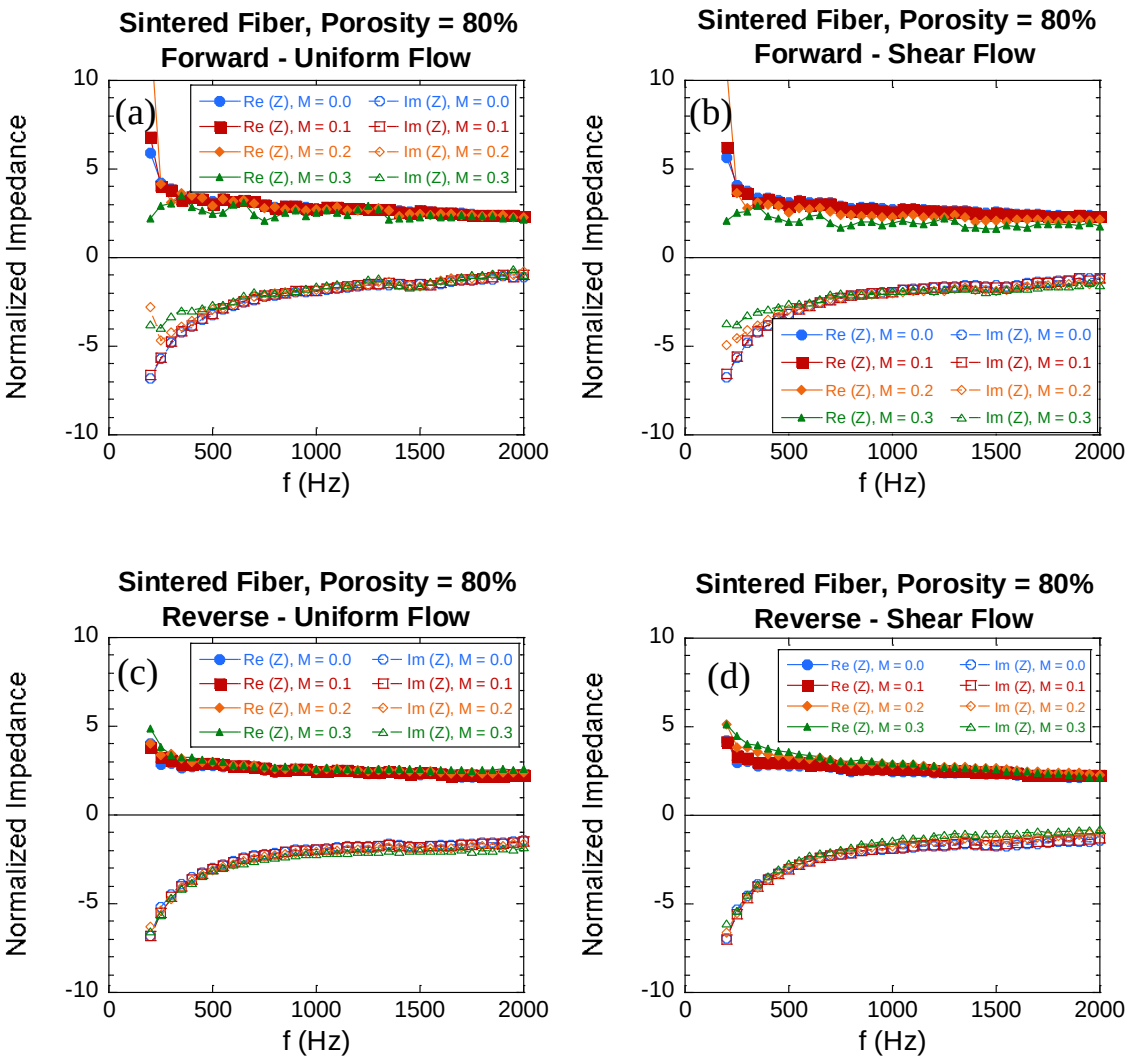

Figure 5.18. The impedance, Re(z) and Im(z), as a function of frequency, f, for the sintered fiber sample with ϕ = 80% in forward mode educed using (a) uniform flow profile and (b) shear flow profile and reverse mode educed using (c) uniform flow profile and (d) shear flow profile

From figure 5.17, 5.18, 5.19 and 5.20, it is shown that in some samples the effect of the velocity profile is significant on the impedance eduction process. The impedance obtained using the uniform and non-uniform velocity profile was different significantly for the sintered fiber sample with ϕ = 65% and the foam sample with ϕ = 85%. On contrary, for the other samples, sintered fiber sample with ϕ = 80% and the foam sample with ϕ = 81%, the velocity profile does not significantly affect the impedance results.

Figure 5.17, 5.18, 5.19 and 5.20 also show that, in the forward mode, the |Re(z)| and |Im(z)| decrease with increasing M. The effect of flow conditions on the impedance is larger when the non-uniform velocity profiles were used. In the reverse mode, both velocity profiles resulted to the resistance Re(z) increasing with increasing M.

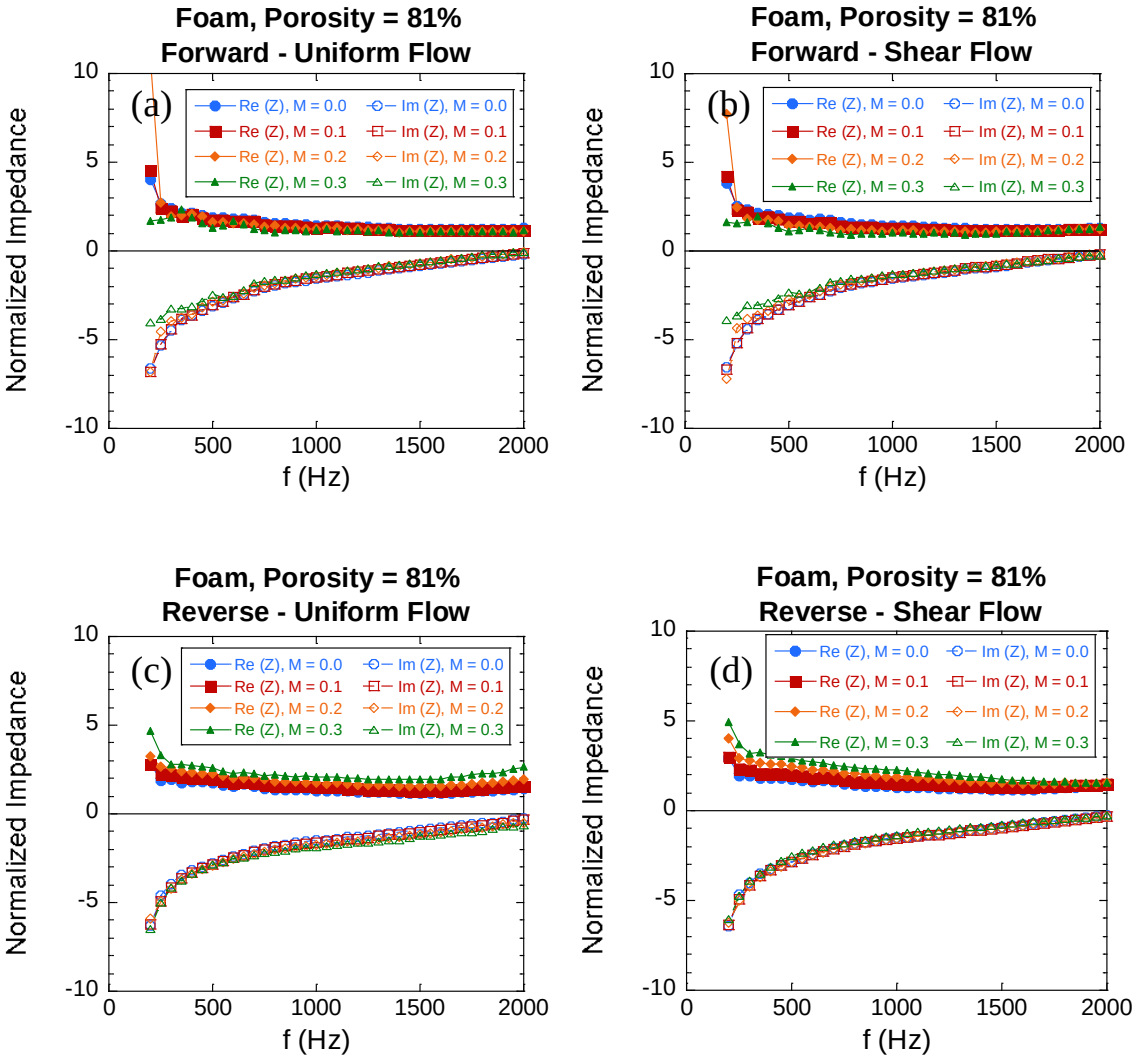

Figure 5.19. The impedance, Re(z) and Im(z), as a function of frequency, f, for the foam sample with ϕ = 81% in forward mode educed using (a) uniform flow profile and (b) shear flow profile and reverse mode educed using (c) uniform flow profile and (d) shear flow profile

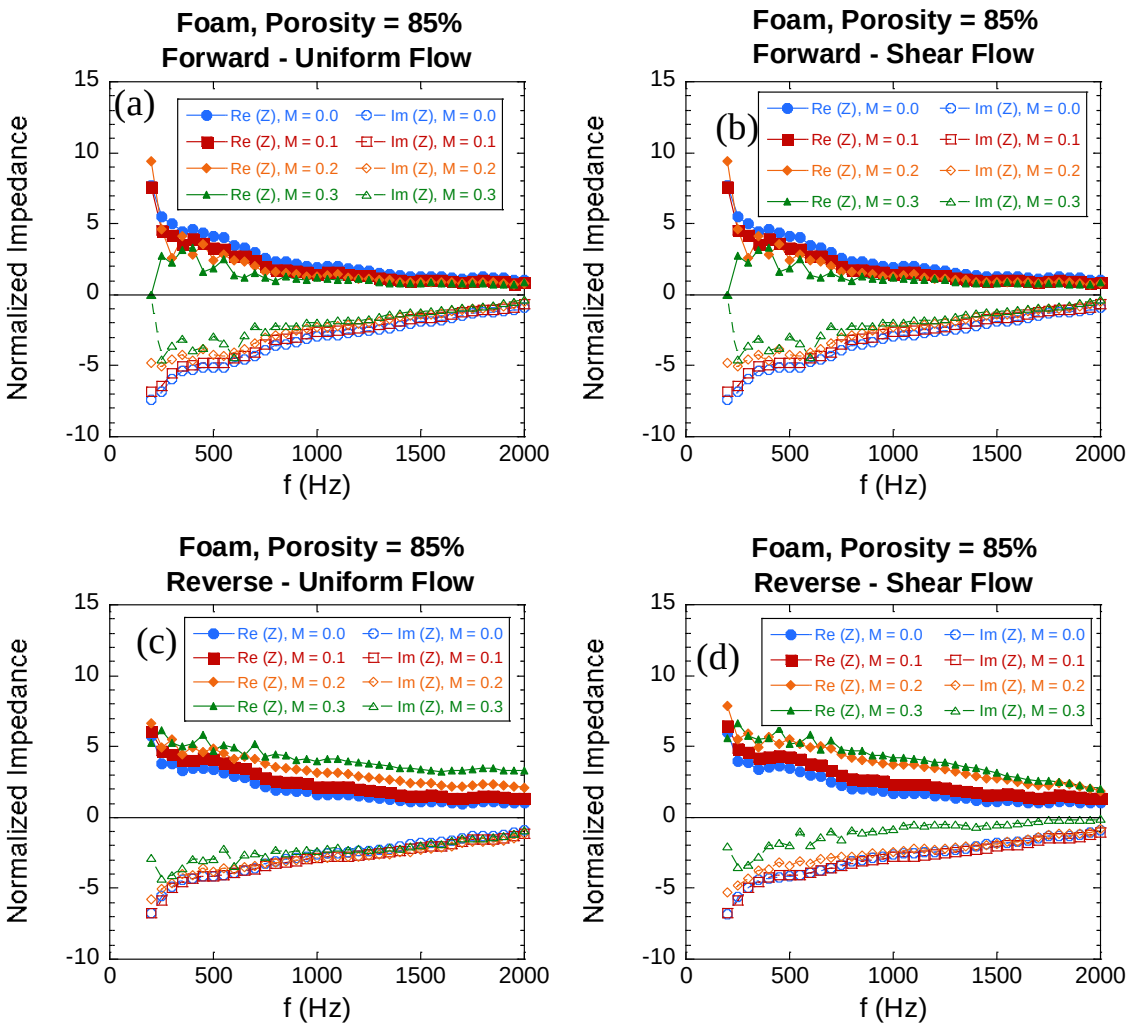

Figure 5.20. The impedance, Re(z) and Im(z), as a function of frequency, f, for the foam sample with ϕ = 85% in forward mode educed using (a) uniform flow profile and (b) shear flow profile and reverse mode educed using (c) uniform flow profile and (d) shear flow profile

The Pridmore–Brown equation (Eq. 5.21) could be regarded as the mass-spring-damper model as follows.

$$\ddot{x} + \frac{b}{m}\dot{x} + \frac{s}{m}x = 0 \tag{5.26}$$

$$\frac{b}{m} = \frac{2\kappa(dM/dy)}{1-\kappa M} \tag{5.27}$$

$$\frac{s}{m} = k_0^2\{(1-\kappa M)^2 - \kappa^2\} \tag{5.19}$$

where m, b, and s denote the mass, damper, and spring constant, respectively. It should be noted though that Pridmore–Brown equation considers pressure as a function of space, *y*, whereas the mass spring samper system considers space as a function of time, *t*. Thus the direct comparison of the two might not be correct, but the pressure distribution along *y* axis inside the samples section in the Pridmore – Brown equation might be understood more easily using this analogy.

If we consider the shear velocity profiles, we can capture the energy absorption in the flow boundary layer that represented in the damping factor appropriately. In contrast, when the uniform velocity profiles were assumed, the second term in the left hand of equation (5.21) and (5.26) that contains the damping constant becomes zero. This might explain the case of the sintered fiber sample with ϕ = 65%, in reverse mode. By using non-uniform velocity profiles, the reactance approaches zero (Im(z) $\rightarrow$ 0) with the increase of *M*, whereas the reactance does not change significantly when uniform velocity profile was used. The reactance approaches zero phenomenon might be represented by the damping constant. This can be interpreted as the flow boundary layer might absorb the sound wave energy due to damping effect.

In the case of uniform flow profile, however, the increase of air speed was still shown to affect the impedance. The damping constant in the Pridmore - Brown equation was zero due to the uniform flow assumption. Meanwhile the third term in the left hand side expresses the undamped natural frequency related to the spring constant was not zero. Thus, in this case, the change of impedance depends on the spring constant only. Equation (5.19) indicates that the spring constant does not depend on the velocity profiles, but depends on *M* and wave number that is also a function of *M*. However, in order to clearly understand the effect of the air speed on the sound attenuation mechanism further

investigation should be conducted. Furthermore, the sound attenuation mechanism inside the boundary layer and also inside the sample is still to be solved.

5.4 Conclusion

The surface impedance of the sintered fiber and the foam samples with ϕ = 81% inside the IT and FD has an identical trend which is similar to the case of locally reactive resonator liner. In contrast, the surface impedance in the IT and FD is different for the foam samples with ϕ = 85%, which have lower flow resistivity. The porous material might be acted similarly to the locally reactive liner if the flow resistivity is high. For these samples, the impedance inside the FD might be predicted more easily using the IT impedance results. In the case of the porous samples with low flow resistivity, the samples might act as a non-locally reactive liner. Thus, its impedance in the FD might be difficult to be predicted using the IT result, but the attenuation in the FD might be improved. However, the SAC of the samples in the IT and FD cannot be compared directly as it depend on the size of the sample.

The increase of air speed shifted the SAC curve to a higher frequency in the forward mode and to a lower frequency in the reverse mode. This is because the interaction between the air flow and the sound speed changes the effective sound wave. However, in the case of the foam sample, other phenomenon might occur at high frequency. The change of the effective sound speed also affected the real part of the wave number, Re (kx/k). In the forward mode, the increase of air speed reduces the Re (kx/k) whereas it increase the Re (kx/k) in the reverse mode for all of the samples. However, the effect of the air speed on the Im (kx/k) cannot be interpreted so easily.

By varying the velocity profiles for the impedance eduction process, uniform velocity profile and shear velocity profile, the effect of boundary layer might be considered. The velocity profile affect the impedance of some of the samples, the sintered fiber sample with ϕ

= 65% and the foam sample with ϕ = 85%, but not the other two samples. Furthermore, the pressure distribution along *y* axis inside the sample section could be interpreted by using the mass-damper-spring system. By using shear velocity profile, the damping constant might cause the reactance approaches zero with increasing *M* indicating that the flow boundary layer absorbs the sound energy because. Furthermore, when uniform velocity profile assumption was used, the damping constant becomes zero, and the spring constant becomes significant to affect the impedance of the samples. Meanwhile the spring constant depends on the air speed. However, the sound attenuation mechanism inside the boundary layer and also inside the sample is still to be solved.

5.5 References

[1] P. Nordin, S. L. Sarin, E. R. Rademaker, and S. Aerosystems, "Development of New Liner Technology for Application in Hot Stream Areas of Aero-Engines," pp. 1–13, 2004.

[2] D. L. Sutliff and M. G. Jones, "Low-Speed Fan Noise Attenuation from a Foam-Metal Liner," *J. Aircr.*, vol. 46, no. 4, pp. 1381–1394, 2009.

[3] D. L. Sutliff, M. G. Jones, and T. C. Hartley, "High-Speed Turbofan Noise Reduction Using Foam-Metal Liner Over-the-Rotor," *J. Aircr.*, vol. 50, no. 5, pp. 1491–1503, 2013.

[4] K. Knobloch, L. Enghardt, and F. Bake, "APU-Noise Reduction by Novel Muffler Concepts," in *Proceedings of ASME Turbo Expo 2018*, 2018, pp. 1–11.

[5] C. Heuwinkel, L. Enghardt, and I. Röhle, "Experimental Investigation of the Acoustic Damping of Perforated Liners with Bias Flow," *13th AIAA/CEAS Aeroacoustics Conf. (28th AIAA Aeroacoustics Conf.*, 2007.

[6] M. G. Jones, W. R. Watson, B. M. Howerton, and S. Busse-Gerstengarbe, "Comparative Study of Impedance Eduction Methods, Part 2: NASA Tests and Methodology," in *19th AIAA/CEAS Aeroacoust. Conf*, 2013, p. AIAA-2013-2125.

[7] S. Busse-Gerstengarbe, F. Bake, L. Enghardt, and M. G. Jones, "Comparative Study of Impedance Eduction Methods, Part 1: DLR Tests and Methodology," in *19th AIAA/CEAS Aeroacoust. Conf*, 2013, p. AIAA-2013-2125.

[8] T. Harada, "ダクト内共鳴型吸音パネルの 音響特性の予測に関する研究," The University of Tokyo, 2018.

[9] F. Bake, R. Burgmayer, A. Schulz, and L. Enghardt, "IFAR Liner Benchmark - Challenge #1 - DLR," in *25th AIAA/CEAS Aeroacoustics Conference*, 2019, p. AIAA-2019-2601.

[10] T. Ishii, K. Nagai, H. Oinuma, and S. Enomoto, "Experimental Study of Acoustic Liner Panels Shared in IFAR Program," in *25th AIAA/CEAS Aeroacoustics Conference*, 2019, p. AIAA-2019-2602.

[11] H. Boden, S. Sack, and S. Jacob, "Impedance measurements for 3-D printed liners," in *25th AIAA/CEAS Aeroacoustics Conference*, 2019, p. AIAA-2019-2600.

[12] A. Schulz, F. Bake, L. Enghardt, and D. Ronneberger, "Impedance eduction of acoustic liners based on four different levels of physical modeling," *22nd AIAA/CEAS Aeroacoustics Conf. 2016*, pp. 1–19, 2016.

[13] L. A. Bonomo, A. Spillere, and J. A. Cordioli, “A parametric uncertainty analysis for impedance eduction based on Prony’s method,” in *25th AIAA/CEAS Aeroacoustics Conference*, 2019, p. AIAA-2019-2541.
[14] M. E. D’Elia, T. Humbert, and Y. Auregan, “Direct impedance eduction of liners from Laser Doppler Velocimetry measurements,” in *25th AIAA/CEAS Aeroacoust. Conf*, 2019, p. AIAA-2019-2516.
[15] M. G. Jones, W. R. Watson, D. M. Nark, and B. M. Howerton, “Impedance Eduction for Multisegment Liners,” in *24th AIAA/CEAS Aeroacoustics Conference*, 2018, p. AIAA-2018-3441.
[16] M. G. Jones, D. M. Nark, and W. R. Watson, “Evaluation of a Multizone Impedance Eduction Method,” in *25th AIAA/CEAS Aeroacoustics Conference*, 2019, p. AIAA-2019-2486.
[17] A. M. Spillere, L. A. Bonomo, J. A. Cordioli, and E. J. Brambley, “Testing Impedance Eduction Boundary Conditions with Four Wavenumbers per Frequency,” in *25th AIAA/CEAS Aeroacoustics Conference*, 2019, p. AIAA-2019-2488.
[18] Z. Zhang, M. Åbom, H. Boden, X. Jing, and L. Du, “Recent Development in the Cremer Impedance: Experimental Analysis, Numerical Validation and Triple Roots,” in *25th AIAA/CEAS Aeroacoustics Conference*, 2019, p. AIAA-2019-2467.
[19] C. Heuwinkel *et al.*, “Characterization of a Perforated Liner by Acoustic and Optical Measurements,” in *16th AIAA/CEAS Aeroacoust. Conf*, 2010, p. AIAA-2010-3765.
[20] J. Gürtler *et al.*, “High-speed camera-based measurement system for aeroacoustic investigations,” *J. Sens. Sens. Syst.*, vol. 5, pp. 125–136, 2016.
[21] C. K. W. Tam, N. N. Pastouchenko, M. G. Jones, and W. R. Watson, “Experimental validation of numerical simulations for an acoustic liner in grazing flow: Self-noise and added drag,” *J. Sound Vib.*, vol. 333, pp. 2831–2854, 2014.
[22] S. Enomoto, T. Ishii, T. Nishizawa, and H. Toh, “Numerical Analysis of Acoustic Liner Performance in grazing flow,” in *25th AIAA/CEAS Aeroacoust. Conf*, 2019, p. AIAA-2019-2613.
[23] E. Brandão, P. Mareze, A. Lenzi, and A. R. da Silva, “Impedance measurement of non-locally reactive samples and the influence of the assumption of local reaction,” *J. Acoust. Soc. Am.*, vol. 133, no. 5, pp. 2722–2731, 2013.
[24] R. Dragonetti and R. A. Romano, “Considerations on the sound absorption of non locally reacting porous layers,” *Appl. Acoust.*, vol. 87, pp. 46–56, 2015.
[25] R. Dragonetti and R. A. Romano, “Errors when assuming locally reacting boundary condition in the estimation of the surface acoustic impedance,” *Appl. Acoust.*, vol. 115, pp. 121–130, 2017.
[26] C. K. W. Tam and K. A. Kurbatskii, “Microfluid Dynamics and Acoustics of Resonant Liners,” *AIAA J.*, vol. 38, no. 8, 2000.
[27] T. Ishii, K. Nagai, O. H, K. J, E. S, and T. Oishi, “Acoustic Research Programs in Aircraft Engines in JAXA: aFJR and Green Engine,” *Asian Jt. Conf. Propuls. Power 2016*, pp. AJCPP2016-131, 2016.
[28] T. Harada, K. Nagai, H. Oinuma, H. Daiguji, and T. Ishii, “Validation of Impedance Eduction Method for Acoustic Liner Panel in Grazing Flow,” *Asian Jt. Conf. Propuls. Power*, 2018.
[29] D. C. Pridmore-Brown, “Sound propagation in a fluid flowing through an attenuating duct,” *J. Fluid Mech.*, vol. 4, no. 4, pp. 393–406, 1958.
[30] U. Ingard, “Influence of Fluid Motion Past a Plane Boundary on Sound Reflection, Absorption, and Transmission,” *J. Acoust. Soc. Am.*, vol. 31, no. 7, pp. 1035–1036, 1959.
[31] M. K. Myers, “On the acoustic boundary condition in the presence of flow,” *J. Sound Vib.*, vol. 71, no. 3, pp. 429–434, 1980.
[32] 吉田季晶, J. A. Tuasikal, 大宮司啓文, and 石井達哉, “グレージング流れ中における吸音パネルの音響インピーダンス推定,” in *JSASS*, 2019.

APPENDIX 5.1

Face to Face Microphones inside the Sample Section

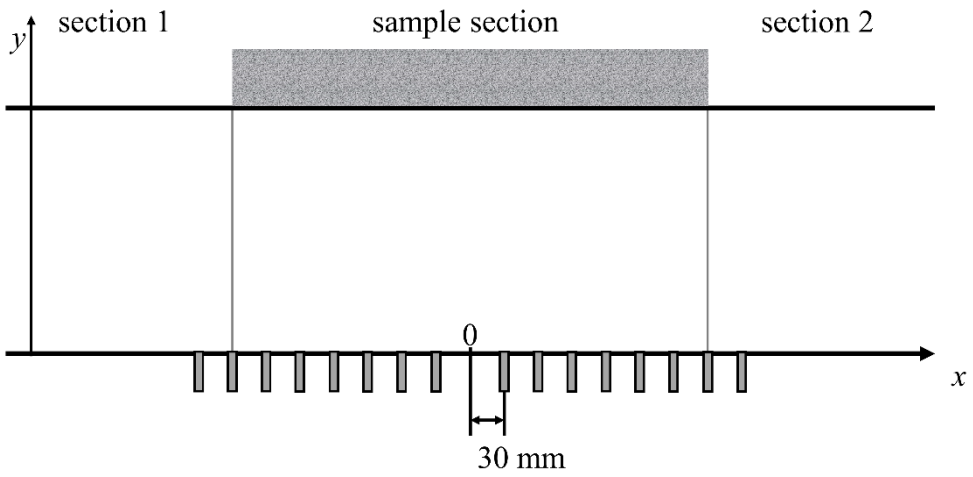

Figure A5.1. The Face to Face Microphone.

Figure A5.1 shows the face to face microphone installed inside the sample section. The pressure detected by these microphones could show directly the reduction of pressure amplitude of the sound wave while propagating inside the sample section. However, using this microphone placement, direct impedance eduction using Kumaresan and Tufts (KT) Method cannot be conducted because there is no microphone installed at $x = 0$. However, the pressure data could be processed to directly obtain the actual wave number inside the sample section by curve fitting method. The actual wave number might be not so different only in some frequency values as reported previously by Yoshida [32].

APPENDIX 5.2

Shear flow profile for the impedance eduction process

The shear flow profile used for solving the Pridmore-Brown is shown in Fig. A5.2. The flow profile was obtained by averaging measurement results of hardwall (no liner) and five resonator type liners with different dimensions and structures. The measured flow profile of the six cases was similar and agreed with 1/7 power law flow profile. Further analysis on the flow profile was reported in Ref.[10].

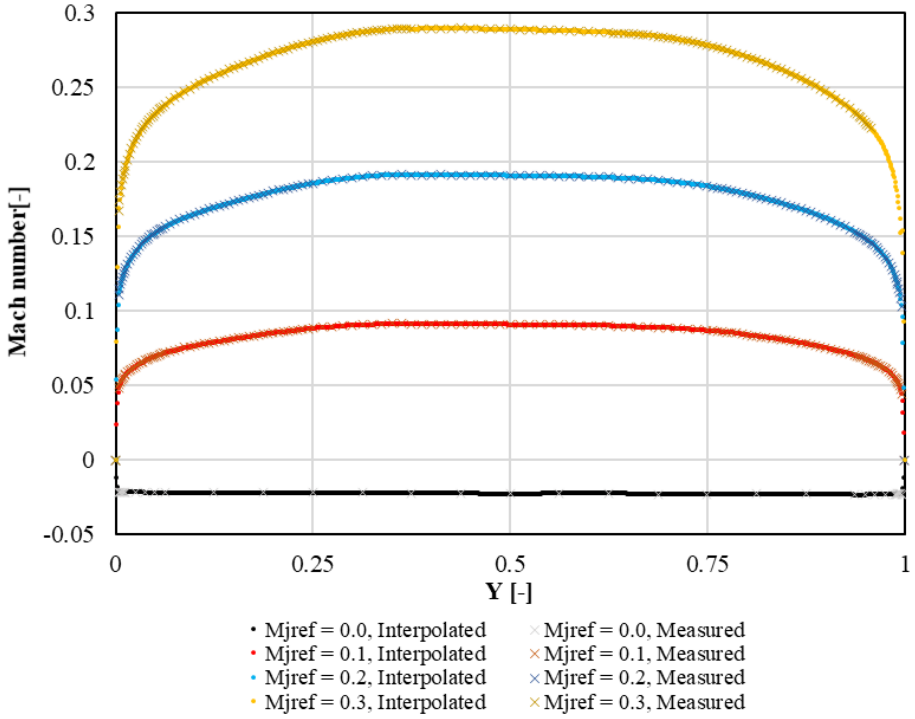

Fig. A5.2. Flow profile in the y axis of the flow duct

CHAPTER 6

Conclusion

In this study, the viscous loss and resonance mechanisms of sound attenuation inside porous materials were observed from the IT experiments. Attenuation due to viscous loss occurred inside the sintered fiber samples that consisted of reticulated structures. Conversely, the attenuation due to resonance was prominent inside foam materials that consisted of pores separated by walls that resembled aggregated cells. However, the foam material that consisted of a reticulated structure could not accommodate the resonance inside the pores as the pores were highly connected. Such cellular foam materials attenuated sound in a similar manner to sintered fiber.

Regarding modeling, the DB model, which considered only the flow resistivity in the calculation, predicted accurately the acoustic properties of sintered fiber and cellular foam materials with a high porosity. This model was accurate for homogenous sintered fiber samples with fiber orientation perpendicular and parallel to the sound wave direction, but it failed for inhomogeneous samples. The DB model also provided an estimation of the maximum SAC range for the foam with cellular structure but failed to predict the SAC peaks and trough. Furthermore, even though the Sides model used additional calculations to predict the flow resistivity, it yielded similar results to those of the DB model for sintered fiber materials. The acoustic properties of foam with a cellular structure can be predicted accurately using the resonance analysis based acoustic model for cellular materials, i.e Lu model.

The relation between flow resistivity and the averaged SAC values of porous materials was also investigated. The SAC increased as the flow resistivity increased until it attained a maximum value, and then started to decrease as the flow resistivity further increased. Thus, there is an optimum range of flow resistivity to obtain the best SAC. However, this optimum range might be different depends on the porous structure. Furthermore, flow resistivity might be able to predict the acoustic energy loss due to viscous loss inside sintered fiber samples by using DB model. However, the value of the flow resistivity was not enough to predict the SAC distribution of foam material in a wide frequency range. A broad frequency-dependent SAC distribution was required in the design process which aimed to reduce noise at specific frequencies. In addition, this research showed that the porous materials might provide a different sound attenuation performance depend on their structure, even though the porosity is similar.

It is difficult to define whether the porous samples are locally reactive or non-locally reactive liner. However, by comparing the IT and FD results, it was found that the surface impedance of the sintered fiber and the foam samples with ϕ = 81% inside the IT and FD has an identical trend which is similar to the case of locally reactive resonator liner. In contrast, the surface impedance characteristic in the IT and FD is different for the foam samples with ϕ = 85%. The porous material might act similar to the locally reactive liner if the flow resistivity is high, but as non-locally reactive if the flow resistivity is low. For the locally reactive samples, the impedance inside the FD might be predicted more easily from the IT impedance results.

The effect of the interaction between the air flow and sound wave was shown to affect the SAC and Re (kx/k) of the samples. The increase of the air speed affects the effective sound speed. Thus, the SAC curve was shifted to a higher frequency in forward mode to a lower frequency in reverse mode. Furthermore, the increase of the air speed shifted the Re (kx/k)

lower in the forward mode and higher in the reverse mode. However, in the case of the foam samples, at high frequency, there might be another factor that might affect the attenuation mechanism so that the effect of air speed on the SAC curve changed. Furthermore, the effect of the air speed on the Im (*kx/k*) that represent the reduction of the pressure amplitude of the sound wave inside the sample section cannot be interpreted as easily.

The velocity profile affected the impedance of some samples, the sintered fiber sample with ϕ = 65% and the foam sample with ϕ = 85%, but not the other two samples. The velocity profile is related to the boundary layer. Thus this parameter might represent the interaction between the air flow and the porous structure. If the uniform velocity profile was used, the impedance eduction disregards the boundary layer. In contrast, by using a non-uniform velocity profile, the effect of flow boundary layer can be considered. For the current research, the pressure distribution in *y* axis can be understood by using the mass-damper-spring system analogy. However, the interaction between the air flow, sound wave, and porous structure cannot be interpreted using the current results. The sound attenuation mechanism inside the boundary layer and also inside the sample structure is still to be solved.

LIST OF PUBLICATIONS

Journal Paper

1. Jannati Adnin Tuasikal, Yo Murata, Kisho Yoshida, Takuya Harada, Kanta Sato, Hirofumi Daiguji, and Tatsuya Ishii
   "Sound Absorption Properties of Stainless Steel Sintered Fiber and Cellular Foam in Impedance Tube and Flow Duct Experiments"

International Conference

1. Jannati Adnin Tuasikal, Kanta Sato, Hirofumi Daiguji, and ○Tatsuya Ishii
   "Sound Absorption Characteristic of Stainless Steel Foam with Porosity Variation"
   Asian Joint Conference on Propulsion and Power, Xiamen-China, March, 2018
   AJCPP2018-25
   Type: Oral presentation and printed document. (peer-reviewed paper)

2. Jannati Adnin Tuasikal, Kanta Sato, Hirofumi Daiguji, and Tatsuya Ishii
   Sound Absorption of Sintered Stainless Steel Fibers Blocks
   2018 AIAA AVIATION Forum, Atlanta-USA, June, 2018
   AIAA-2018-3928
   Type: Oral presentation and printed document. (peer-reviewed paper)

3. Jannati Adnin Tuasikal, Hirofumi Daiguji, and Tatsuya Ishii
   Sound Absorption Characteristics of Porous Metal with Structure Configuration Variation
   25th AIAA/CEAS Aeroacoustics Conference, Delft-The Netherland, May, 2019
   AIAA-2019-2748
   Type: Oral presentation and printed document. (peer-reviewed paper)

4. Jannati Adnin Tuasikal, Yo Murata, Kisho Yoshida, Hirofumi Daiguji, and Tatsuya Ishii
   Attenuation of Sound Wave by Porous Metal inside a Flow Duct
   26th AIAA/CEAS Aeroacoustics Virtual Conference, June, 2020
   AIAA-2020-2609
   Type: Oral presentation and printed document. (peer-reviewed paper)

Domestic Conference

1. 吉田季晶，Jannati Adnin Tuasikal，大宮司啓文， 石井達哉
   グレージング流れ中における 吸音パネルの音響インピーダンス推定
   第 59 回航空原動機・宇宙推進講演会 2019 年 3 月 6 日～7 日 長良川国際会議場
   講演番号: 2C19 (JSASS-2019-0095)

Kisho Yoshida, Jannati Adnin Tuasikal, Hirofumi Daiguji, Tatsuya Ishii
Impedance Eduction of Acoustic Panels in Grazing Flow
The 59 the conference on aerospace propulsion and power, Gifu, March 7, 2019
Paper number: 2C19 (JSASS-2019-0095)